UPC
Departament d'Enginyeria
Mecànica
UNIVERSITAT POLITÈCNICA DE CATALUNYA

A dynamical model of a double-deck circular tunnel embedded in a full-space

by

Arnau Clot Razquin

directed by

Jordi Romeu Garbí
Robert Arcos Villamarín

A thesis submitted in partial fulfillment for the
degree of Doctor of Philosophy of Mechanical Engineering

in the
Escola Tècnica Superior d'Enginyeries Industrial i Aeronàutica de Terrassa
Department of Mechanical Engineering

January 10, 2014

Abstract

Escola Tècnica Superior d'Enginyeries Industrial i Aeronàutica de Terrassa
Department of Mechanical Engineering

Doctor of Philosophy in Mechanical Engineering

by Arnau Clot Razquin

This thesis presents a three-dimensional dynamic model of a double-deck circular tunnel embedded in a full-space. The model uses the receptance method to obtain the response of the complete structure from the response of its parts. The considered subsystems are the interior floor and the tunnel-soil coupled system. The classical thin plate theory is considered to represent the behaviour of the first and the Pipe in Pipe model is chosen to describe the second. Because the complete model is assumed to be geometrically invariant in the train circulation direction, the coupling of both systems is performed in the wavenumber-frequency domain. After the model formulation, some important issues about its numerical computation are detailed and the obtained results are discussed. The response of a double-deck tunnel to a dynamic and to a quasistatic excitation is compared to the response obtained for a simple tunnel. The first comparison is done performing a power flow study of both tunnel structures when a harmonic line load is applied on them. The main differences between their radiation magnitudes and patterns are identified and discussed. The second comparison is done calculating the total amount of energy crossing a certain surface when a static load moving at a constant speed is considered. Results for a wide range of load speeds and radial distances are presented. A complete track-tunnel-soil model is finally obtained coupling a superstructure model to the interior floor model previously presented.

Acknowledgements

En primer lloc vull expressar la meva enorme gratitud als directors d'aquesta tesis, en Jordi Romeu i en Robert Arcos, tant per la seva confiança, consells i recolzament com per la seva inesgotable paciència en cada una de les moltes converses que han anat donant forma a aquest treball. Ha estat un immens plaer treballar amb persones amb tanta energia, optimisme i motivació.

No menys important ha estat el suport rebut per part de tots els membres d'aquesta bonica família que és el LEAM. Gràcies a la Tere, a l'Andreu, a en Santi i a tots els becaris i excompanys per totes les aventures que hem compartit dins i fora del TR45. I mereixen una menció apart la Sara i en Robert, a qui vull donar les gràcies pels centenars de rialles, sonores i sinceres, emeses pel despatx 1.02 al llarg d'aquests anys.

Tota aquesta aventura no l'hauria pogut ni acabar ni molt menys gaudir tant com ho he fet de no ser per tots aquells grans amics que m'han donat, sabent-ho o no, forces per seguir enfrontant-me als reptes i obstacles del viatge. Vull donar les gràcies a la Maria, per haver-me recolzat del primer a l'últim pas, a en Marc i en Pep, a qui sempre sento al meu costat per més que es separin els nostres camins, a L'Alba i a l'Ari, per tots els avituallaments on hem agafat noves forces per seguir endavant, i a tots els meus amics de Lleida, els propers i els llunyans, que fan encara mes especial cada tornada a casa. Gràcies a tots per haver formar part d'aquesta etapa de la meva vida.

I finalment, vull donar les gràcies a tota la meva família, avies, tiets, cosins i cosines, per haver-me fet sentir enormement estimat i valorat, tant en els bons i com en els (pocs) mals dies que un viatge així necessariament té. I molt especialment als meus germans, Ferran i Guillem, i als meus pares, Anna i Salvador. Crec que no us dic això ni una petita part de les vegades que ho hauria de fer: Gràcies per ser com sou i per tot el que m'heu donat.

Contents

List of Figures

List of Tables

Als meus germans i als meus pares

Chapter 1

Introduction

This text begins with a brief introduction to the railway ground-borne vibration problem and justifies the main reasons that led to the development of the present work. After this, a brief outline of the contents of each chapter is presented.

1.1 Justification of this work

Underground railway systems have become one of the most important forms of public transportation in heavily populated cities. One of the major problems of these type of transport is the propagation of the generated vibration through the soil into the nearby buildings. If effective isolation methods are not applied, the comfort of the inhabitants of these buildings is reduced due to the ground-borne vibration and the re-radiated noise caused by the vibration of the building structural members.

The choice of an adequate isolating system is of critical importance in the design of an underground railway system. On one hand, if the chosen isolating system is not sufficiently efficient mitigating the generated vibrations, structural modifications with a large economical cost may be required. On the other hand, if an effective isolation system is used in cases where the generated vibration isn't high enough to be a source of annoyance, the cost of the constructed infrastructure is unnecessarily increased. It becomes clear that precise predicting models are a fundamental tool to use in the design of a new railway system or in the modification of an existing one.

Due to the huge complexity of the train-track-ground-building coupled system, different approaches have been proposed for obtaining useful models for the prediction of train-induced ground-borne vibrations. These models are usually classified into three types:

Empirical, numerical and analytical models. A brief description of each one is presented in the following paragraphs.

Empirical models use experimental results to obtain simple decaying laws between the vibration levels at certain positions of the ground and the distance of these to the considered source. These type of models were firstly proposed by Bornitz [2] and popularized by Barkan [3]. A review on the propagation of ground vibrations, particulary focused on them, has been written by Gutowsy and Dym [4]. Despite being fast and easy to apply, these models are unable to give an insight view of the physical phenomena involved in the problem and also present a high degree of inaccuracy.

Numerical models, such as Finite Element (FE) [5, 6], Boundary Element (BE) and FE-BE hybrid models [7, 8], can obtain high precision predictions of the vibration behaviour of complex structures. However, even in the cases where a geometrical invariance [9–11] or periodicity [12] of the system is considered, the use of this type of models has huge computational and engineering costs which, combined with their limitations extrapolating any obtained results, restricts the economical viability of their use to very particular cases.

Analytical models describe the dynamical behaviour of the system using theoretical considerations. Their use allows to understand the mechanics of the considered problem and the effect that the involved parameters have on this. These type of models show many advantages in front of the other ones considered: they are clearly more flexible and powerful than empirical models and have a much lower computational and engineering cost than numerical models. The main drawback of these models is that many complex structures can't be modelled analytically, requiring the use of numerical models to predict its response. Examples of analytical models used in the prediction of train induced vibrations are [13–18].

Almost all the underground railway lines have trains circulating in both directions. This requirement has usually been solved constructing two identical tunnels, one for each direction, but different single tunnel designs have also been implemented. An innovative and interesting solution is the use of double-deck tunnels, where the tunnel is divided into two sections by an interior floor and trains circulate along both sections. An example of this type of design has been recently used in some stretches of Line 9, a new Barcelona's underground railway. Fig. 1.1 shows the cross-section of this structure.

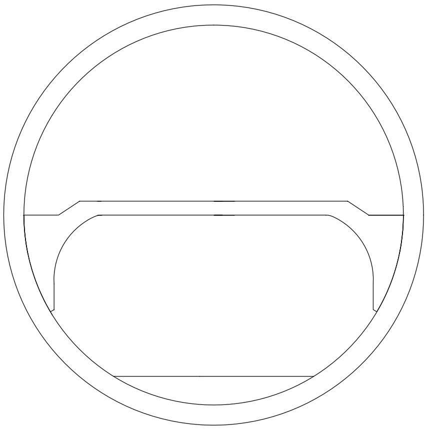

Fig. 1.1: Cross-section of the Barcelona's underground railway Line 9 double-deck circular tunnel.

It seems clear that the dynamical behaviour of a double-deck tunnel will show novel and unexpected phenomena that must be properly studied. The use of empirical or numerical models is not the most adequate way to achieve this goal. While the former are completely unable to model the problem, the computational costs and numerical nature of the later makes them adequate for the obtention of precise results for a given set of parameter values but non-viable for the study of the effect that each element of the system has in the global response. It is then almost necessary to use an analytical model for a proper understanding of the dynamic-response of a double-deck tunnel structure. The lack of existence of an analytical model for this type of tunnel is what has motivated the development of the present work.

In this thesis, an analytical model for describing the dynamical behaviour of a double-deck circular tunnel embedded in a full-space is developed. The proposed model treats the interior floor of the tunnel as an infinite thin plate and uses the well-established PiP model [17] to represent the tunnel-soil system. The global model is obtained using the receptance method [19]. Once the model is formulated, different dynamical responses of a double-deck tunnel are obtained and compared to the ones obtained in a simple tunnel.

1.2 Thesis outline

The text is divided in seven chapters. In this chapter, a brief justification of the presented work and an outline of the contents of each chapter of this text are described.

Chapter 2 presents a short review of the most relevant work published about the vibration of coupled plate-shell systems, fundamental solutions and methods presented to treat elastodynamic problems and train-induced ground-borne vibration models.

Chapter 3 develops a three-dimensional model of a double-deck circular tunnel embedded in a full-space. This chapter begins with the formulation of the dynamical models considered for the interior floor and the tunnel-soil coupled systems. After this, the assumed coupling conditions are defined and some numerical considerations that should be taken into account are also described.

Chapter 4 develops a power flow calculation of the response of a double-deck tunnel to a harmonic line load. Because the problem is a plane-strain one, this chapter begins presenting the two-dimensional formulation of the model. After that, the considered power flow calculation is performed and the results are compared to those obtained in a simple tunnel model.

Chapter 5 presents a calculation of the radiated energy by a double-deck tunnel when a static load moving at a constant speed is applied on its interior floor. Again, the results are compared to those obtained in a simple tunnel case.

Chapter 6 adds a track model to the interior floor model to obtain a complete track-tunnel-soil model for a double-deck tunnel.

Finally, Chapter 7 points out the main conclusions obtained in the previous chapters and proposes some guidelines and recommendations for further work developed on the topic.

Chapter 2

Literature review

This chapter presents a review of the previously published works that are relevant to the present study. The chapter is divided into three sections. The first section is devoted to the dynamical behaviour of plate-shell combined structures. The second deals with the modelisation of the soil as a linear elastic media focusing on the existing fundamental solutions, especially those which consider a buried load. Finally, the last section presents the main underground train-induced ground-borne vibration models existing in the literature.

2.1 Vibration of thin shell structures

Thin shell structures play a key role in the proposed model for a double-deck circular tunnel. Because this type of tunnel is modelled assuming a combined plate-cylindrical shell structure, a review of works dealing with these structural elements is presented.

2.1.1 Vibration of plates

Depending on the thickness of the plate, theories with different degrees of complexity have been proposed to model its dynamical response. When this thickness is much smaller than the width and length of the plate, it is well established that the classical plate theory formulated by Kirchoff is good enough to represent the dynamics of the plate. A vast amount of literature deals with the analytical results obtained considering these type of structure under many different boundary and initial conditions. Important studies of the free response of a thin plate have been developed by Warburton [20] and

Leissa [21]. Most of the published results in the field of the transverse vibrations of a thin plate have been collected and unified by Leissa in a must have book [22].

Less efforts have been dedicated to the study of the in-plane vibrations which, at high excitation frequencies, can be of great importance. An exact solution for two simply supported boundaries and any combination of classical boundaries for the other two has been recently obtained by Liu and Xing [23].

2.1.2 Vibration of shells

A great number of theories have been proposed to model the static and dynamic behaviour of thin walled structures with curvature. Unlike in the thin plate case, there is not a common agreement on which one of them is the best for representing the behaviour of this fundamental structures. Most of the proposed theories are based on the Love's shell theory [24] and have been obtained after performing slight modifications on its hypothesis. Some of the most used are the ones presented by Donell [25], Timoshenko [26], Reissner [27], Flügge [28] and Sanders [29]. Again, a huge effort has been done by Leissa collecting and unifying many of the published results in a single reference [30].

2.1.3 Vibration of plate-shell combined structures

Coupled plate-cylindrical shell structures have been studied by several researchers because of its interest as airplane fuselage models. Peterson and Boyd [31] presented the first analytical model for a shell with a partitioned floor. Langley [32] studied, using a dynamic stiffness method, the free vibration of circular cylinders stiffened with an interior floor. With a variational formulation, Missaoui et al. [33] studied the free and forced vibration of a plate-shell system using artificial springs to simulate the structural coupling. Using the receptance method [19], Lee et al. [34] obtained the free vibrations of a simply supported shell-plate structure. The model was later extended by Lee et al. [35] to include the laminated composites case. For both cases, the free vibration of the subsystems was calculated using the Rayleigh-Ritz energy method and the eigenfrequencies of the global system thereby obtained were compared with experimental results. The receptance method was also used by Wang et al. [36] to study the power flow characteristics of the plate cylindrical shell structure and by Zhao et al. [37] to study the forced response of a plate-cylindrical shell structure.

2.2 Soil models

In vibration problems, due to the small magnitude of the stresses involved, the soil is usually modelled as a linear elastic media. When isotropy is assumed, two independent elastic constants are required to characterise it, usually the first and second Lamé constants. When linear elasticity is assumed in an infinite media, two types of volumetric waves are found: the compressional or P-waves and the shear or S-waves. A third type of wave, the Rayleigh wave, is also found when the media is considered to be semi-infinite [38]. If a layered half-space is considered, the existence of other types of waves is also found. This is the case of the Love waves [39], that appear when a soft layer lies over a rigid one, and of the Stoneley waves [40], that exist in a solid-solid interface.

2.2.1 Fundamental elastodynamic solutions

Closed-form solutions have only been obtained for a reduced number of elastodynamic problems. One of the first and most important results was the one presented by Stokes [41], who deduced the displacement field of a full-space under the action of time varying point forces. A not least important work was later developed by Lamb [42], who obtained the displacement field of an elastic half-space under the action of a line or a point load. Lamb was unable to fully evaluate the integrals of his solutions and obtained the asymptotic (far field) solution of the problem. Because of the size of his contribution, this problem is nowadays known as the Lamb's problem. The integrals of the exact solution were later solved, performing a hardly understandable contour integration, by Cagniard [43]. The procedure was simplified by De Hoop [44], and received the name of the Cagniard-De Hoop method. The impulse surface line load was also studied by Sherwood [45], who compared his solution with some experimental results obtained detonating small explosive charges. Pekeris found the analytical expressions of the displacements caused by a surface [46] and by a buried [47] point load when its time dependance was given by a Heaviside function and considering both Lamé constants equal. Interesting results have also been presented by Arcos et al. [48] who, comparing the exact and the asymptotic surface line and point load solutions of the Lamb's problem, determined the size of the near field and studied the effect of the ground's mechanical parameters on it.

Studies on the energy distribution among the different types of waves generated by a surface source have been developed by Miller and Pursey [49, 50]. Their results have been recently generalised by Razin [51], who presented the distribution of energies for a buried harmonic point source, finding a particular depth of the source where the energy in form of Rayleigh waves reaches a maximum.

Interesting advances have also been performed in the numerical evaluation of Lamb's solutions. Georgiadis et al. [52] presented a procedure to evaluate the point load case. Arcos et al. [53] greatly reduced the computational cost of this numerical evaluation by combining the use of a clever change of variable and the substraction of the static integrand, a technique previously proposed by Apsel and Luco [54].

Most of these fundamental elastodynamic solutions have been recently collected and unified in a book by Kausel [55].

2.2.2 Layered half-space

A matrix formalism to study the dynamic response of a layered media was firstly derived by Thompson [56] and revised and computed by Haskell [57]. After them, many other authors worked on increasing the computational efficiency of the method by rewriting the analytical expressions. Among all the published advances, a special mention must be done to the work presented by Kausel and Roësset [58] who obtained the stiffness matrix of each layer, allowing to treat the problem in the same way that conventional structural analysis problems.

2.2.3 Viscoelasticity

One of the most used damping models in soil dynamics is the nonviscous Kelvin-Voigt model. In this type of model, the internal friction of the media is modelled considering complex valued mechanical parameters. Using the correspondence principle announced by Read [59], any viscoelastic solution is directly obtained from the corresponding elastic one extending the validity of this last to complex values of the field variables.

2.3 Train induced ground-borne vibration

This section starts with a justification of the considered frequency range of study based on the published results. After that, some of the most important numerical and analytical underground train-induced ground-borne vibration models are reviewed. The section end with a description of the inherent limitations and unavoidable uncertainty of any proposed, numerical or analytical, model.

2.3.1 Frequency range of the problem

This subsection discusses the range of frequencies of interest in train-induced ground-borne vibrations. This range must be correctly defined in order to assume valid hypothesis and develop realistic simplifying models of this type of problem. The section considers separately the range of frequencies excited in the wheel-rail interaction and the ranges of interest when the response of the track or the soil are predicted.

Excitation mechanisms

Two main types of excitation are usually distinguished in train-induced ground vibrations: the quasi-static and the dynamic excitations.

The quasi-static excitation is related to the static component of the considered moving load. This type of excitation mechanism is of great importance for High Speed Trains (HST) tracks placed on soft soils. In these cases, the train speed can be similar to the critical phase speed of the track-soil system and the quasi-static excitation generates high vibration levels [60]. The frequency content of the generated excitations is concentrated between 0 and 50 Hz [61].

The dynamic excitation is caused by the dynamic interaction of the train-track system. The main causes of this type of excitation are the wheel and track unevenness and the variations of the mechanical parameters of the track [62]. The dynamic excitation is usually the main source of excitation in low and mid-speed trains. Remennikov and Kaewunruen [63] state that the dynamic/impact loading frequency range is 0-2000 Hz.

Track response

Knothe and Grassie [64] modelled the vehicle/track interaction problem giving frequency ranges of study for each part. When the track, the sleepers and the wheel-rail irregularities are studied, they proposed a frequency range between 0 and 1500 Hz. Regarding the rail model, the same authors also concluded that a Bernoilli-Euler beam model could be used for excitation frequencies under 500 Hz. Above this value, higher order theories must be considered. A Timoshenko beam is used, for example, by Thompson on the wheel-rail noise generation [65–67].

The importance of considering a detailed ground model in superstructure modelling was studied by Knothe and Wu [68], who determined that this was mandatory for frequencies under 250 Hz. The same conclusion was obtained by Van den Broeck and De Roeck [69], who studied the changes of the direct receptance (the response of the rail on the position where the load is applied) when different ballast and substrate models are considered.

Soil response

When the ground response is required, the high frequency content is rapidly attenuated due to the material damping. Results obtained by Heckl et al. [70] showed that the dominant frequency range of ground vibrations was between 40-100 Hz and that these vibrations become very small above 200 Hz. Similar results have been found for example by Degrande and Schillemans [71] in experimental measures of HST. Significant underground railway vibration levels where found in the range 10-100 Hz in experimental measures done by Gupta et al. [72].

Building response

For the case of building vibrations caused by train passages, measures performed by Kuppelwieser and Ziegler [73] showed that the range where building vibrations where most apreciable was between 10 and 60 Hz. A similar frequency range is considered by the technical standards [74–76], which state that the frequency range has to be measured between 1 and 80 Hz. For the case of the re-radiated noise by the structural members of the building, Hood et al. [77] measures showed that the frequency range of the problem was between 50 and 160 Hz.

2.3.2 Numerical models

Several numerical models have been proposed to treat the problem of underground train-induced vibrations. Due to the computational cost of the problem, two-dimensional (2D) models have been used by some authors as a simplifying assumption. This is the case for example of Chua et al. [5], who used a 2D FE model with absorbing boundaries to study the building response to subway train traffic, or Jones et al. [7], who developed a 2D Finite Element-Boundary Element (FE/BE) hybrid model and used it to study modifications in the design of two types of tunnels. The possibility of considering 2D models instead of three-dimensional (3D) ones was studied by Andersen and Jones [8]. They compared the results of a 2D and a 3D FE/BE hybrid model of two types underground tunnels. Their conclusion was that a 2D model was useful to study vibration reductions achieved when changes on the structure are done but a full 3D model was required for absolute vibration transmission predictions.

To overcome the numerical difficulties of a 3D model, two simplifying considerations have been lately performed: to assume that the tunnel-soil system is an infinite periodic structure and to assume that it is an infinite structure of invariant cross-section.

The periodicity of the tunnel-soil system in the train circulation direction can be used to simplify the computational cost of the numerical models and still obtain accurate results. Considering this assumption, a Floquet transform [78] can be applied to the problem and the complete solution is then obtained discretising only a reference cell. This method was used by Cloteau et al. [79] to study the dynamical behaviour of very long structures. In the framework of the CONVURT project, Cloteau et al. [12] presented a periodic coupled FE/BE model to obtain the vibration response of underground infrastructures. The results of this model have been compared with the ones obtained using the Pipe-in-pipe model (PiP) by Gupta et al. [80]. The model was also used by Gupta et al. [72] to predict the vibrations of an underground train passage in Beijin. Recently, Gupta and Degrande [81] proposed to use this methodology to compare the efficiency between continuous and discontinuous floating slabs.

The invariance of the system in the train circulation direction allows to solve the problem using a two-and-a-half dimensional (2.5D) model. In this type of model, the problem is transformed to the wavenumber domain and the complete solution is found solving a cross-section of the system for a discrete set of wavenumber values. One of the first articles using a 2.5D FE/BE model, was presented by Aubry et al [82]. Sheng et al. [9] outlined the use of this type of model and demonstrated its applicability to surface and tunnel vibrations. This modelling method was used by the same authors to study the response of infinite periodic structures to harmonic loads [83]. The method has also been used by Yang and Hung [84], who presented a 2.5D finite/infinite element procedure to study the ground vibrations induced by surface and buried moving loads. They also used this method to develop a parametric study for the case of vibrations caused by underground trains [85]. A recent example of the use of this modelling technique for a surface and underground tracks is done by François et al. [10] and Galvin et al [11].

Several alternative numerical formulations can also be found in the literature. To avoid the inviability of developing a 3D FE model of the problem, Gardien and Stuit [6] divided it into three submodels. Another interesting approach to obtain fast results and still take advantage of the adaptability of numerical methods was proposed by Müller et al. [86], who developed an hybrid FE-analytical model of a non-circular tunnel formulated in the wavenumber domain.

2.3.3 Analytical models

Analytical models of underground train-induced vibrations have also been presented by several authors. These type of models are sometimes divided between fully analytical and semi-analytical models. In the first case, a closed form solution of the soil vibration is obtained while in the second, the obtention of results requieres to perform a numerical calculation (usually an integral antitransform). In both cases, the computational cost is negligible in front of the computational cost of a realistic numerical model of the problem. A model to study the low-frequency ground vibrations generated by HST circulating in tunnels has been proposed by Krylov [15]. Another fully analytical model, which considered the tunnel as a beam embedded in a half-space has been presented by Metrikine and Vrouwevelder [16].

A well-established model for the prediction of underground train vibrations is the PiP model, developed by Forrest and Hunt [17, 18]. This model initially considered the combined tunnel-soil system as a thin cylindrical shell coupled to a thick cylindrical shell of infinite external radius [17]. The tunnel-soil model was then coupled to a train-track model which considered the floating slab, the rail and the axle masses [18]. The model neglected the effect of the train suspensions and the Hertzian contact, as suggested by the experimental data given by Heckl et al. [70] and conclusions obtained by Clark [87]. A more detailed floating slab superstructure model was coupled to the PiP tunnel model by Hussein and Hunt [88]. In their work, three different coupling assumptions and the wave-guided solution of the global model where studied. Hussein and Hunt [89] used the model to study the mean power flow generated by an infinite train of point loads. This calculation was proposed as a good evaluator to quantify the efficiency of vibration countermeasures. Using the 2.5D elastodynamic Greens functions for a full-space obtained by Tadeu and Kausel [90] and those for a half-space (constructed using the formers ones) obtained by Tadeu et al. [91], the initial PiP model was extended by Hussein et al. [92] adding the existance of a free-surface. Comparing the full-space and the half-space versions of the PiP model, Jones et al. [93] suggested a 6 dB difference in the surface power spectral density (PSD) when the depth of the tunnel is at least of two tunnel-diameters. The consideration of a layered half-space was also developed by Hussein et al. [94]. In this case, the multi-layered half-space Green's functions are calculated using the direct stiffness method [58]. The model results where also compared to those obtained with the periodic FE-BE model previously explained [12, 95] finding good agreement between them despite the huge differences in calculation times (minutes in a personal computer against hours in one processor of a high performance cluster).

None of the previous analytical models is able to directly deal with a double-deck tunnel construction geometry. Some interesting results regarding the effect that the interior floor has on the track response have been obtained by Otero [1].

2.3.4 Inaccuraccy of the common assumptions

Because of the complexity of the coupled system train-track-tunnel-soil, numerous simplifying assumptions must be performed in any predictive model developed. The uncertainty and inaccuracy that some of these assumptions have is presented by Jones et al. [96] in a review about the topic. Some of these effects are briefly described in the next paragraph.

The existence of a twin tunnel, common in many underground systems and ignored by almost all the developed models, is studied by Kuo et al. [97]. The importance of modelling the discontinuities in floating slab tracks (FST) was considered by Hussein and Hunt, who developed a continuous [98] and a discontinuous [99] analytical models for this type of track. Using the 2D TLM, Jones and Hunt studied the importance of soil inhomogeneities [100] and of moderate layer inclinations [101]. Their use of a 2D model was justified by the previously mentioned results of Andersen and Jones [8]. The same authors relaxed the coupling condition between the tunnel and the soil in the PiP model and studied the effect of considering voids at the tunnel-soil interface [102].

Significant differences where obtained in all of the considered comparisons, in some cases obtaining differences on the predictions of 20 dB. This result shouldn't be ignored when predictive results are obtained from any analytical or numerical model.

Chapter 3

Double-deck circular tunnel model

In this chapter, a 3D model is developed for calculating the ground vibrations generated in a double-deck tunnel with a circular cross-section. The model considers the free response of the interior floor and of the tunnel-soil system separately and makes use of the receptance method to obtain the response of the coupled system. The interior floor is modelled as a thin plate and the tunnel-soil system is described using the Pipe in Pipe (PiP) model. Several issues that must be taken into account to perform an accurate numerical computation are also described. The response of the surrounding soil to a vertical harmonic point load applied on the interior floor is compared to the one caused by a radial point load applied at the bottom of a simple tunnel. The proposed model of a double-deck tunnel is compared to a weak coupled one. The effect on the interior's floor deflection of applying a radial point load at the bottom of the tunnel is also presented. The proposed model allows the PiP formulation to be extended to a new type of tunnel structure.

3.1 Notation used

Before exposing the considered model for a double-deck circular tunnel, the notation used through this chapter is presented. Despite defining it for the case of the displacements, the notation is also used for the stress fields and for the considered loads.

Harmonic motion is assumed for all the dynamic variables of the system. Then, for a certain displacement field $\mathbf{u}$, lower and upper case expressions are related as follows

$$\mathbf{u}(x,\dots,t) = \mathbf{U}(x,\dots)\mathrm{e}^{\mathrm{i}\omega t}, \tag{3.1}$$

where x is the coordinate in the train circulation direction, ω is circular frequency and t is time.

Because the coupling of the subsystems is performed in the wavenumber domain, the displacement field must be transformed using the Fourier transform defined by Eq. (A.3). The obtained expression is written as

$$\bar{\mathbf{U}}(k_x,\dots) = \int_{-\infty}^{\infty} \mathbf{U}(x,\dots)\mathrm{e}^{\mathrm{i}k_x x}\mathrm{d}x, \tag{3.2}$$

where the bar notation informs that the variable has been transformed, k_x is the x-direction corresponding wavenumber.

For the tunnel and soil cases, due to the periodicity of the system respect the angular coordinate, a Fourier series decomposition is also applied (see Section A.2). The notation used to define this coefficients is $\bar{\mathbf{U}}_n$.

3.2 Introduction

The double-deck tunnel (a tunnel with an interior floor dividing it) is modelled in this work as an infinitely long circular cylindrical shell of constant thickness h_t and constant mean radius r_t divided into two equal parts by an interior floor of constant thickness h_p, and no curvature. A cross-section of the model is presented in Fig. 3.1(a). The tunnel is considered to be embedded in a full-space and the resulting displacements are obtained at measuring distances $r_m \geq r_t$.

The next sections detail the mechanical models assumed for each subsystem and the coupling conditions considered, which can be seen in Fig. 3.1(b).

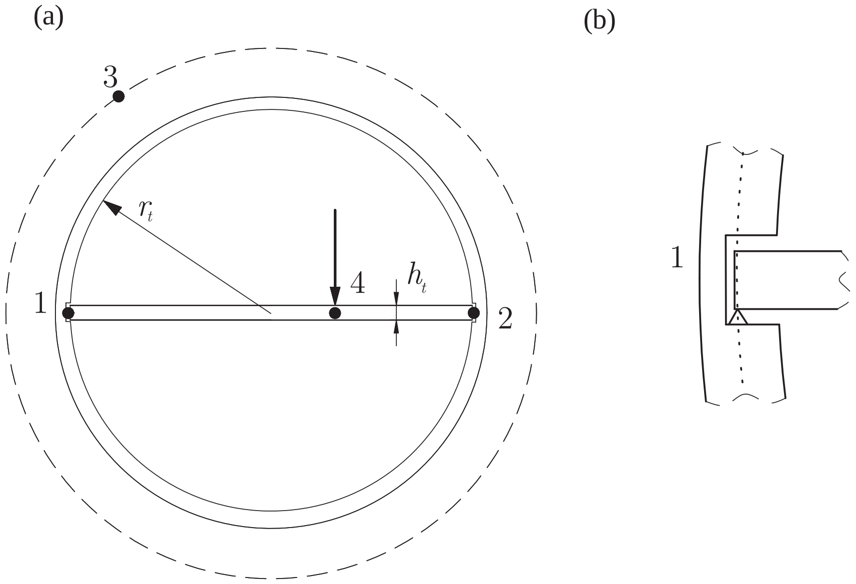

FIG. 3.1: (a) Cross-section of the double-deck circular tunnel model. (b) Coupling hypothesis between the interior floor and the tunnel.

3.3 Interior floor

3.3.1 Model hypothesis

The interior floor is modelled as an homogeneous and isotropic Kirchoff's thin plate of constant thickness h_p, constant width L_p and of infinite extent in the x-direction (a strip plate). A scheme of the model is shown in Fig. 3.2. A Cartesian system of coordinates (x, y_p, z_p) is chosen, where the subscript p, which indicates that the system of coordinates is related to the plate, is not used for the x-coordinate because it is shared by both considered subsystems. Because the receptance method requires it, the

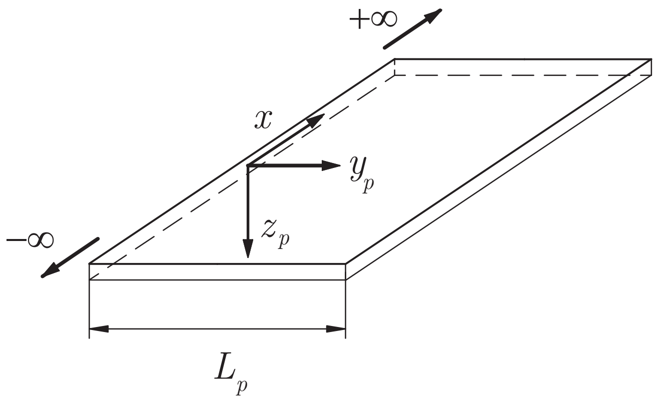

FIG. 3.2: Model and Cartesian system of coordinates considered for the interior floor.

two edges of the plate are considered to be free.

The transverse equation of motion of the interior floor is given by

$$D_p \nabla^4 w_p(x, y_p, t) = p(x, y_p, t) - \rho_p h_p \frac{\partial^2 w_p(x, y_p, t)}{\partial t^2}, \tag{3.3}$$

where

$$D_p = \frac{E_p h_p^3}{12(1-\nu_p^2)} \tag{3.4}$$

is the flexural rigidity of the interior floor, w_p is its deflection, ρ_p is its density, E_p is its Young's modulus, ν_p is its Poisson's ratio, $p(x, y_p, t)$ is the applied vertical load and

$$\nabla^4 = \frac{\partial^4}{\partial x^4} + 2\frac{\partial^4}{\partial x^2 \partial y_p^2} + \frac{\partial^4}{\partial y_p^4} \tag{3.5}$$

is the biharmonic operator.

The applied loads and the deflection are considered to be harmonic

$$w_p(x, y_p, t) = W_p(x, y_p)\mathrm{e}^{\mathrm{i}\omega t}, \qquad p(x, y_p, t) = P(x, y_p)\mathrm{e}^{\mathrm{i}\omega t}. \tag{3.6}$$

Because the considered system is of infinite extent in the x-direction, the problem is transformed to the wavenumber domain applying the Fourier transform defined by Eq. (A.3) to Eq. (3.3). The resulting equation is

$$\left(\frac{\mathrm{d}^4}{\mathrm{d}y_p^4} - 2k_x^2\frac{\mathrm{d}^2}{\mathrm{d}y_p^2} + (k_x^4 - \kappa^4)\right)\bar{W}_p(y_p) = \frac{\bar{P}(y_p)}{D_p}, \tag{3.7}$$

where

$$\kappa = \left(\frac{\rho_p h_p \omega^2}{D_p}\right)^{1/4}. \tag{3.8}$$

The forced response of a strip plate is obtained in this work using the modal participation method, which requires to know the free response of the system to obtain the forced one.

3.3.2 Free response

The free response of a strip plate is obtained solving Eq. (3.7) when $\bar{P} = 0$ and no damping is considered. Two types of solutions are usually considered in this problem: The case where $\kappa^2 > k_x^2$, identified as case I, and the case where $\kappa^2 < k_x^2$, identified as case II. The free response can be written as

$$\bar{W}_p(y_p) = \begin{cases} A^I \sin(\zeta_2 y_p) + B^I \cos(\zeta_2 y_p) & \\ \quad + C^I \sinh(\zeta_1 y_p) + D^I \cosh(\zeta_1 y_p), & \text{when } \kappa^2 > k_x^2, \\ A^{II} \sinh(\zeta_2' y_p) + B^{II} \cosh(\zeta_2' y_p) & \\ \quad + C^{II} \sinh(\zeta_1 y_p) + D^{II} \cosh(\zeta_1 y_p), & \text{when } \kappa^2 < k_x^2 \end{cases} \tag{3.9}$$

where

$$\zeta_1 = \sqrt{\kappa^2 + k_x^2}, \qquad \zeta_2 = \sqrt{\kappa^2 - k_x^2}, \qquad \zeta_2'^2 = -\zeta_2^2 \tag{3.10}$$

and where the four unknown coefficients are determined using the considered boundary conditions. The receptance method [19] requires to know the forced response of each subsystems under free boundary conditions. Due to this, and because the problem is being solved in the wavenumber domain, these boundary conditions have to be also transformed. Applying Eq. (A.3) to Eq. (B.10), the obtained transformed boundary conditions are

$$\begin{aligned} \left.\left(\frac{\mathrm{d}^3\bar{W}_p}{\mathrm{d}y_p^3} - (2-\nu_p)k_x^2\frac{\mathrm{d}\bar{W}_p}{\mathrm{d}y_p}\right)\right|_{y_p=0,L_p} &= 0, \\ \left.\left(\frac{\mathrm{d}^2\bar{W}_p}{\mathrm{d}y_p^2} - \nu_p k_x^2 \bar{W}_p\right)\right|_{y_p=0,L_p} &= 0. \end{aligned} \tag{3.11}$$

Substituting Eq. (3.9) into Eq. (3.11), two systems of equations of the following form are obtained

$$\begin{pmatrix} c_{11}^{I/II} & c_{12}^{I/II} & c_{13}^{I/II} & c_{14}^{I/II} \\ c_{21}^{I/II} & c_{22}^{I/II} & c_{23}^{I/II} & c_{24}^{I/II} \\ c_{31}^{I/II} & c_{32}^{I/II} & c_{33}^{I/II} & c_{34}^{I/II} \\ c_{41}^{I/II} & c_{42}^{I/II} & c_{43}^{I/II} & c_{44}^{I/II} \end{pmatrix} \begin{pmatrix} A^{I/II} \\ B^{I/II} \\ C^{I/II} \\ D^{I/II} \end{pmatrix} = \begin{pmatrix} 0 \\ 0 \\ 0 \\ 0 \end{pmatrix} \tag{3.12}$$

one for each case.

A nontrivial solution of Eq. (3.12) is only obtained when the determinant of the matrix of coefficients c_{ij} is 0. For each value of the wavenumber, a discrete set of frequencies ω_n verifies this condition. These are the eigenfrequencies of the problem. For each of them, the previous equation is an undetermined system where a solution $\bar{W}_n$ with an arbitrary amplitude can still be obtained. These solutions are the eigenfunctions of the problem. To simplify the performed calculations, the eigenfunctions are obtained discarding the last equation of the undetermined system.

For case I ($\kappa^2 > k_x^2$), the nonzero coefficients of Eq. (3.12) are

$$\begin{aligned}
&c_{12}^I = -\zeta_2^2 + k_x^2\nu_p, && c_{14}^I = \zeta_1^2 - k_x^2\nu_p,\\
&c_{21}^I = (-\zeta_2^2 + k_x^2\nu_p)\sin(\zeta_2 L_p), && c_{22}^I = (-\zeta_2^2 + k_x^2\nu_p)\cos(\zeta_2 L_p),\\
&c_{23}^I = (\zeta_1^2 - k_x^2\nu_p)\sinh(\zeta_1 L_p), && c_{24}^I = (\zeta_1^2 - k_x^2\nu_p)\cosh(\zeta_1 L_p),\\
&c_{31}^I = -\zeta_2[\zeta_2^2 + k^2(2-\nu_p)], && c_{33}^I = \zeta_1[\zeta_1^2 - k^2(2-\nu_p)],\\
&c_{41}^I = -\zeta_2[\zeta_2^2 + k^2(2-\nu_p)]\cos(\zeta_2 L_p), && c_{42}^I = \zeta_2[\zeta_2^2 + k_x^2(2-\nu_p)]\sin(\zeta_2 L_p),\\
&c_{43}^I = \zeta_1[\zeta_1^2 - k_x^2(2-\nu_p)]\cosh(\zeta_1 L_p), && c_{44}^I = \zeta_1[\zeta_1^2 - k_x^2(2-\nu_p)]\sinh(\zeta_1 L_p).
\end{aligned} \tag{3.13}$$

Defining

$$\gamma_1 = \kappa^2 + k_x^2(1-\nu_p), \qquad \gamma_2 = \kappa^2 - k_x^2(1-\nu_p) \tag{3.14}$$

the determinant of the matrix, known as the characteristic frequency equation of the problem, can be written as

$$2\zeta_1\zeta_2\gamma_1^2\gamma_2^2[\cosh(\zeta_1 L_p)\cos(\zeta_2 L_p) - 1] = \sinh(\zeta_1 L_p)\sin(\zeta_2 L_p)[\zeta_1^2\gamma_2^4 - \zeta_2^2\gamma_1^4]. \tag{3.15}$$

Omitting the arbitrary amplitude, the eigenfunctions can be written as

$$\begin{aligned}
\bar{W}_n(y_p) \quad = \quad & \zeta_2\gamma_1\sinh(\zeta_1 y_p) + \zeta_1\gamma_2\sin(\zeta_2 y_p)\\
& -\sigma_{FF}[\gamma_2\cosh(\zeta_1 y_p) + \gamma_1\cos(\zeta_2 y_p)],
\end{aligned} \tag{3.16}$$

where

$$\sigma_{FF} = \frac{\zeta_2\gamma_1^2\sinh(\zeta_1 L_p) - \zeta_1\gamma_2^2\sin(\zeta_2 L_p)}{\gamma_1\gamma_2[\cosh(\zeta_1 L_p) - \cos(\zeta_2 L_p)]}. \tag{3.17}$$

For case II ($\kappa^2 < k_x^2$), the nonzero coefficients are

$$\begin{aligned}
&c_{12}^{II} = \zeta_2'^2 - k_x^2\nu_p, && c_{14}^{II} = \zeta_1^2 - k_x^2\nu_p,\\
&c_{21}^{II} = (\zeta_2'^2 - k_x^2\nu_p)\sinh(\zeta_2' L_p), && c_{22}^{II} = (\zeta_2'^2 - k_x^2\nu_p)\cosh(\zeta_2' L_p),\\
&c_{23}^{II} = (\zeta_1^2 - k_x^2\nu_p)\sinh\zeta_1 L_p, && c_{24}^{II} = (\zeta_1^2 - k_x^2\nu_p)\cosh\zeta_1 L_p,\\
&c_{31}^{II} = \zeta_2'[\zeta_2'^2 - k_x^2(2-\nu_p)], && c_{33}^{II} = \zeta_1[\zeta_1^2 - k_x^2(2-\nu_p)],\\
&c_{41}^{II} = \zeta_2'[\zeta_2'^2 - k_x^2(2-\nu_p)]\cosh(\zeta_2' L_p), && c_{42}^{II} = \zeta_2'[\zeta_{'2}^2 - k_x^2(2-\nu_p)]\sinh(\zeta_2' L_p),\\
&c_{43}^{II} = \zeta_1[\zeta_1^2 - k_x^2(2-\nu_p)]\cosh(\zeta_1 L_p), && c_{44}^{II} = \zeta_1[\zeta_1^2 - k_x^2(2-\nu_p)]\sinh(\zeta_1 L_p).
\end{aligned} \tag{3.18}$$

The characteristic frequency equation can be written as

$$2\zeta_1\zeta_2'\gamma_1^2\gamma_2^2[\cosh(\zeta_1 L_p)\cosh(\zeta_2' L_p) - 1] = \sinh(\zeta_1 L_p)\sinh(\zeta_2' L_p)[\zeta_1^2\gamma_2^4 + \zeta_2'^2\gamma_1^4] \tag{3.19}$$

and the eigenfunctions can be written as

$$\begin{aligned}\bar{W}_n(y_p) &= \zeta_2^{'}\gamma_1 \sinh(\zeta_1 y_p) + \zeta_1\gamma_2 \sinh(\zeta_2^{'} y_p) \\ &\quad -\sigma_{FF}^{'}[\gamma_2 \cosh(\zeta_1 y_p) + \gamma_1 \cosh(\zeta_2^{'} y_p)], \end{aligned} \tag{3.20}$$

where

$$\sigma_{FF}^{'} = \frac{\zeta_2^{'}\gamma_1^2 \sinh(\zeta_1 L_p) - \zeta_1\gamma_2^2 \sinh(\zeta_2^{'} L_p)}{\gamma_1\gamma_2[\cosh(\zeta_1 L_p) - \cosh(\zeta_2^{'} L_p)]}. \tag{3.21}$$

Once both characteristic frequency equations are known, the frequency spectrum of the problem can be obtained. In Fig. (3.3), the spectrum is plotted considering the mechanical parameters specified in Table 3.1. The parameters used are typical values found in a reinforced concrete structure and are similar to the ones used in [1].

Parameter	Value
L_p	10.9 m
h_p	0.4 m
E_p	27.6 GPa
ν_p	0.175
ρ_p	3000 kg m^{-3}
η_p	0.02

Table 3.1: Mechanical parameters used to model the interior floor as a thin plate.

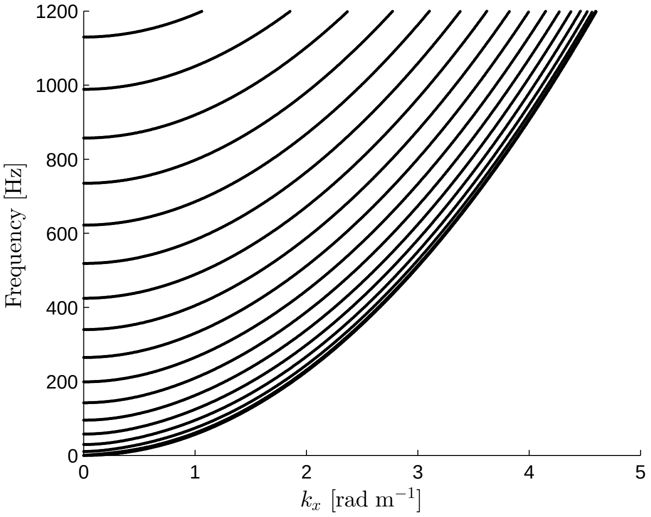

Fig. 3.3: Frequency spectrum of a free-free (F-F) strip plate.

3.3.3 Forced response

When the boundary conditions of a finite continuous system are of the form

$$\sum_{k=0}^{3} \mathrm{Coef}_k \frac{\mathrm{d}^k \bar{W}_p(y_p)}{\mathrm{d}y_p^k} = 0, \tag{3.22}$$

being Coef_k arbitrary constants, the problem eigenfunctions $\bar{W}_n$ are an infinite set of orthogonal functions. Then

$$\int_0^{L_p} \bar{W}_n(y_p)\bar{W}_m(y_p)\mathrm{d}y_p = \delta_{mn}C_n, \quad m, n = 1, 2, \ldots \tag{3.23}$$

where δ_{mn} is the Kronecker delta and where

$$C_n = \int_0^{L_p} \bar{W}_n(y_p)^2 \mathrm{d}y_p. \tag{3.24}$$

Considering the forced response $\bar{W}(y_p)$ and the applied load $\bar{P}(y_p)$ as linear combinations of the known eigenfunctions, the the forced response of the strip plate can be written as [103]

$$\bar{W}(y_p) = \sum_{n=1}^{\infty} \frac{\bar{W}_n(y_p)p_n}{D_p(\kappa_n^4 - \kappa^4)}, \tag{3.25}$$

where

$$p_n = \frac{1}{C_n}\int_0^{L_p} \bar{P}(y_p)\bar{W}_n(y_p)\mathrm{d}y_p \tag{3.26}$$

and where

$$\kappa_n = \left(\frac{\rho_p h_p \omega_n^2}{D_p}\right)^{1/4}. \tag{3.27}$$

The loss of energy due to microstructural mechanisms is modelled using hysteretic damping [19]. In this damping model, a complex Young modulus is defined as follows

$$E_p^* = E_p(1 + \mathrm{i}\eta_p), \tag{3.28}$$

where η_p is the loss factor of the interior floor. Due to this, Eq. (3.25) is rewritten as

$$\bar{W}_p(y_p) = \sum_{n=1}^{\infty} \frac{\bar{W}_n(y_p)p_n}{D_p(1 + \mathrm{i}\eta_p)(\kappa_n^4 - \kappa^4)}. \tag{3.29}$$

Substituting Eqs. (3.8) and (3.27) into (3.29), the following expression is obtained

$$\bar{W}_p(y_p) = \sum_{n=1}^{\infty} \frac{\bar{W}_n(y_p)p_n}{\omega_n^2 \rho_p h_p \left((1 + \mathrm{i}\eta_p) - \dfrac{\omega^2}{\omega_n^2} \right)}. \tag{3.30}$$

Rearranging the previous expression, the deflection of the plate can be finally written as

$$\bar{W}_p(y_p) = \sum_{n=1}^{\infty} \frac{\bar{W}_n(y_p)p_n \mathrm{e}^{\mathrm{i}\phi_n}}{C_n \rho_p h_p \sqrt{(\omega_n^2 - \omega^2)^2 + \omega_n^4 \eta_p^2}}, \tag{3.31}$$

where

$$\phi_n = \arctan\left(\frac{\eta_p}{1 - (\omega/\omega_n)^2} \right). \tag{3.32}$$

3.3.4 Response to point and distributed loads

A receptance is defined as the displacement (or slope) at Point/Line i caused by a harmonic unitary load (or moment) applied at Point/Line j. In this work, receptances are usually defined in the wavenumber domain instead of in the space domain and can be understood as the response at Line i to a spatially sinusoidal load applied at Line j [91]. For the case of the interior floor, these space and wavenumber receptances are named α_{ij} and $\bar{\alpha}_{ij}$, respectively.

Harmonic point load

A vertical harmonic point load applied at a Point 4, with coordinates $(0, y_4)$, is given by

$$p(x, y_p, t) = P(x, y_p)\mathrm{e}^{\mathrm{i}\omega t} = \delta(y_p - y_4)\delta(x)\mathrm{e}^{\mathrm{i}\omega t}. \tag{3.33}$$

Applying Eq. (A.3) to $P(x, y_p)$, the following wavenumber distribution of the load is obtained

$$\bar{P}(y_p) = \delta(y_p - y_4) \tag{3.34}$$

and the coefficients p_n, defined in Eq. (3.26), are in this case

$$p_n = \frac{1}{C_n} \int_0^{L_p} \bar{W}_n(y_p)\delta(y_p - y_4)\mathrm{d}y_p = \frac{1}{C_n}\bar{W}_n(y_4). \tag{3.35}$$

The receptance of the interior floor at Line i is obtained substituting Eq. (3.35) into Eq. (3.31). The result can be written as

$$\bar{\alpha}_{i4} = \sum_{n=1}^{\infty} \bar{W}_n(y_i)\bar{W}_n(y_4)B_n, \tag{3.36}$$

where

$$B_n = \frac{\mathrm{e}^{\mathrm{i}\phi_n}}{C_n\rho_p h_p\sqrt{(\omega_n^2-\omega^2)^2+\eta_p^2\omega_n^4}}. \tag{3.37}$$

The receptance in the space domain is obtained applying Eq. (A.4) to Eq. (3.36). The resulting expression is

$$\alpha_{i4} = \frac{1}{2\pi}\int_{-\infty}^{\infty}\sum_{n=1}^{\infty}\bar{W}_n(y_i)\bar{W}_n(y_4)B_n\mathrm{e}^{-\mathrm{i}k_x x_i}\mathrm{d}k_x. \tag{3.38}$$

where (x_i, y_i) are the coordinates of Point i.

Distributed load

The considered coupling loads between the interior floor and the tunnel are loads applied at certain position y_i and distributed along the x direction. They can be expressed as

$$p(x, y_p, t) = P(x, y_p)\mathrm{e}^{\mathrm{i}\omega t} = F(x)\delta(y_p - y_4)\mathrm{e}^{\mathrm{i}\omega t}, \tag{3.39}$$

where $F(x)$ is its distribution. The wavenumber distribution of the load is given by

$$\bar{P}(k_x, y_p) = \bar{F}(k_x)\delta(y_p - y_4) \tag{3.40}$$

and the load coefficients p_n are again given by Eq. (3.35).

The receptance of the interior floor in the wavenumber domain is again given by

$$\bar{\alpha}_{i4} = \frac{\bar{W}_p(k_x, y_p)}{\bar{F}(k_x)} = \sum_{n=1}^{\infty}\bar{W}_n(y_i)\bar{W}_n(y_4)B_n \tag{3.41}$$

while the response of the plate in the space domain is given by

$$W_p(x_i, y_i) = \frac{1}{2\pi}\int_{-\infty}^{\infty}\bar{\alpha}_{i4}\bar{F}\mathrm{e}^{-\mathrm{i}k_x x_i}\mathrm{d}k_x \tag{3.42}$$

The previous antitransform requires to know the wavenumber distribution of the load $\bar{F}$ to be analytically or numerically solved. Note that Eq. (3.38) is a particular case of Eq. (3.42) where $\bar{F} = 1$.

3.3.5 Numerical computation of the plate receptances

This subsection deals with some difficulties and considerations that have to be taken into account when the numerical computation of the previous expressions is done.

The form of the strip plate eigenfunctions presented in Eqs. (3.16) and (3.20) is not suitable for performing numerical calculations. For large arguments of the hyperbolic functions, inaccurate results are obtained. A procedure to solve this problem, for the case of beam eigenfunctions, has been presented by Gonçalves et al. [104]. This procedure, which involves to rearrange the eigenfunction expressions and to perform analytical approximations on them, is adapted here for the case of strip plate eigenfunctions.

Dividing Eq. (3.16) by $\zeta_2\gamma_1$ and making use of the equality

$$\sinh(\zeta_1 y_p) - \cosh(\zeta_1 y_p) = -\mathrm{e}^{-\zeta_1 y_p},$$

the eigenfunction can be expressed as

$$\bar{W}_n(y_p) = -\mathrm{e}^{-\zeta_1 y_p} + \nu_{FF}\cosh(\zeta_1 y_p) + \frac{\zeta_1\gamma_2}{\zeta_2\gamma_1}\sin(\zeta_2 y_p) - \frac{\sigma_{FF}}{\zeta_2}\cos(\zeta_2 y_p), \tag{3.43}$$

where

$$\nu_{FF} = 1 - \frac{\sigma_{FF}\gamma_2}{\zeta_2\gamma_1}. \tag{3.44}$$

Written this way, the chief cause of the numerical problems of the expression becomes clear. For large values of $\zeta_1 L_p$, ν_{FF} can be smaller than the typical resolution of the numerical computation softwares. When this happens, the product $\nu_{FF}\cosh(\zeta_1 y_p)$, is numerically considered zero despite having a significant contribution to the eigenfunction value. This problem can be avoided performing some analytical approximations before the numerical results are obtained. If ζ_1 is a large value, $\cosh(\zeta_1 L_p) >> \cos(\zeta_2 L_p)$, and

$$\begin{aligned}\nu_{FF}\cosh(\zeta_1 y_p) &= \left[\frac{\gamma_1^2 z_2 \mathrm{e}^{-\zeta_1 L_p} + \zeta_1\gamma_2^2\sin(\zeta_2 L_p) - \zeta_2\gamma_1^2\cos(\zeta_2 L_p)}{\gamma_1^2\zeta_2[\cosh(\zeta_1 L_p) - \cos(\zeta_2 L_p)]}\right]\cosh(\zeta_1 y_p) \\ &\approx \frac{\cosh(\zeta_1 y_p)}{\cosh(\zeta_1 L_p)}\left[\mathrm{e}^{-\zeta_1 L_p} + \frac{\zeta_1\gamma_2^2}{\zeta_2\gamma_1^2}\sin(\zeta_2 L_p) - \cos(\zeta_2 L_p)\right].\end{aligned} \tag{3.45}$$

Using also that

$$\frac{\cosh(\zeta_1 y_p)}{\cosh(\zeta_1 L_p)} \approx \mathrm{e}^{\zeta_1(y_p - L_p)} + \mathrm{e}^{-\zeta_1(y_p + L_p)}, \tag{3.46}$$

the unstable term can be finally written as

$$\nu_{FF}\cosh(\zeta_1 y_p) \approx \left[\mathrm{e}^{\zeta_1(y_p - L_p)} + \mathrm{e}^{-\zeta_1(y_p + L_p)}\right]\left[\frac{\zeta_1\gamma_2^2}{\zeta_2\gamma_1^2}\sin(\zeta_2 L_p) - \cos(\zeta_2 L_p)\right] \tag{3.47}$$

and the eigenfunction is no longer a numerically ill-behaved expression. An equivalent procedure has been done with Eq. (3.20).

The modal summation performed in the calculations of the interior floor receptances are truncated taking into account the frequency range of interest for the problem, which is usually taken as 1-200 Hz [74]. A detailed study of the convergence of the double-deck tunnel model is later described in Subsection 3.6.2.

Two additional considerations are worthy of mention because they avoid unnecessary calculations. One, the axial symmetry of the applied load implies a symmetrical response. Due to this, $\bar{\mathbf{U}}(k_x) = \bar{\mathbf{U}}(-k_x)$ and the number of numerical operations and the required storage memory can be almost halved. This property will also be used in the numerical computation of the global results. The other, because the strip plate eigenmodes are independent of the applied loads, they can be computed just once and be reused for each loading case studied.

3.3.6 Validation of the analytical expressions

This subsection presents a numerical comparison to ensure that the forced response of a strip plate has been correctly derived and computed. Two different calculations are performed. The first one, the edge loads of a simply supported-simply supported (SS-SS) strip plate excited by a harmonic point load. The second, the edge loads required in a F-F strip plate, excited again by a harmonic load, to ensure zero deflection at these points. If the harmonic load is applied at the same point for both strip plates and if the analytical expressions obtained and the numerical computation of them are correct, both results must be equal.

SS-SS Strip plate eigenmodes

As a previous step of the comparison, the forced response of a SS-SS strip plate is required. The SS-SS strip plate transformed boundary conditions are obtained applying Eq. (A.3) to Eq. (B.8). The resulting expressions are

$$\bar{W}_p\Big|_{y_p=0,L_p} = 0, \qquad \frac{\mathrm{d}^2\bar{W}_p}{\mathrm{d}y_p^2} - k_x^2\nu_p\bar{W}_p\Big|_{y_p=0,L_p} = 0. \tag{3.48}$$

For these boundary condition, it can be demonstrated [21] that eigenfrequencies are only obtained when $\kappa^2 > k_x^2$. Substituting Eq. (3.9) into Eq. (3.48) the following nonzero coefficients are obtained

$$\begin{aligned}
&c^I_{12} = 1, && c^I_{14} = 1,\\
&c^I_{21} = \sin(\zeta_2 L_p), && c^I_{22} = \cos(\zeta_2 L_p),\\
&c^I_{23} = \sinh(\zeta_1 L_p), && c^I_{24} = \cosh(\zeta_1 L_p),\\
&c^I_{32} = -(\zeta_2^2 + \nu_p k_x^2), && c^I_{34} = \zeta_1^2 - \nu_p k_x^2,\\
&c^I_{41} = -(\zeta_2^2 + \nu_p k_x^2)\sin(\zeta_2 L_p), && c^I_{42} = -(\zeta_2^2 + \nu_p k_x^2)\cos(\zeta_2 L_p),\\
&c^I_{43} = (\zeta_1^2 - \nu_p k_x^2)\sinh(\zeta_1 L_p), && c^I_{44} = (\zeta_1^2 - \nu_p k_x^2)\cosh(\zeta_1 L_p).
\end{aligned} \tag{3.49}$$

Operating, the characteristic equation is reduced to

$$\sin(\zeta_2 L_p) = 0 \tag{3.50}$$

and the problem eigenfunctions are given by

$$\bar{W}_n(y_p) = \sin(\zeta_2 y_p). \tag{3.51}$$

The forced response is again given by Eq. (3.36), considering now the SS-SS strip plate eigenmodes instead of the F-F ones. Once the response has been antitransformed to the space domain using Eq. (A.4), the edge loads are obtained using Eq. (B.7).

Response comparison

Fig 3.4 presents a cross-section of a F-F strip plate with an harmonic point load applied at Point 4 and two harmonic distributed loads at both edges of the plate, defined as Lines 1 and 2. The x-direction distribution of the loads is not drawn but, because the problem is solved in the wavenumber domain, only the untransformed dimensions are of interest.

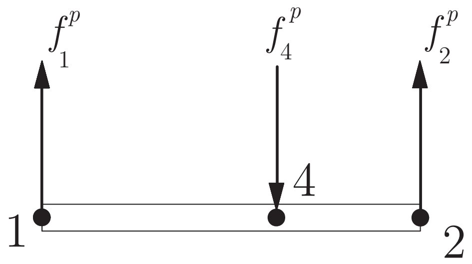

FIG. 3.4: Free body diagram of the interior floor

For the considered loads, the deflection of a F-F strip plate $\bar{W}_p^F$ is given by

$$\bar{W}_p^F(y_p) = -\bar{F}_1 \bar{\alpha}_{i1}^F - \bar{F}_2 \bar{\alpha}_{i2}^F + \bar{\alpha}_{i4}^F, \tag{3.52}$$

where $\bar{\alpha}_{ij}^{F}$ are the receptances of the F-F strip plate to a point load and where $\bar{F}_1$ and $\bar{F}_2$ are the wavenumber distributions of the edge loads, which are unknown.

Imposing that $\bar{W}_p^F(0) = \bar{W}_p^F(L_p) = 0$, the following system of equations is obtained

$$\begin{pmatrix} \bar{F}_1 \\ \bar{F}_2 \end{pmatrix} = \begin{pmatrix} \bar{\alpha}_{11}^F & \bar{\alpha}_{12}^F \\ \bar{\alpha}_{21}^F & \bar{\alpha}_{22}^F \end{pmatrix}^{-1} \begin{pmatrix} \bar{\alpha}_{1j}^F \\ \bar{\alpha}_{2j}^F \end{pmatrix}. \tag{3.53}$$

The space distribution of the edge loads F_1 and F_2 are obtained applying Eq. (A.4) to $\bar{F}_1$ and $\bar{F}_2$.

For the case of a SS-SS strip plate, its deflection $\bar{W}_p^{SS}$ when an harmonic point load is applied at Point 4 is given by

$$\bar{W}_p^{SS}(y_p) = \bar{\alpha}_{ij}^{SS}. \tag{3.54}$$

The strip plate deflection in the space domain $W_p^{SS}(y_p)$ is obtained applying Eq. (A.4) to Eq. (3.54) and the edge forces $V_y(y_p)$ are calculated using Eq. (B.7).

Fig 3.5 compares the edge loads F_1 and V_y at four different cross-sections of the strip plate. The mechanical parameters of the plate are those defined in Table 3.1 and the harmonic point load is applied at $y_4 = 5.45$ m. The inverse Fourier transform have been computed considering $N = 2048$ samples and a space resolution of $\Delta x = 0.5$ m. More details of how this numerical integration is performed are presented in Appendix A. A truncation frequency of 4800 Hz has been chosen in order to obtain accurate results (see Section 3.6 for a justification of this truncation value). The chosen cross-sections are x_m = 0, 20, 50 and 100 m.

The results show a perfect match between both loads for all the cross-sections considered. This result ensures that the modal summation has been correctly calculated and computed.

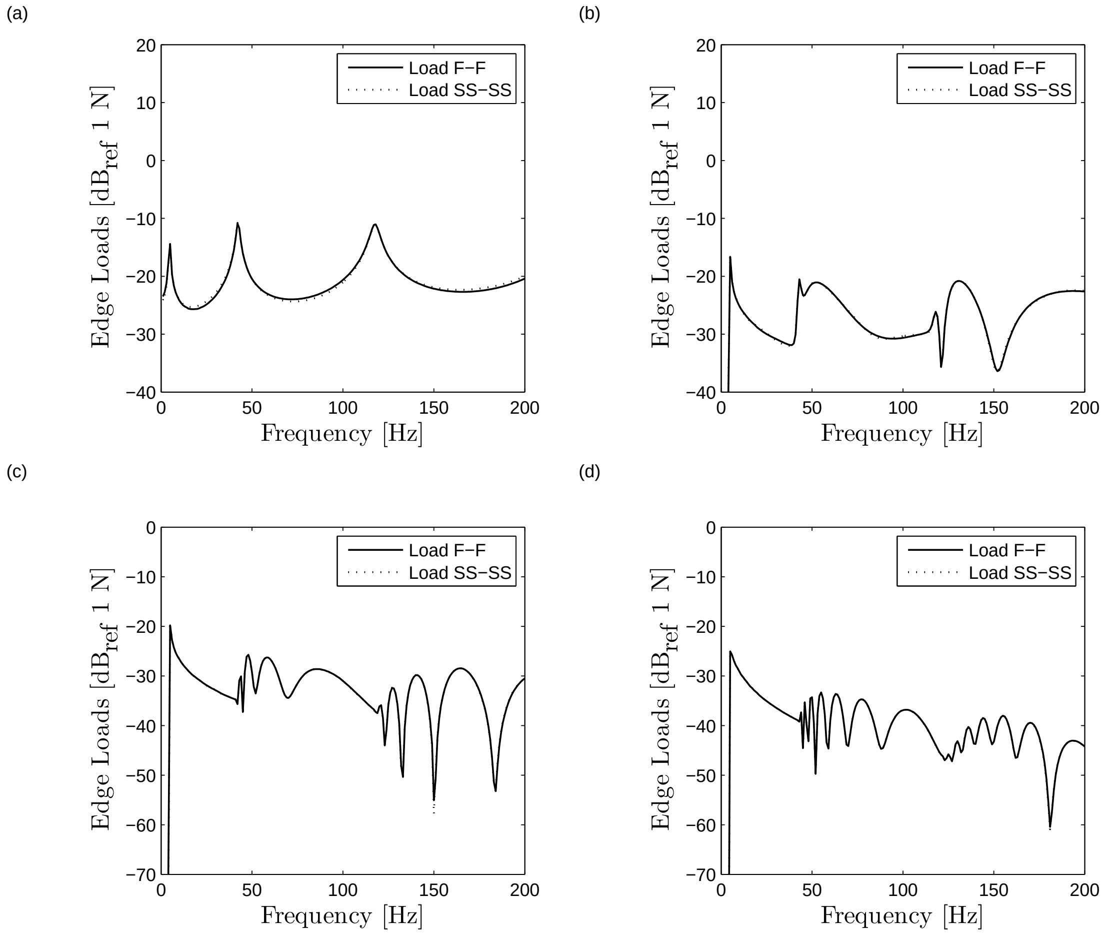

FIG. 3.5: Comparison between the edge loads of a SS-SS strip plate and the external loads required to apply to a F-F strip plate to behave as the first one. The cross-sections considered are: (a) $x_m = 0$ m, (b) $x_m = 20$ m, (c) $x_m = 50$ m and (d) $x_m = 100$ m.

3.4 Tunnel-soil model

3.4.1 Model hypothesis

The soil and the tunnel dynamics are described using the PiP model derived by Forrest and Hunt [17]. In their work, the tunnel is assumed to behave as a thin cylindrical shell and the soil is modelled as an infinite linear isotropic homogeneous elastic media. The coupling between both systems is done in the wavenumber-frequency domain considering that, at the interface, their displacement fields are equal and that the stress fields caused by one subsystem to the other are equal in magnitude and of opposite sign. The initial formulation, which assumed symmetric loads respect to the angular coordinate θ, was later extended to antisymmetric loads by Hussein and Hunt [88]. Both formulations of the model are presented in Appendix D. The positive directions considered for the

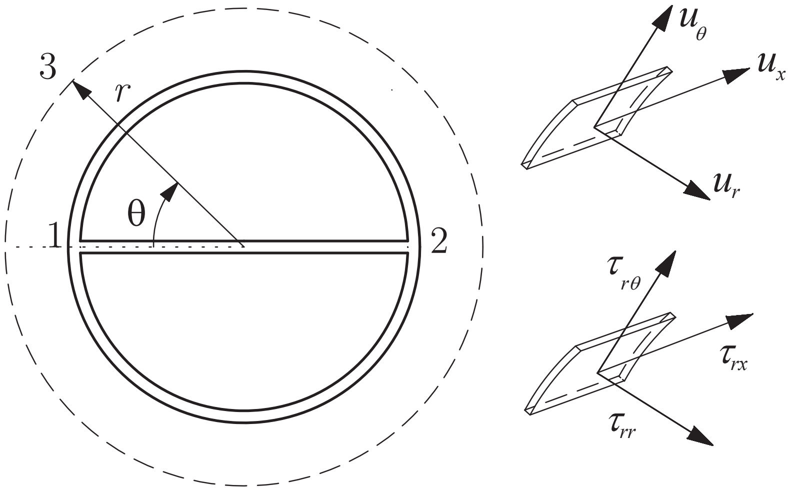

FIG. 3.6: Cross-section of the double-deck circular tunnel model with the chosen system of coordinates and the positive directions considered for the displacement and stress fields.

displacements (u_x, u_θ and u_r) and stresses (τ_{rx}, $\tau_{r\theta}$ and τ_{rr}) and the chosen system of coordinates (x, θ, r) are presented in Fig. 3.6.

In this work, because the external loads are tangential and applied at two opposite points of the tunnel (see Section 3.5), the origin of the angular coordinate θ has been changed from the original PiP formulation and only the antisymmetric formulation is required to obtain the resulting displacements. Due to this, the displacement and stress fields can be written as

$$\bar{\mathbf{U}} = \sum_{n=0}^{\infty} \mathbf{S}^a \bar{\mathbf{U}}_n^a, \qquad \bar{\mathbf{T}} = \sum_{n=0}^{\infty} \mathbf{S}^a \bar{\mathbf{T}}_n^a, \tag{3.55}$$

where $\mathbf{S}^a$ is defined in Eq. (D.3). Using Eqs. (D.25) and (D.26), the stress and displacement fields are given by

$$\bar{\mathbf{U}} = \sum_{n=0}^{\infty} \mathbf{S}^a \mathbf{M}^a \bar{\mathbf{P}}_n, \qquad \bar{\mathbf{T}} = \sum_{n=0}^{\infty} \mathbf{S}^a \mathbf{K}^a \bar{\mathbf{P}}_n, \tag{3.56}$$

where the Fourier coefficients $\bar{\mathbf{P}}_n$ are obtained by transforming and decomposing the applied tangential load and where $\mathbf{M}^a$ and $\mathbf{K}^a$ are defined in Eqs. (D.27) and (D.28). To simplify the notation the superscript a will be omitted during the rest of the section.

3.4.2 Receptance to a distributed tangential load

In the proposed model for a double-deck tunnel, two tangential coupling loads are applied along Lines 1 and 2 of the tunnel's interior surface. Using the Dirac's delta definition in cylindrical coordinates these loads can be expressed as

$$\mathbf{p}_1 = \begin{pmatrix} 0 \\ P_{\theta,1}(x) \\ 0 \end{pmatrix} \frac{\delta(\theta)}{r_t} \mathrm{e}^{\mathrm{i}\omega t}, \qquad \mathbf{p}_2 = \begin{pmatrix} 0 \\ P_{\theta,2}(x) \\ 0 \end{pmatrix} \frac{\delta(\theta - \pi)}{r_t} \mathrm{e}^{\mathrm{i}\omega t}, \tag{3.57}$$

where $P_{\theta,1}(x)$ and $P_{\theta,2}(x)$ are the axial unknown distributions of the coupling loads. As is detailed in Section D.4, these loads are transformed to the wavenumber domain and decomposed in Fourier series. For $\mathbf{p}_1$, the transformed coefficients are

$$\bar{\mathbf{P}}_0 = \frac{1}{2r_t\pi} \begin{pmatrix} 0 \\ \bar{P}_{\theta,1}(k_x) \\ 0 \end{pmatrix}, \qquad \bar{\mathbf{P}}_n = \frac{1}{r_t\pi} \begin{pmatrix} 0 \\ \bar{P}_{\theta,1}(k_x) \\ 0 \end{pmatrix}. \tag{3.58}$$

For $\mathbf{p}_2$ the coefficients are

$$\bar{\mathbf{P}}_0 = \frac{1}{2r_t\pi} \begin{pmatrix} 0 \\ \bar{P}_{\theta,2}(k_x) \\ 0 \end{pmatrix}, \qquad \bar{\mathbf{P}}_n = \frac{(-1)^n}{r_t\pi} \begin{pmatrix} 0 \\ \bar{P}_{\theta,2}(k_x) \\ 0 \end{pmatrix}. \tag{3.59}$$

The receptances of the PiP are defined in this work as $\bar{\boldsymbol{\beta}}_{ij}$. They can be understood as the response of a Line i to a sinusoidally varying load applied at Line j. In the most general case, this receptance is a 3×3 matrix of the following form

$$\bar{\boldsymbol{\beta}}_{ij} = \begin{pmatrix} \beta_{ix,jx} & \beta_{ix,j\theta} & \beta_{ix,jr} \\ \beta_{i\theta,jx} & \beta_{i\theta,j\theta} & \beta_{i\theta,jr} \\ \beta_{ir,jx} & \beta_{ir,j\theta} & \beta_{ir,jr} \end{pmatrix}. \tag{3.60}$$

Using this notation, the receptances to loads $\mathbf{p}_1$ and $\mathbf{p}_2$ are named as $\bar{\boldsymbol{\beta}}_{i,1\theta}$ and $\bar{\boldsymbol{\beta}}_{i,2\theta}$ respectively. These receptances are obtained operating Eq. (3.58) and (3.59) with Eqs. (D.25) and (3.56). The resulting expressions can be written as

$$\bar{\boldsymbol{\beta}}_{i,1\theta} = \frac{1}{2r_t\pi} \begin{pmatrix} 0 \\ m_{22,0} \\ 0 \end{pmatrix} + \sum_{n=1}^{\infty} \frac{1}{r_t\pi} \begin{pmatrix} m_{12,n}\sin(n\theta_i) \\ m_{22,n}\cos(n\theta_i) \\ m_{32,n}\sin(n\theta_i) \end{pmatrix} \tag{3.61}$$

and

$$\bar{\boldsymbol{\beta}}_{i,2\theta} = \frac{1}{2r_t\pi}\begin{pmatrix} 0 \\ m_{22,0} \\ 0 \end{pmatrix} + \sum_{n=1}^{\infty}\frac{(-1)^n}{r_t\pi}\begin{pmatrix} m_{12,n}\sin(n\theta_i) \\ m_{22,n}\cos(n\theta_i) \\ m_{32,n}\sin(n\theta_i) \end{pmatrix}, \tag{3.62}$$

where $m_{ij,n}$ refers to the n-th ring mode of the ij component of the matrix $\mathbf{M}$ and θ_i is the angular position of Line i.

Similar expressions can be obtained for the stress fields caused by the considered tangential loads if the coefficients $m_{ij,n}$ are replaced by the coefficients $k_{ij,n}$, defined as the n-th ring modes of the ij component of the matrix $\mathbf{K}$. As in the interior floor case, the resulting displacement at a particular point of the Line i can be obtained antitransforming Eqs. (3.61) or (3.62).

3.4.3 Numerical computation of the PiP receptances

The modal summation is again truncated considering the frequency range of interest for the considered problem [74]. For computing the receptances of the PiP model, a finite number of ring modes have to be considered in Eqs. (3.61) and (3.62). A study of the convergence of the model respect this parameter is performed in Subsection 3.6.2.

Another difficulty to overcome in the numerical implementation of the model is that the matrix inversions performed in Eqs. (D.27) and (D.28) are inversions of bad conditioned matrices. To avoid the numerical problems caused by these inversions, the equations have been solved using an **LU** decomposition for complex valued matrices.

The mechanical parameters used to modelise the tunnel as a thin cylindrical shell and the soil as an linear homogeneous isotropic elastic media are presented in Tables 3.2 and 3.3. The tunnel parameters are equal to the interior floor ones, which are typical values for a reinforced concrete. For the case of soil, the values represent a soft tertiary ground. Hysteretic damping has been considered in the tunnel and in the soil. The damping definitions and the relations between the different elastic constants are presented in Section C.2.

Parameter	Value
r_t	5.65 m
h_t	0.4 m
E_t	27.6 GPa
ν_t	0.175
ρ_t	3000 kg m^{-3}
D_{E_t}	0.02

TABLE 3.2: Mechanical parameters used to model the tunnel as a thin shell.

Parameter	Value
E_s	100 MPa
ν_s	0.3
ρ_s	1950 kg m^{-3}
D_P	0.03
D_S	0.03

TABLE 3.3: Mechanical parameters used to model the soil as an elastic continuum.

3.5 Coupling of the systems

The coupling of the interior floor and the tunnel-soil systems is done using the receptance method [19]. The interaction between the tunnel walls and the interior floor of a double-deck tunnel depends on the construction method used to build it. This work focuses in the case where the interior floor is a separate precast slab structure supported on the tunnel walls, which is modelled using simply supported connections at both edges of the interior floor. As can be seen in Fig. 3.1, the interior floor is considered to be simply supported at Lines 1 and 2 of the tunnel structure. The interior floor is also excited by a vertical harmonic load applied at Point 4. Fig. 3.7 presents the free body diagrams of both systems. The distribution of the loads in the x-direction has been omitted because the problem is solved in the wavenumber domain.

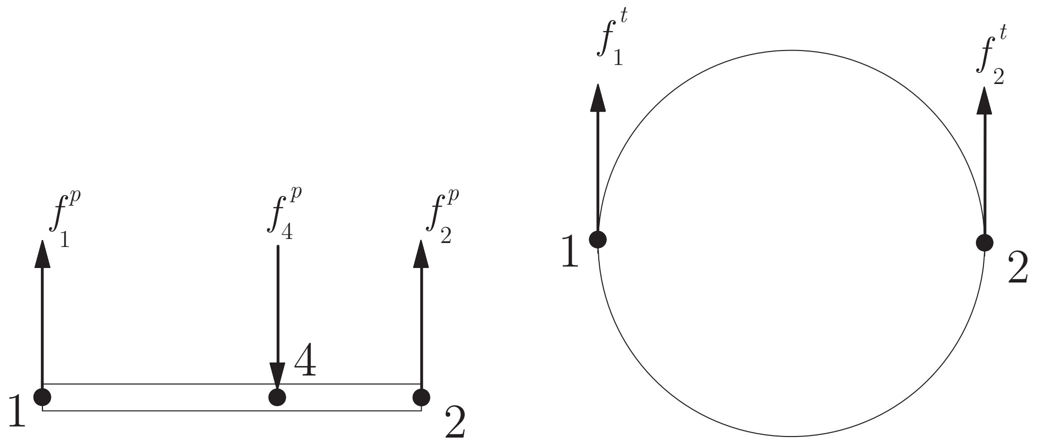

FIG. 3.7: (a) Free body diagram of the interior floor. (b) Free body diagram of the tunnel-soil system.

The transformed deflection of the interior floor can be written as

$$\bar{W}_p(y_i) = -\bar{\alpha}_{i1}\bar{F}_1^p - \bar{\alpha}_{i2}\bar{F}_2^p + \bar{\alpha}_{i4}\bar{F}_4^p, \tag{3.63}$$

where $\bar{F}_4^p$, $\bar{F}_1^p$ and $\bar{F}_2^p$ are the wavenumber distributions of the external load and of the coupling loads respectively.

The transformed displacement field of the tunnel is given by

$$\begin{pmatrix} \bar{U}_{ix}^t \\ \bar{U}_{i\theta}^t \\ \bar{U}_{ir}^t \end{pmatrix} = \begin{pmatrix} \bar{\beta}_{ix,1\theta} \\ \bar{\beta}_{i\theta,1\theta} \\ \bar{\beta}_{ir,1\theta} \end{pmatrix} \bar{F}_1^t - \begin{pmatrix} \bar{\beta}_{ix,2\theta} \\ \bar{\beta}_{i\theta,2\theta} \\ \bar{\beta}_{ir,2\theta} \end{pmatrix} \bar{F}_2^t. \tag{3.64}$$

where $\bar{F}_1^t$ and $\bar{F}_2^t$ are the transformed unknown loads exerted on the tunnel by the plate.

To model the coupling of both structures, the following set of conditions is considered

$$\begin{aligned} \bar{W}_p(0) &= -\bar{U}_{1\theta}^t, & \bar{F}_1^p &= -\bar{F}_1^t, \\ \bar{W}_p(L_p) &= \bar{U}_{2\theta}^t, & \bar{F}_2^p &= -\bar{F}_2^t. \end{aligned} \tag{3.65}$$

The coupling loads are obtained by substituting Eqs. (3.63) and (3.64) into Eq. (3.65)

$$\begin{pmatrix} -(\bar{\alpha}_{1,1} + \bar{\beta}_{1\theta,1\theta}) & -\bar{\alpha}_{1,2} + \bar{\beta}_{1\theta,2\theta} \\ -\bar{\alpha}_{2,1} + \bar{\beta}_{2\theta,1\theta} & -(\bar{\alpha}_{2,2} + \bar{\beta}_{2\theta,2\theta}) \end{pmatrix} \begin{pmatrix} \bar{F}_1^t \\ \bar{F}_2^t \end{pmatrix} = \begin{pmatrix} \bar{\alpha}_{1,4} \\ \bar{\alpha}_{2,4} \end{pmatrix} \bar{F}_4^p. \tag{3.66}$$

The required plate receptances in Eq. (3.66) are obtained from Eq. (3.41). Two considerations can be taken into account to avoid unnecessary calculations. One, because the plate modes are symmetric or antisymmetric, $\bar{\alpha}_{11} = \bar{\alpha}_{22}$. The other, due to the Maxwell reciprocity principle, $\bar{\alpha}_{12} = \bar{\alpha}_{21}$.

The required PiP receptances in Eq. (3.66) are given by the tangential component of Eqs. (3.61) and (3.62). The resulting expressions are

$$\begin{aligned} \bar{\beta}_{1\theta,1\theta} &= \bar{\beta}_{2\theta,2\theta} = \frac{m_{22,0}}{2r_t\pi} + \frac{1}{r_t\pi}\sum_{n=1}^{\infty} m_{22,n}, \\ \bar{\beta}_{1\theta,2\theta} &= \bar{\beta}_{2\theta,1\theta} = \frac{m_{22,0}}{2r_t\pi} + \frac{1}{r_t\pi}\sum_{n=1}^{\infty} m_{22,n}(-1)^n. \end{aligned} \tag{3.67}$$

With the coupling loads calculated, the displacement fields of each subsystem can be obtained using Eqs. (3.63) and (3.64). The displacement fields in the space domain can be finally obtained antitransforming. They can be expressed as

$$\begin{aligned} W_p(y_i) &= \frac{1}{2\pi}\int_{-\infty}^{\infty} \bar{\gamma}_{i4}^p \bar{F}_4^p \mathrm{e}^{-\mathrm{i}k_x x}\mathrm{d}k_x, \\ \mathbf{U}_i^t &= \frac{1}{2\pi}\int_{-\infty}^{\infty} \bar{\gamma}_{i4}^t \bar{F}_4^p \mathrm{e}^{-\mathrm{i}k_x x}\mathrm{d}k_x, \end{aligned} \tag{3.68}$$

where $\bar{\gamma}_{i4}^p$ is the interior floor receptance of a double-deck tunnel model to a point load applied at Line 4 of the interior floor and $\bar{\gamma}_{i4}^t$ is the tunnel-soil receptance of a double-deck tunnel to the same load.

3.5.1 Other types of loads

In the space domain, the response of a linear system to any type of loading distribution can be obtained as a superposition of point loads responses by means of the convolution product. This convolution product becomes a direct product when the problem is transformed to the wavenumber domain. This fact is easily seen in Eqs. (3.68), where the response to a particular load distribution $\bar{F}_4^p(k_x)$ is generated from the point load case, in which $\bar{F}_4^p = 1$. In this section, two types of loads used to represent simplified train models are considered: A finite harmonic line load and an infinite multipoint load.

Finite harmonic line load

A finite line load can be written as

$$F_4^p(x) = \frac{1}{L_t}\left[H\left(x + \frac{L_t}{2}\right) - H\left(x - \frac{L_t}{2}\right)\right], \tag{3.69}$$

where L_t is the lenght of the considered line and where $H(x)$ is the Heaviside step function. Its transformed expression is

$$\bar{F}_4^p(k_x) = \mathrm{sinc}\left(\frac{k_x L_t}{2}\right), \tag{3.70}$$

where $\mathrm{sinc}(x) = \sin(x)/x$.

The response of a doble-deck tunnel to this type of load is obtained substituting Eq. (3.70) into Eq. (3.68). The Fourier inverse transform has to be calculated numerically. Methods to compute this numerical integration are presented in Appendix A. In this work, the Fast Fourier Transform (FFT) algorithm is the numerical method used to solve these integrals.

Infinite multipoint load

An infinite set of equispaced points can be described by

$$F_4^p(x) = \sum_{n=-\infty}^{\infty} \delta(x - nL_p), \tag{3.71}$$

where L_p is the distance between loads. Using the distribution equality

$$\sum_{n=-\infty}^{\infty} \mathrm{e}^{2\pi \mathrm{i} n t} = \sum_{n'=-\infty}^{\infty} \delta(n' - t),$$

the transformed expression of this type of load can be written as

$$\bar{F}_4^p(k_x) = \sum_{n=-\infty}^{\infty} \mathrm{e}^{\mathrm{i}k_x n L_p} = \sum_{n'=-\infty}^{\infty} \delta\left(n' - \frac{k_x L_p}{2\pi}\right). \tag{3.72}$$

This type of wavenumber distribution allows to perform an additional analytical step. If Eq. (3.72) is substituted into the first one of Eqs. (3.68), the following interior floor deflection is obtained

$$\begin{aligned} W_p(y_i) &= \frac{1}{2\pi}\int_{-\infty}^{\infty} \bar{\gamma}_{i4}^p(k_x) \sum_{n'=-\infty}^{\infty} \delta\left(n' - \frac{k_x L_p}{2\pi}\right) \mathrm{e}^{-\mathrm{i}k_x x} \mathrm{d}k_x \\ &= \frac{1}{2\pi} \sum_{n'=-\infty}^{\infty} \bar{\gamma}_{i4}^p \left(\frac{2\pi n}{L_p}\right) \mathrm{e}^{\left(\frac{-\mathrm{i}2\pi n x}{L_p}\right)}. \end{aligned} \tag{3.73}$$

The solution is obtained as an sum of discrete values instead of an integral. Because the receptance of the system decays for large values of $\frac{2\pi n}{L_p}$, this infinite sum is reduced to a finite one in the region where $\bar{\gamma}_{i4}^{p}$ is significant.

3.6 Numerical results

3.6.1 Maximum displacement magnitude

To perform the comparisons between a simple-tunnel and a double-deck tunnel, the maximum displacement magnitude will be used. Considering a harmonic displacements of the form

$$u_i = |U_i| \sin(\omega t + \varphi_i), \tag{3.74}$$

where u_i is any of the three ortogonal components of the displacement and where

$$\varphi_i = \arctan\left(\frac{\mathrm{Im}(U_i)}{\mathrm{Re}(U_i)}\right), \tag{3.75}$$

the displacement magnitude can be expressed as

$$u_R^2 = \sum_{i=1}^{3} u_i^2 = \sum_{i=1}^{3} \left[U_i^2 \sin^2(\omega t + \varphi_i)\right]. \tag{3.76}$$

Using trigonometric identities, Eq. (3.76) can be rewritten as

$$u_R^2 = \sum_{i=1}^{3} \frac{U_i^2}{2} - \mathfrak{c}\cos(2\omega t) + \mathfrak{s}\sin(2\omega t), \tag{3.77}$$

where

$$\mathfrak{s} = \sum_{i=1}^{3} \left[\frac{U_i^2}{2}\sin(2\varphi_i)\right], \quad \mathfrak{c} = \sum_{i=1}^{3} \left[\frac{U_i^2}{2}\cos(2\varphi_i)\right]. \tag{3.78}$$

The maximum value of u_R^2 occurs when ωt satisfies

$$\frac{\mathrm{d}u_R^2}{\mathrm{d}(\omega t)} = 0, \tag{3.79}$$

resulting in the condition

$$\sin(2\omega t)\mathfrak{c} = \cos(2\omega t)\mathfrak{s}. \tag{3.80}$$

Combining Eq. (3.80) with $\sin^2(2\omega t) + \cos^2(2\omega t) = 1$, the following relations are obtained

$$\sin(2\omega t) = \pm\frac{\mathfrak{s}}{\sqrt{\mathfrak{s}^2 + \mathfrak{c}^2}}, \quad \cos(2\omega t) = \pm\frac{\mathfrak{c}}{\sqrt{\mathfrak{s}^2 + \mathfrak{c}^2}}. \tag{3.81}$$

Substituting the previous expressions in Eq. (3.77) gives the value of the square of the maximum displacement magnitude

$$u_m^2 = \max\left(u_R^2\right) = \sum_{i=1}^{3} \frac{U_i^2}{2} + \sqrt{\mathfrak{s}^2 + \mathfrak{c}^2}. \tag{3.82}$$

3.6.2 Convergence of the model

The convergence of the results have been studied considering four different parameters: The number of samples N, the space resolution Δx, the eigenmodes truncation frequency f_t and the number of ring modes N_r. The results are obtained at $r = 10$ m and $\theta' = \pi/2$ rad. The maximum displacement magnitude is plotted at two different cross-sections: $x_m = 0$ m and $x_m = 40$ m. The convergence have been studied modifying one of the parameters each time and setting the others at values that ensure good convergence.

Space resolution

Fig. 3.8 presents the maximum displacement magnitude at the considered points for five values of the space resolution: $\Delta x = 4,\ 2,\ 1,\ 0.5$ and 0.25 m at the cross-section $x_m = 0$ m (subfigures (a) and (b)) and $x_m = 40$ m (subfigures (c) and (d)). The same size of the space sampling has been considered by setting a number of samples $N = 512,\ 1024,\ 2048,\ 4096$ and 8192 respectively. Due to this, a wavenumber resolution of $\pi/1024$ rad, a truncation frequency $f_t = 2400$ Hz and a number of ring modes $N_r = 20$ have been considered in all cases. Significant differences are only found between the first three space resolutions considered (subfigures (a) and (c)). Errors over 10 dB are found when $\Delta x = 4$ m and about 1 dB for high frequencies if $\Delta x = 2$ m. Smaller space samplings ensure that all the wavenumber content of the response is taken into account and correct results are obtained.

Truncation frequency

Fig. 3.9 presents the maximum displacement magnitude at the considered points for five values of the truncation frequency: 300, 600, 1200, 2400 and 4800 Hz. For all cases, $\Delta x = 0.25$ m, $N = 8192$ and $N_r = 20$. As can be seen, only for a truncation frequency of 300 Hz, the results show a significant lack of accuracy. At frequencies over 50 Hz, differences of about 3-4 dB are found. If $f_t = 600$ Hz, this differences are reduced to 0.5-1 dB. Accurate results around the spectrum peaks may require truncation frequencies up to 2400 Hz or even 4800 Hz. The relation between the desired precision of the

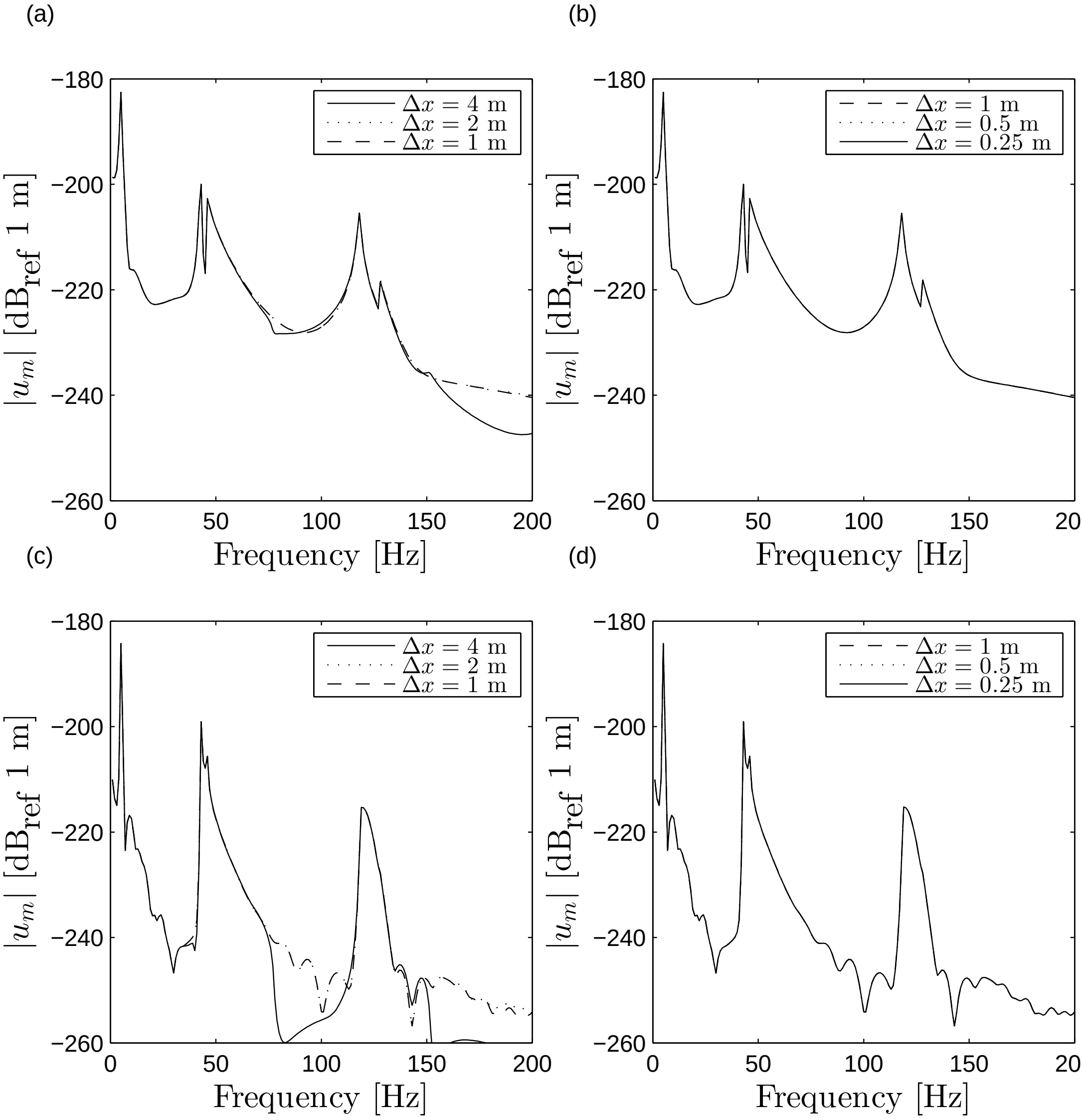

FIG. 3.8: Comparison of the maximum displacement magnitude at $r = 10$ m and $\theta = \pi/2$ rad for five different values of the space sampling resolution Δx. Two cross-sections have been considered: $x_m = 0$ m ((a) and (b)) and $x_m = 40$ m ((c) and (d)).

results and the computational cost required to obtain them is particulary delicate for this parameters. Also, as is detailed in Section 3.6.3, a high truncation frequency is also required when the coupling loads are studied.

Wavenumber resolution

Fig. 3.10 presents the results for five different number of samples $N = 512$, 1024, 2048, 4096 and 8192. Because the space sampling resolution is $\Delta x = 0.5$ m in all cases, this is equal to consider a wavenumber sampling resolution of $\Delta k = \pi/64$, $\pi/128$, $\pi/256$,

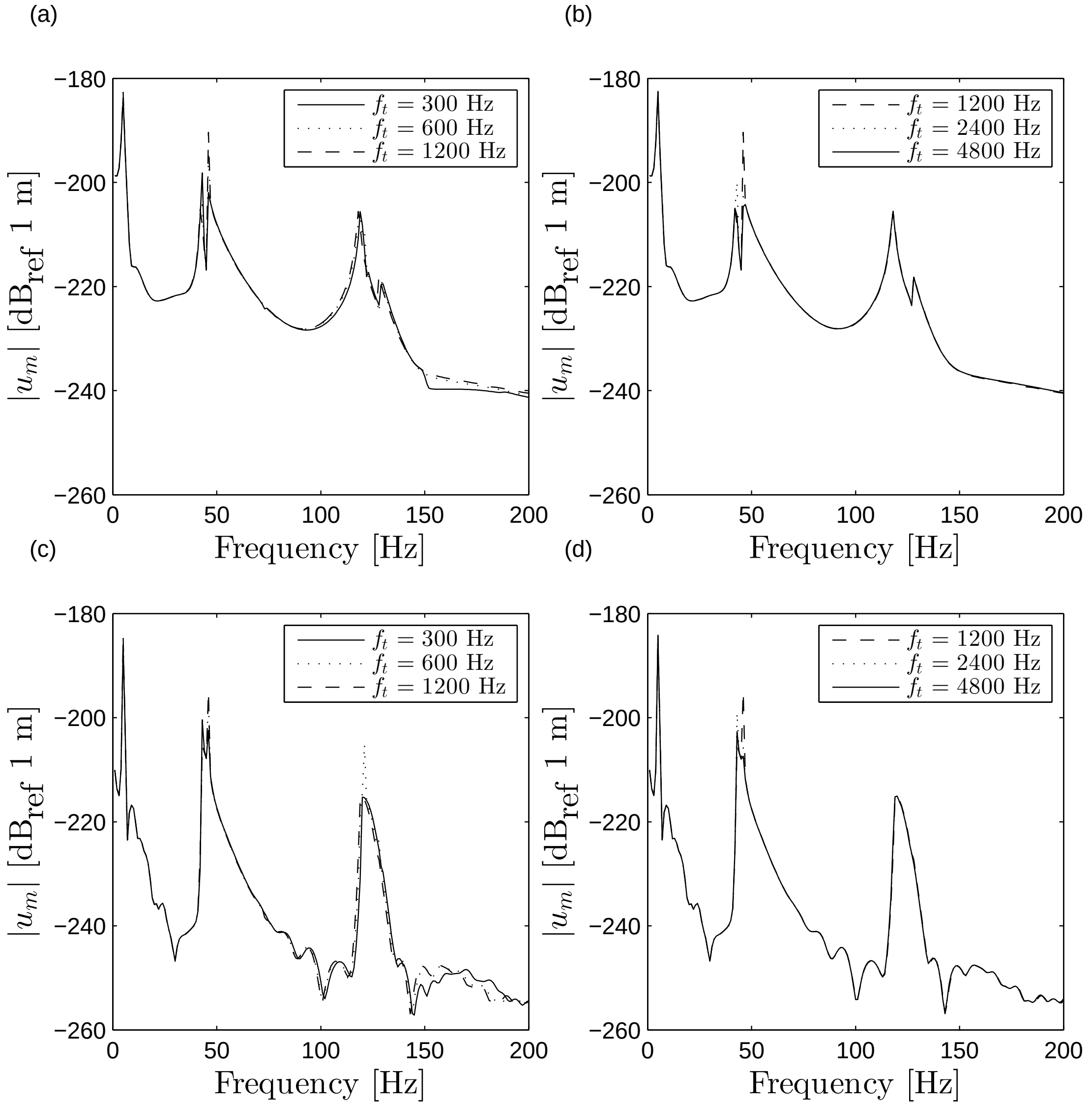

FIG. 3.9: Comparison of the maximum displacement magnitude at $r = 10$ m and $\theta = \pi/2$ rad for different values of the truncation frequency f_t Two cross-sections have been considered: $x_m = 0$ m ((a) and (b)) and $x_m = 40$ m ((c) and (d)).

$\pi/512$ and $\pi/1024$ rad respectively. In all cases, $f_t = 2400$ Hz and $N_r = 20$. When a bad wavenumber sampling is chosen the antitransformed displacement is not a smooth function. Differences near 10 dB are found if $N = 512$ samples. This differences are reduced to 0.5-2 dB if $N = 2048$ and are under 0.5 dB if $N = 4096$ samples. As it is explained in Appendix A, the lack of accuracy is caused by a bad sampling of the peaks found in $\bar{\boldsymbol{U}}$. This problem could be properly solved choosing a wiser sampling distribution instead of using an equispaced one with a huge number of samples.

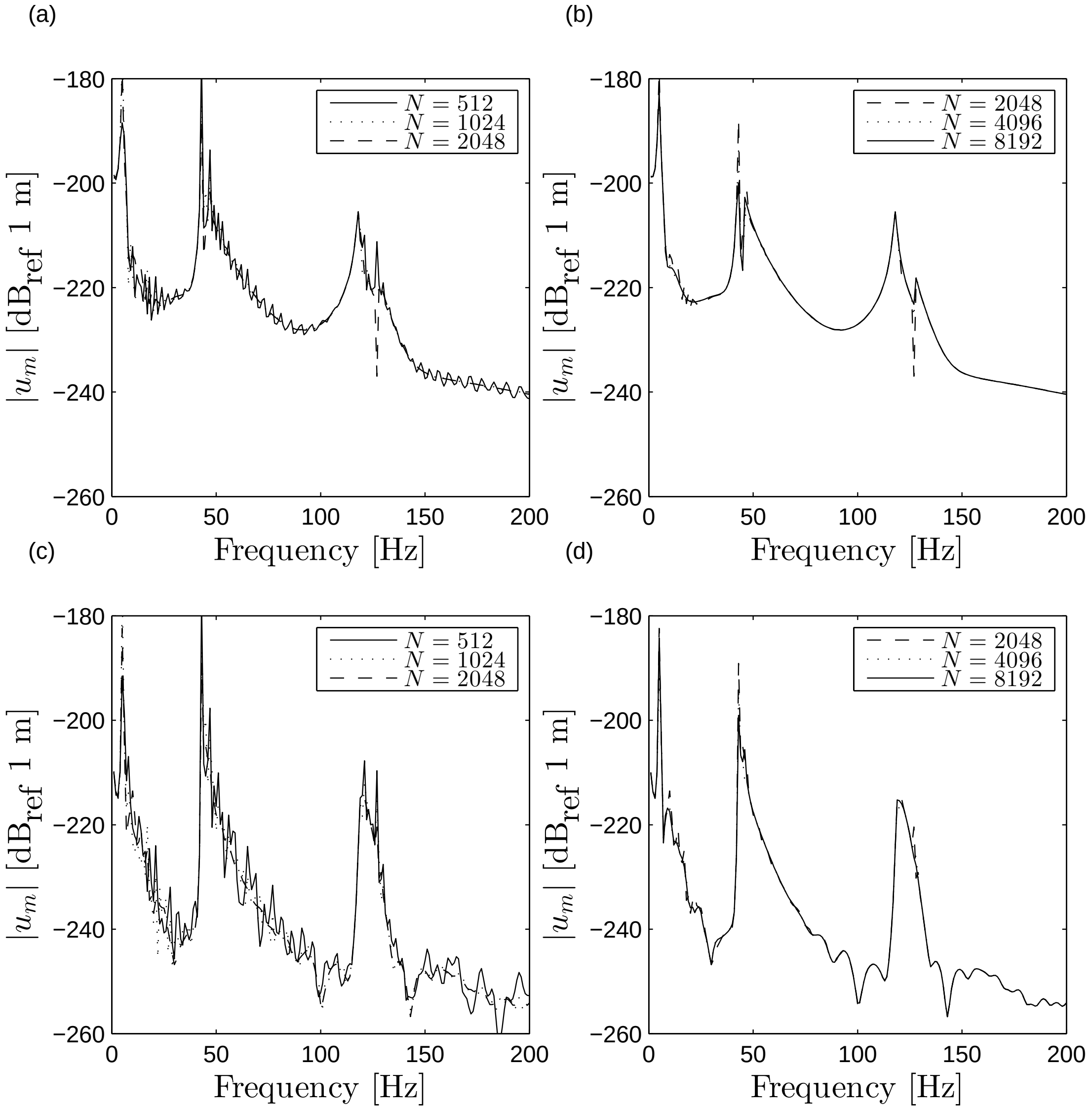

FIG. 3.10: Comparison of the maximum displacement magnitude at $r = 10$ m and $\theta = \pi/2$ rad for five different values of the total number of samples N. Two cross-sections have been considered: $x_m = 0$ m ((a) and (b)) and $x_m = 40$ m ((c) and (d)).

Ring modes

Fig. 3.11 presents the results considering four different number of total ring modes N_r = 6, 10, 15 and 20. The results are obtained considering f_t = 2400 Hz, Δx = 0.5 m and N = 8192 samples. As can be seen from (a) and (c), choosing 6 or 10 ring modes for the calculations gives errors of 10-15 dB and 2-3 dB respectively. As in the case of the truncation frequency, the errors are more significant when high excitation frequencies are studied. From (b) and (d) can be concluded that convergence of the results is achieved when at least 15 ring modes are considered. Differences smaller than

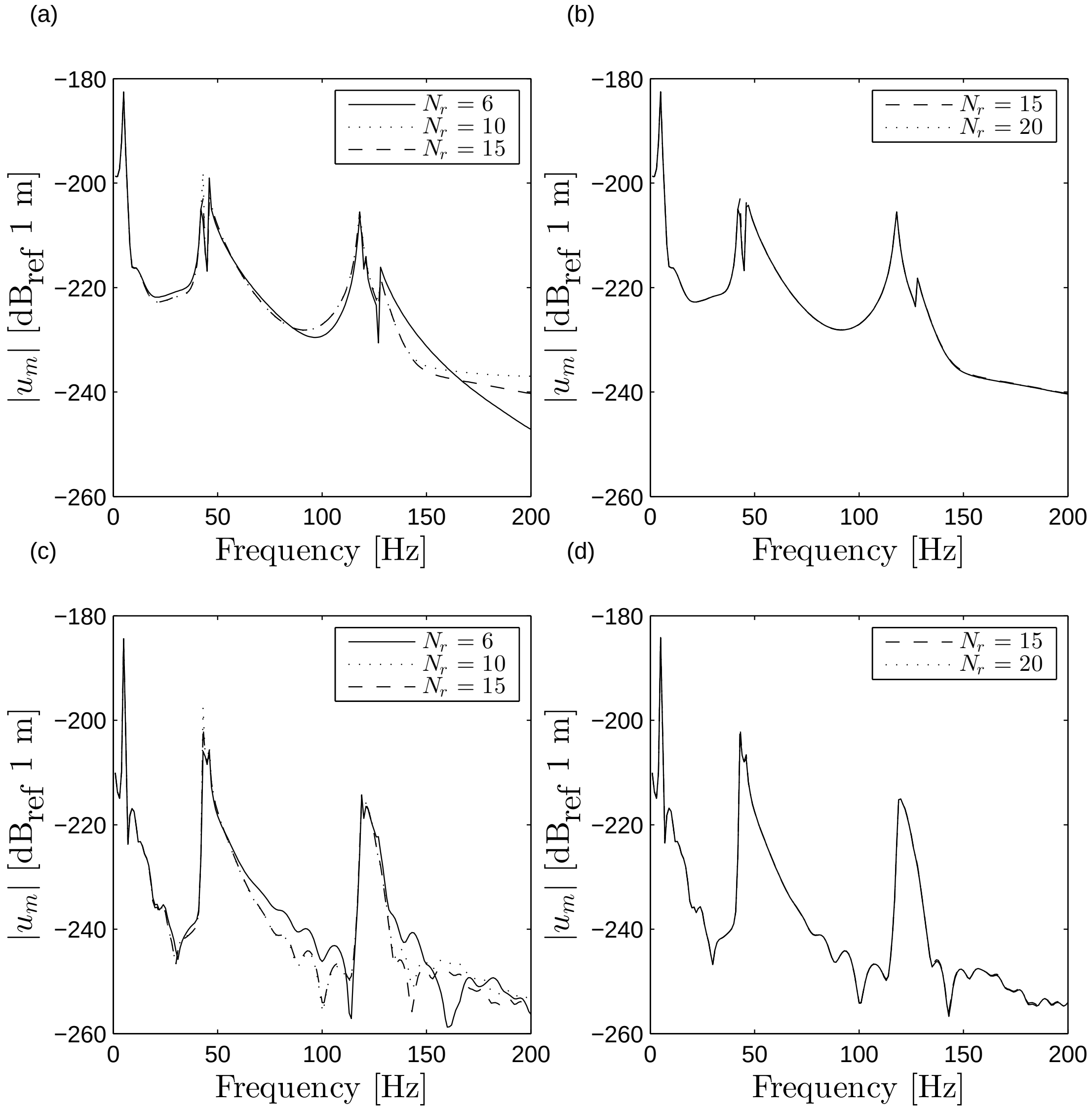

FIG. 3.11: Comparison of the maximum displacement magnitude at $r = 10$ m and $\theta = \pi/2$ rad for four different values of the total number of ring modes N_r Two cross-sections have been considered: $x_m = 0$ m ((a) and (b)) and $x_m = 40$ m ((c) and (d)).

0.1 dB are obtained if 20 ring modes are calculated instead of 15. These results are agree with the convergence criteria proposed by Forrest and Hunt [17].

3.6.3 Model results

Fig. 3.12 shows the magnitude of the left coupling load $\bar{F}_1^p$ for four different excitation frequencies: 10, 40, 80 and 160 Hz. The results have been obtained considering that a harmonic unitary vertical point load is applied at the centre of the interior floor, where $y_4 = 5.45$ m, and considering the cross-section $x = 0$ m. In this case, the

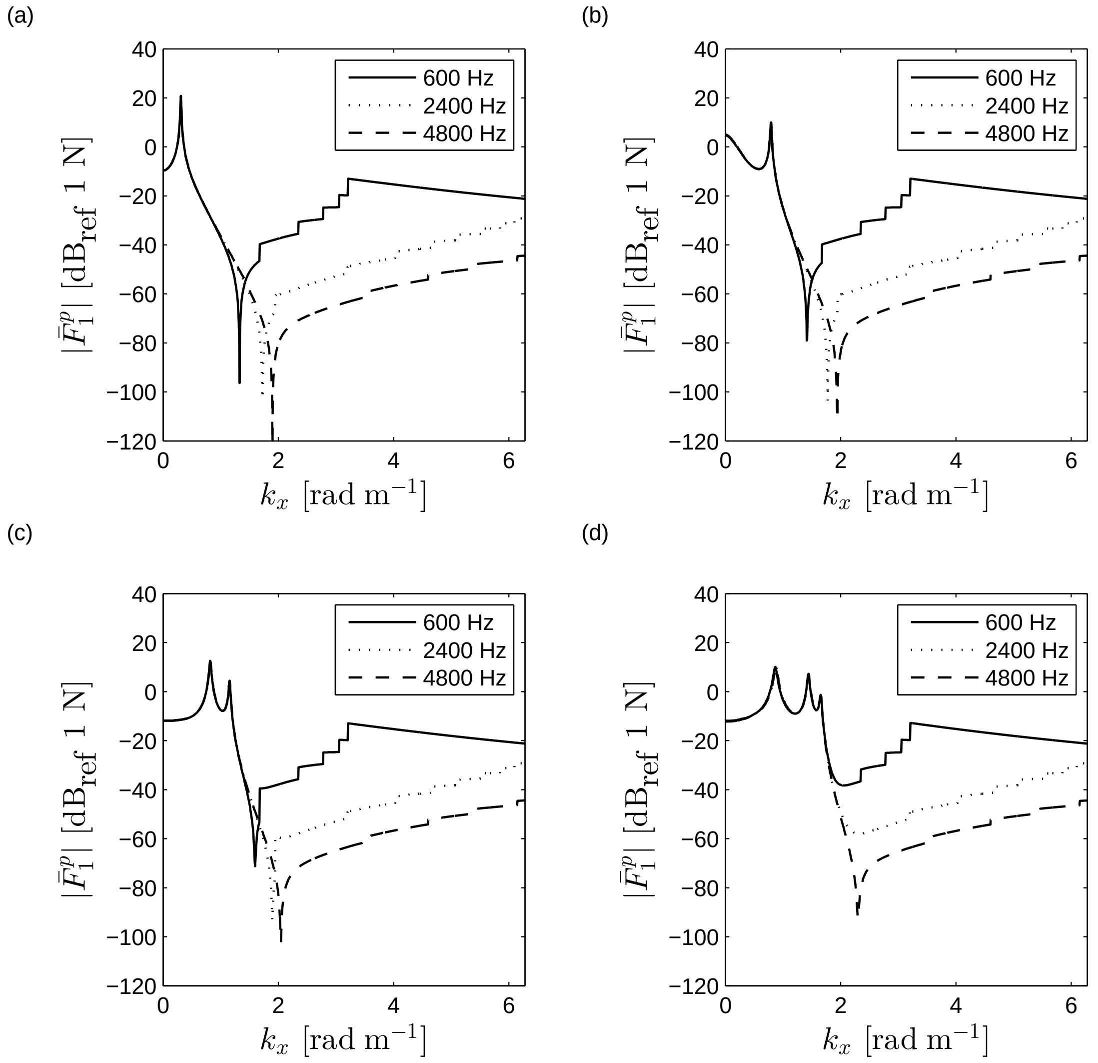

FIG. 3.12: Magnitude of the coupling load $\bar{F}_1^p$ when the strip plate is excited by a vertical harmonic point load applied at $y_4 = 5.45$ m and considering three different truncation frequencies (600, 2400 and 4800 Hz). Results are presented for different exciting frequencies: (a) 10 Hz, (b) 40 Hz, (c) 80 Hz and (d) 160 Hz.

wavenumber and space distributions of the coupling loads are symmetric with respect to the x-direction and equal for both. Calculations have been performed considering three diferent frequency truncation limits: 600, 2400 and 4800 Hz. Differences in the results are only found for high wavenumber values. When the displacement field of the double-deck tunnel is desired, this high wavenumber contribution of the coupling load is multiplied by the response of the system which, at these wavenumber values, is almost zero. Due to this, the product of both becomes negligible and the 600 Hz truncation limit ensures good accuracy of the results. Only when the space domain distribution of the coupling load is desired, the high wavenumber content plays an important role in the calculations and a higher truncation limit must be considered. The importance of choosing a high truncation limit is demonstrated in Fig. 3.13, where the coupling

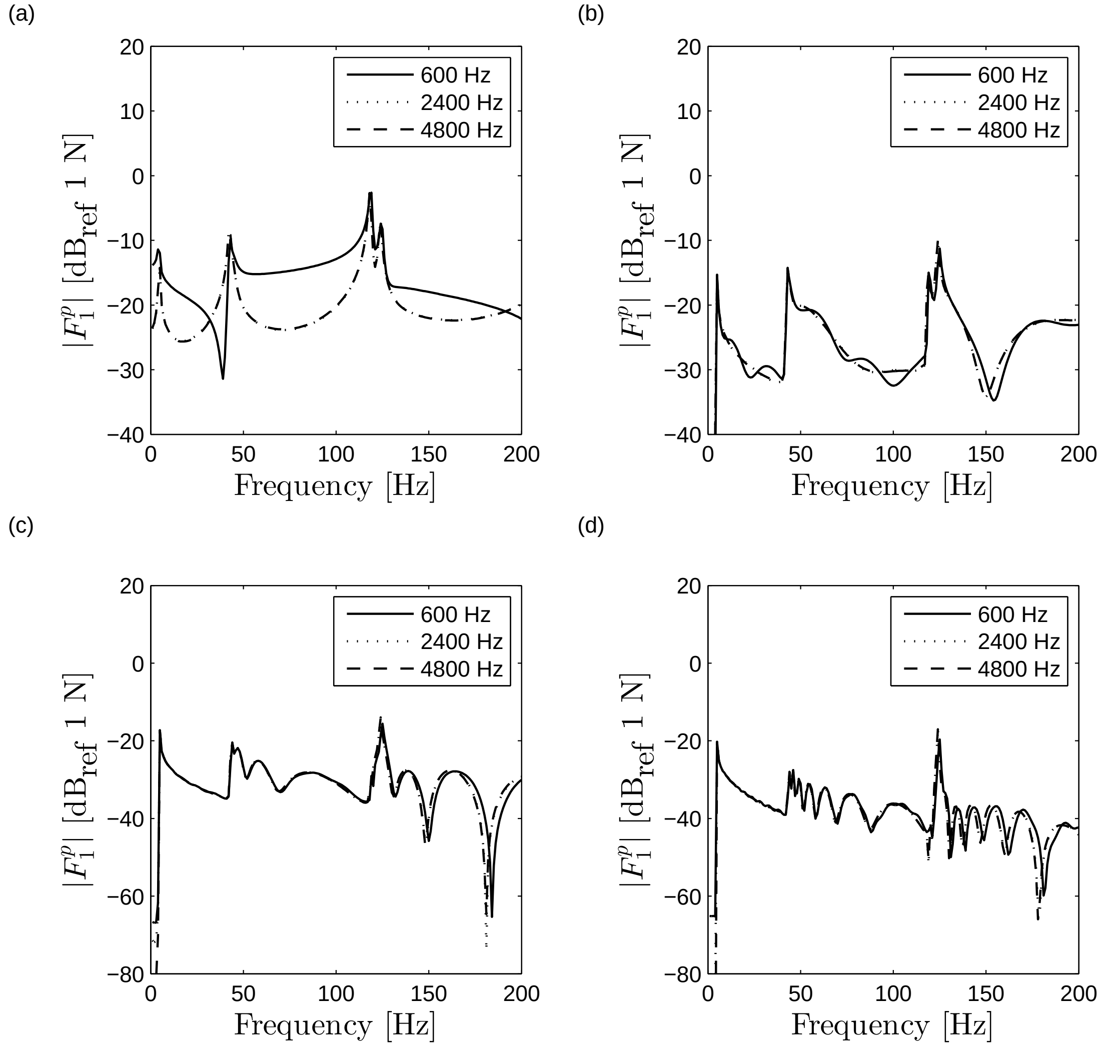

FIG. 3.13: Magnitude of the coupling load F_1^p when the strip plate is excited by a vertical harmonic point load applied at $y_4 = 5.45$ m and considering three different truncation frequencies (600, 2400 and 4800 Hz). The cross-sections considered are: (a) $x_m = 0$ m, (b) $x_m = 20$ m, (c) $x_m = 50$ m and (d) $x_m = 100$ m.

load $\bar{F}_1^p$ has been transformed to the space domain and the frequency dependance of its magnitude is plotted at four tunnel cross-sections: $x_m = 0$, 20, 50 and 100 m. It is clear that the coupling load distribution is not accurately calculated if a truncation frequency of 600 Hz is considered, especially when measuring positions near the applied loads are considered.

Fig. 3.12 also provides an additional information that is used for choosing an adequate wavenumber sampling. Since the range where the main wavenumber contribution of the coupling loads becomes wider as the excitation frequency increases, an adequate wavenumber sampling for the maximum exciting frequency case can be used for all the other exciting frequencies. The use of a unique wavenumber sampling vector enables

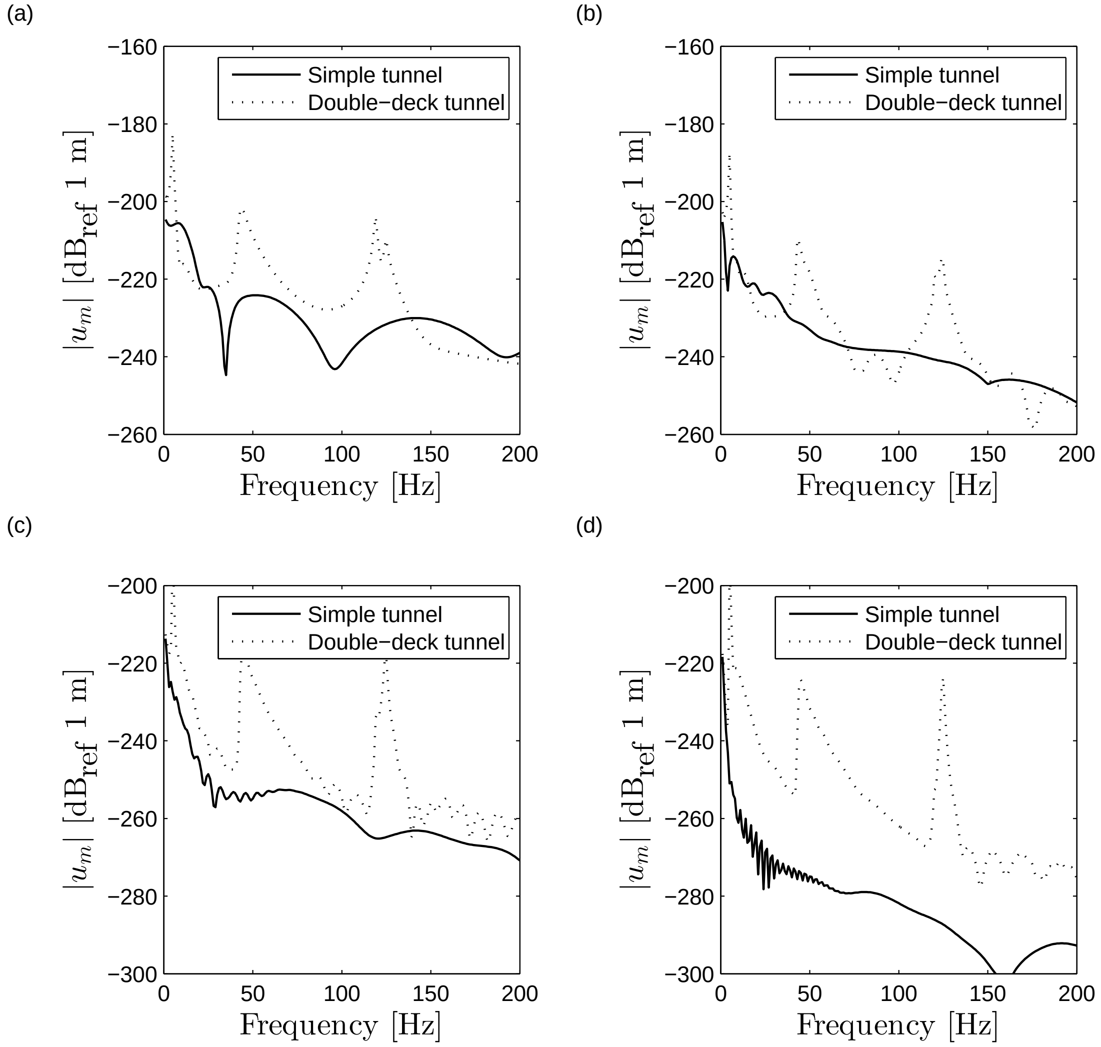

Fig. 3.14: Maximum displacement magnitude response of a double-deck tunnel and a simple tunnel. Results are calculated at $r_m = 10$ m and $\theta_m = \pi/2$. The cross-sections considered are: (a) $x_m = 0$ m, (b) $x_m = 20$ m, (c) $x_m = 50$ m and (d) $x_m = 100$ m.

a much faster computation of the results. The sampling defined with the previously specified values of N and Δk is adequate for all the excitation frequencies studied.

In Fig. 3.14 a comparison of the frequency response of the double-deck tunnel against the frequency response of a simple tunnel is presented. The double-deck tunnel is excited by a vertical unitary point load applied at $y_4 = 5.45$ m and the simple tunnel, which is modelled using the PiP tunnel model [17], is excited by a radial unitary point load applied at its bottom. The results are obtained, for the previously used set of cross-sections, at $r_3 = 10$ m and $\theta_3 = \pi/2$ rad. The comparison has been performed calculating the maximum displacement magnitude for excitation frequency values in the range 1-200 Hz with a frequency resolution $\Delta f = 1$ Hz.

The comparison shows some clear differences between the response of both types of tunnels. At the chosen positions the response of the double-deck tunnel tends to be higher than the response of the simple one for most of the considered frequencies. Also, for all of the cross-sections considered, the double-deck tunnel response shows moderately sharp peaks at certain frequencies. This type of response is not found in the simple tunnel case, therefore it must be caused by the interior floor dynamic behaviour and the interaction between it and the tunnel-soil systems. Looking at the obtained displacements at cross-sections away from the one where the load is applied, it is also seen that the decay of the double-deck tunnel response is smoother than the one obtained in the simple tunnel case.

3.6.4 Comparison with an uncoupled model

A simpler way to model the interaction between the interior floor and the tunnel-soil system is to consider a weak coupling model. In this type of coupling, the tunnel-soil system is assumed to be perfectly rigid when the interaction loads are calculated. These loads are then introduced to the tunnel-soil system to obtain its response. To justify the use of the proposed coupling hypothesis instead of the weak coupling ones, both models are compared. Under the weak coupling assumption, the interior floor is considered as an strip plate simply supported at both edges. Its response is given again by Eq. (3.36) but by considering the eigenmodes of the SS-SS case instead of the F-F ones. Finally, to obtain the weak coupling model response, the edge loads V_y of the SS-SS strip plate (Eq. (B.7)) are obtained and applied as the input loads of the PiP model.

In Fig. 3.15 the SS-SS strip plate edge load at $y_p = 0$ is compared to the antitransformed left coupling load F_1^p for two different types of ground. The first one, named soft ground, has already been defined in Table 3.3. The second one, named hard ground, is considered to have a Young modulus 100 times higher. A vertical harmonic point load applied at $y_4 = 5.45$ m is again considered and the truncation frequency is set to 4800 Hz. As can be seen in the plots, the soft ground case presents some peaks that the weak coupling model doesn't predict. In contrast, in the case of the hard ground, these peaks are not obtained and the resulting coupling loads are very similar to the ones obtained with an uncoupled model. It is concluded that the weak coupling assumption would only be an acceptable hypothesis for very a hard ground, being clearly unrealistic for the types of ground that typically surrounds tunnels.

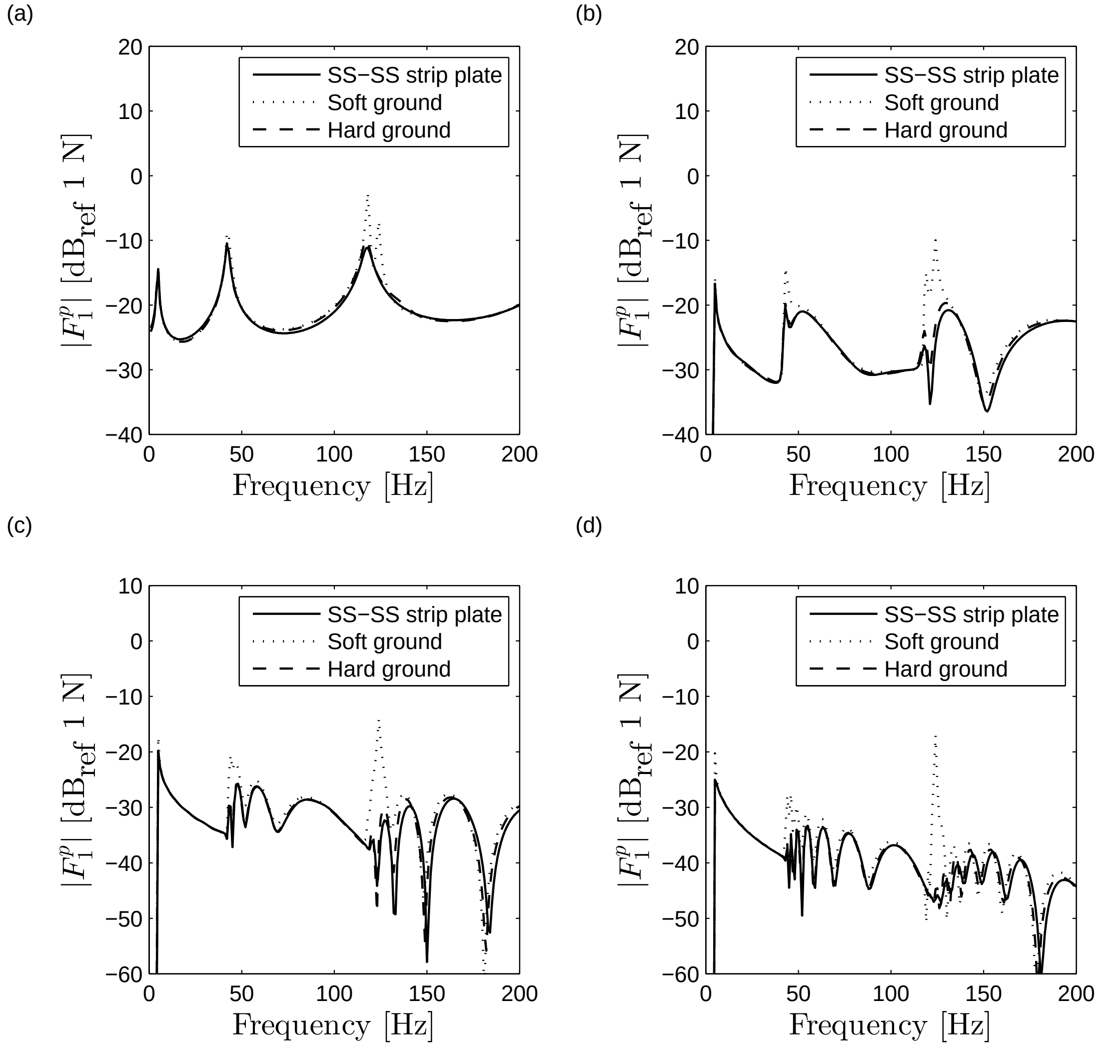

FIG. 3.15: Comparison between the coupling load F_1^p of the double-deck model for two types of ground and the edge load V_y in a SS-SS strip plate. The cross-sections considered are: (a) $x_m = 0$ m, (b) $x_m = 20$ m, (c) $x_m = 50$ m and (d) $x_m = 100$ m.

3.6.5 Effect of a tunnel bottom load

The proposed model allows to study the effect that a load applied at the bottom of the tunnel (labeled as Line 5) has on different positions of Line 4. This effect is calculated here comparing the displacements obtained at this line of the interior floor when a radial point load applied at the cross-section $x_m = 0$ is added to the previously considered vertical point load acting on the interior floor. This calculation requires adding the terms $\bar{\beta}_{1\theta,5r}\bar{F}_5^t$ and $\bar{\beta}_{2\theta,5r}\bar{F}_5^t$ in the right part of Eq. (3.66). The new system of equations is

$$\begin{pmatrix} -(\bar{\alpha}_{11}+\bar{\beta}_{1\theta,1\theta}) & -\bar{\alpha}_{12}+\bar{\beta}_{1\theta,2\theta} \\ -\bar{\alpha}_{21}+\bar{\beta}_{2\theta,1\theta} & -(\bar{\alpha}_{22}+\bar{\beta}_{2\theta,2\theta}) \end{pmatrix} \begin{pmatrix} \bar{F}_1^t \\ \bar{F}_2^t \end{pmatrix} = \begin{pmatrix} \bar{\alpha}_{14} \\ \bar{\alpha}_{24} \end{pmatrix} \bar{F}_4^p + \begin{pmatrix} \beta_{1\theta,5r} \\ -\beta_{2\theta,5r} \end{pmatrix} \bar{F}_5^t. \tag{3.83}$$

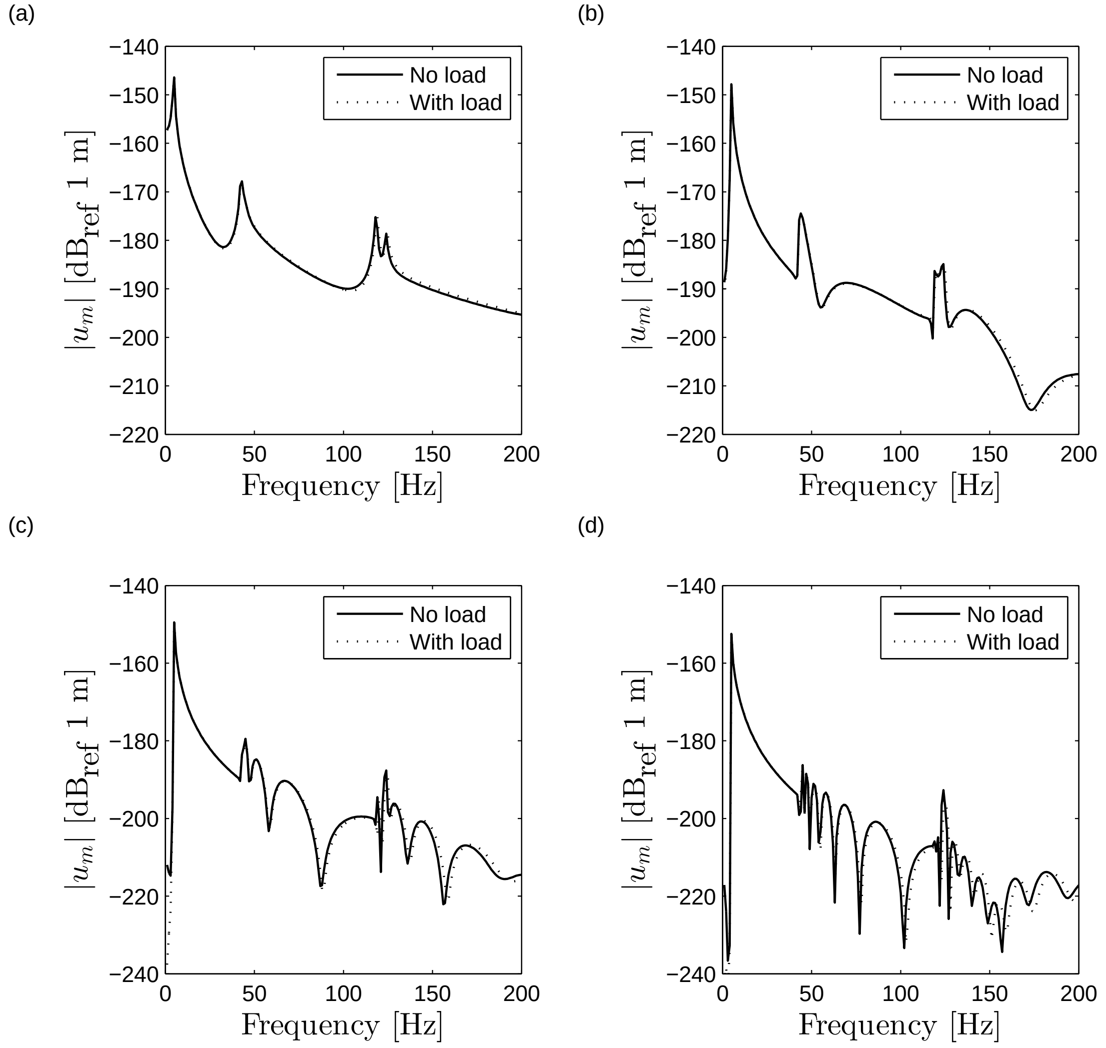

FIG. 3.16: Displacement magnitude at $y_p = 5.45$ m when a radial point load applied at the bottom of the tunnel is added to the initial loading configuration and also when it is not. The cross-sections considered are: (a) $x_m = 0$ m, (b) $x_m = 20$ m, (c) $x_m = 50$ m and (d) $x_m = 100$ m.

In the chosen system of coordinates the radial point load is applied at $\theta_5 = 3\pi/2$. Again, at the plate edges, only antisymmetric terms are once again used and the receptances can be written as

$$\begin{aligned}\bar{\beta}_{1\theta,5r} &= \frac{1}{r_t\pi}\sum_{n=1}^{\infty} m_{23,n}\sin\left(\frac{3\pi n}{2}\right),\\ \bar{\beta}_{2\theta,5r} &= \frac{1}{r_t\pi}\sum_{n=1}^{\infty}(-1)^n m_{23,n}\sin\left(\frac{3\pi n}{2}\right).\end{aligned}$$

Fig. 3.16 compares the resulting displacements at $y_4 = 5.45$ m for the four previously considered cross-sections. The results show that the effect of the radial bottom load can almost be ignored in all the frequency range considered. This load effect should only be taken into account for the farthest measuring points and at high frequencies.

3.7 Chapter conclusions

A three-dimensional model for the dynamic behaviour of double-deck tunnels is presented. The use of the receptance method allows to calculate the response of the global structure by combining the responses of the interior floor and of the tunnel-soil system separately. The interior floor is assumed to behave as a thin strip plate while the tunnel-soil system is modelled using the PiP model. The obtained model can be used to extend the prediction of vibration levels generated by underground trains to this new type of tunnel infrastructure. The details of the numerical computation of the model are also described. The results presented show the importance of the interior floor behaviour on the resulting displacements. A comparison is made between the vibration levels of a double-deck tunnel and those found in a simple tunnel, finding significant differences between their responses. In order to justify the use of a strong coupled model, the resulting interaction loads are compared to those obtained in a weak coupled model. Except for the case of unrealistically rigid grounds, the coupling assumptions considered in the proposed model are found to be necessary. Finally, the effect that the application of a second load at the bottom of the tunnel has on the interior floor deflection is also studied. It is found that this load effect only becomes important at long distances from the points where both loads are applied.

Chapter 4

A power flow calculation in plane-strain conditions

The purpose of the present chapter is to present a calculation of the mean power flow radiated by a double-deck circular tunnel and compare it to the one radiated by a simple circular tunnel. The comparison is performed considering that a harmonic line load is applied on both tunnels. Plane-strain conditions can be assumed for both tunnel models, simplifying the analytical formulation of the problem and improving the efficiency of the calculations. Numerical results show significant differences between the power flow radiated by both tunnels, with the one radiated by the double-deck tunnel reaching much higher values. The effect of changing the position of the applied load on the interior floor and of modifying its flexural rigidity is also studied. A comparison is made between the radiation patterns of both tunnels for the most important one-third octave bands in human exposure to building vibrations caused by underground trains [76].

4.1 Analytical formulation of the model in plane-strain conditions

In this chapter, the power flor radiated by a double-deck tunnel is compared to the one radiated by a simple tunnel. This comparison is performed considering that both structures are excited by a harmonic line load. This type of load is not adequate to calculate accurate values of the ground-borne vibration caused by a train passage but it is an interesting choice when a power flow comparison between two types of tunnel structures is desired. When harmonic line loads are considered, plain strain conditions

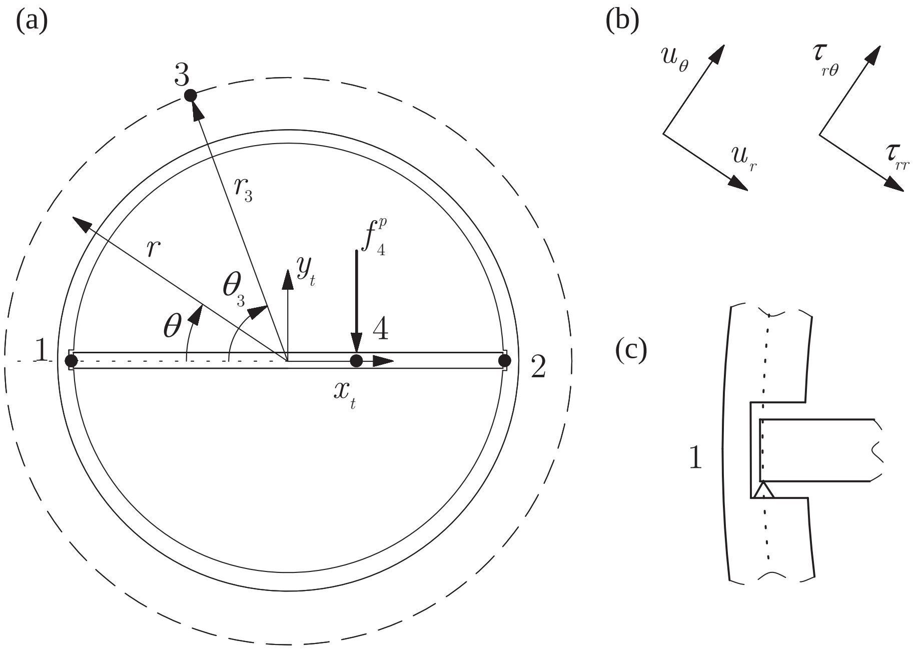

Fig. 4.1: (a) Cross-section of a double-deck circular tunnel. A Cartesian and a cylindrical system of coordinates are defined. (b) Positive signs for the displacements and stresses. (c) Coupling condition considered between the tunnel and the interior floor.

can be assumed and the problem is solved using only a cross-section of the tunnel-soil system. Fig. 4.1 presents this cross-section for a double-deck tunnel. The figure also shows the chosen positive direction for the displacements $\mathbf{u}$ and stresses $\boldsymbol{\tau}$ and the coupling condition considered between the tunnel and the interior floor. A cylindrical system of coordinates (θ, r) is defined to describe any point of soil or the tunnel. A Cartesian system of coordinates (x_t, y_t) is also defined to describe the mean local power flow distributions presented in Section 4.3.

As in the previous chapter, the interior floor is coupled to the tunnel structure at Lines 1 and 2 and the external load, which in this case is a vertical harmonic line load f_4^p, is applied at Line 4. The response of the structure is obtained at an arbitrary Line 3 of the soil. The problem is again solved coupling the interior floor to the tunnel-soil structure by means of the receptance method. The next subsections describe the dynamic equations of each subsystem in plane-strain conditions.

4.1.1 Thin-plate in plane-strain conditions

Fig. 4.2 presents a cross-section of the interior floor with its thickness h_p and width L_p defined. A Cartesian system of coordinates (y_p, z_p) is defined and the deflection of any line of the interior floor is described by w_p.

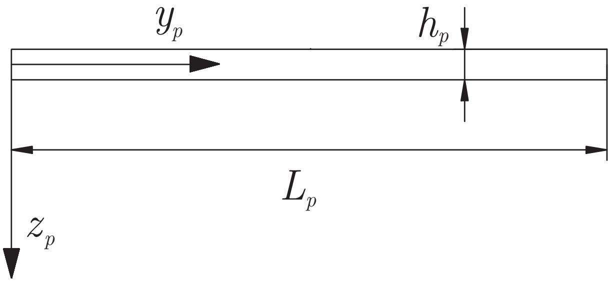

FIG. 4.2: Interior floor model in plane-strain conditions

The equation of motion of a thin plate in plane-strain conditions is obtained imposing that $\dfrac{\partial}{\partial x} = 0$ in Eq. (3.3), which gives

$$D_p \frac{\partial^4 w_p(y_p,t)}{\partial y_p^4} + \rho_p h_p \frac{\partial^2 w_p(y_p,t)}{\partial t^2} = f_4^p(y_p,t), \tag{4.1}$$

where

$$D_p = \frac{E_p h_p^3}{12(1-\nu_p^2)} \tag{4.2}$$

is the flexural rigidity of the plate, ρ_p is its density, E_p is its Young modulus and ν_p is its Poisson ratio. The obtained equation is equivalent to the equation of motion of a Bernoulli-Euler beam [103].

The vertical harmonic line load can be written as

$$f_4^p(y,t) = \delta(y_p - y_4)\mathrm{e}^{\mathrm{i}\omega t}. \tag{4.3}$$

Because harmonic motion is assumed

$$w_p(y_p,t) = W_p(y_p)\mathrm{e}^{\mathrm{i}\omega t}. \tag{4.4}$$

Introducing Eqs. (4.4) and (4.3) into Eq. (4.1) the following equation is obtained

$$\frac{\mathrm{d}^4 W_p}{\mathrm{d}y_p^4} - \kappa^4 W_p = \frac{\delta(y_p - y_4)}{D_p}, \tag{4.5}$$

where κ has been defined in Eq. (3.8).

Again, the receptance method requires to know the forced response of the system considering free boundary conditions. Now, the boundary conditions of a free edge of the plate are

$$\left.\frac{\mathrm{d}^2 W_p}{\mathrm{d}y_p^2}\right|_{y_p=0,L_p} = 0, \qquad \left.\frac{\mathrm{d}^3 W_p}{\mathrm{d}y_p^3}\right|_{y_p=0,L_p} = 0 \tag{4.6}$$

and the resulting characteristic equation is

$$\cosh(\kappa_n L_p)\cos(\kappa_n L_p) - 1 = 0, \tag{4.7}$$

where κ_n has been defined in Eq. (3.27).

In this case is not necessary to perform analytical approximations to obtain numerically well-behaved eigenfunctions. Very accurate results can be obtained if the eigenfunctions are rewritten as Tang [105] proposes. For the F-F case, this expression is

$$\begin{aligned} W_n(y_p) \;=\; & \left(\frac{1}{\sin(\kappa_n L_p) - \sinh(\kappa_n L_p)}\right) \cdot \\ & [\cosh(\kappa_n L_p)\sinh(\kappa_n y_p) - \cosh(\kappa_n y_p)\sinh(\kappa_n L_p) \\ & -\cos(\kappa_n y_p)\sinh(\kappa_n L_p) - \cos(\kappa_n L_p)\sinh(\kappa_n y_p) \\ & +\cosh(\kappa_n y_p)\sin(\kappa_n L_p) + \cosh(\kappa_n L_p)\sin(\kappa_n y_p) \\ & +\cos(\kappa_n y_p)\sin(\kappa_n L_p) - \cos(\kappa_n L_p)\sin(\kappa_n y_p)]. \end{aligned} \tag{4.8}$$

The modal participation method is again used to obtain the forced response of the interior floor. The deflection is now written as

$$W_p(y_p) = \sum_{n=1}^{\infty} \frac{W_n(y_p) p_n}{D_p(\kappa_n^4 - \kappa^4)}, \tag{4.9}$$

where

$$p_n = \frac{1}{C_n}\int_0^{L_p} \delta(y_p - y_4) W_n(y_p) \mathrm{d}y_p = \frac{W_n(y_4)}{C_n} \tag{4.10}$$

and where

$$C_n = \int_0^{L_p} W_n(y_p)^2 \mathrm{d}y_p. \tag{4.11}$$

The obtained expressions are almost equal to those obtained in the global model but, in this case, the results are directly written in the space domain. It is also worth to mention that the summation of modes must include the two rigid body modes existing at $\omega_n = 0$ (degenerate modes). Those modes only appeared in the 3D model when the results for $k_x = 0$ were obtained.

In plane-strain conditions, the receptances α_{ij} are defined as the response at Line i to a harmonic line load applied at Line j. Considering again hysteretic damping, the receptance α_{i4} can be written as

$$W_p(y_i) = \alpha_{i4} = \sum_{n=1}^{\infty} W_n(y_i) W_n(y_4) B_n, \tag{4.12}$$

where

$$B_n = \frac{\mathrm{e}^{-\mathrm{i}\phi_n}}{C_n \rho_p h_p \sqrt{(\omega_n^2 - \omega^2)^2 + \omega_n^4 \eta_p^2}} \tag{4.13}$$

and where ϕ_n has been defined in Eq. (3.32).

4.1.2 PiP model in plane-strain conditions

Along this chapter, the PiP model is used for two reasons: To obtain the soil response to the interior floor-tunnel coupling loads of a double-deck tunnel and to obtain the soil response to a load applied at a simple tunnel. The only difference between both cases is the chosen origin of the angular coordinate. This difference is pointed out in Fig. 4.3, where a new angular coordinate θ' has been defined. This definition is the one proposed in [17] and simplifies the calculation of the PiP response to a radial load applied at the bottom of the tunnel. The same positive direction for the displacement and stress fields have been defined.

As in the interior floor case, the receptance of the PiP model $\boldsymbol{\beta}_{ij}$ is defined as the responses at Line i of the system to a load applied at Line j. In plane-strain conditions these receptances are 2×2 matrices that can be written as

$$\boldsymbol{\beta}_{i,j} = \begin{pmatrix} \beta_{i\theta,j\theta} & \beta_{i\theta,jr} \\ \beta_{ir,j\theta} & \beta_{ir,jr} \end{pmatrix}, \tag{4.14}$$

where the subscript definition is the same that has been used in Chapter 3.

An analogous frequency response function $\boldsymbol{\varepsilon}_{i,j}$, representing the stress caused at Line i by an line load applied at Line j is defined. These function can be also written as

$$\boldsymbol{\varepsilon}_{i,j} = \begin{pmatrix} \varepsilon_{ir\theta,j\theta} & \varepsilon_{ir\theta,jr} \\ \varepsilon_{irr,j\theta} & \varepsilon_{irr,jr} \end{pmatrix}. \tag{4.15}$$

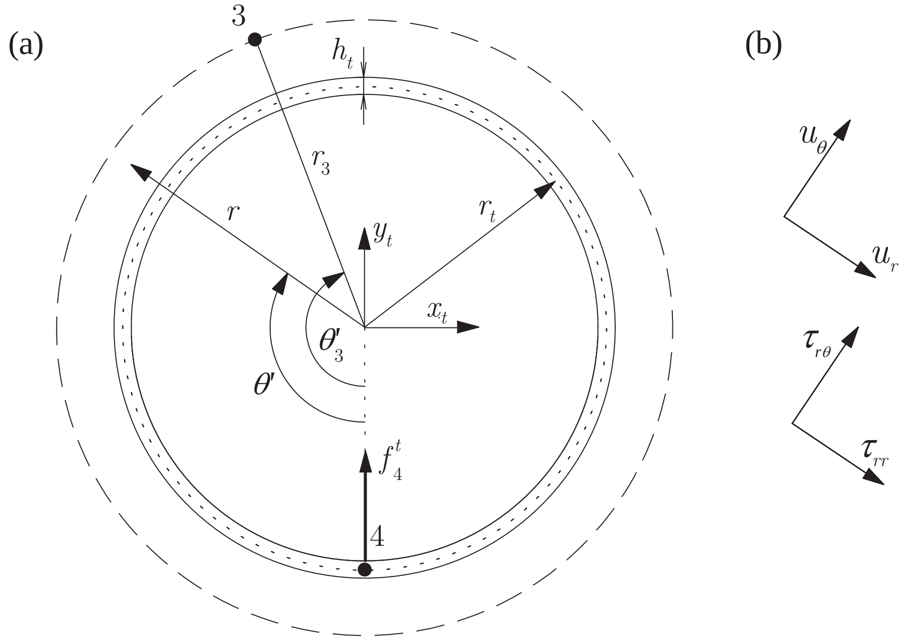

FIG. 4.3: (a) Cross-section of a simple circular tunnel with a load applied at its bottom. A Cartesian and a cylindrical system of coordinates are defined. (b) Positive signs for the displacements and stresses.

To obtain the response of a simple tunnel to a radial load applied at $\theta' = 0$ only the symmetric formulation of the PiP model is required. In this case, Eqs. (D.48) become

$$\begin{aligned} \mathbf{u} &= \mathbf{U}\mathrm{e}^{\mathrm{i}\omega t} = \sum_{n=0}^{\infty} \mathbf{S}_{2\mathrm{D}}^{s} \mathbf{U}_n^s \mathrm{e}^{\mathrm{i}\omega t}, \\ \boldsymbol{\tau} &= \mathbf{T}\mathrm{e}^{\mathrm{i}\omega t} = \sum_{n=0}^{\infty} \mathbf{S}_{2\mathrm{D}}^{s} \mathbf{T}_n^s \mathrm{e}^{\mathrm{i}\omega t}, \end{aligned} \tag{4.16}$$

where $\mathbf{S}_{2\mathrm{D}}^{s}$ is defined in Eq. (D.49) and where $\mathbf{U}_n^s$ and $\mathbf{T}_n^s$ are obtained from Eq. (D.50).

The tangential and radial load coefficients of the considered load are given by

$$F_{4\theta,n}^{t,s} = 0, \qquad F_{4r,n}^{t,s} = \begin{cases} \dfrac{1}{2\pi r_t}, & n = 0, \\ \dfrac{1}{\pi r_t}, & n > 0. \end{cases} \tag{4.17}$$

Combining Eqs. (4.16) and (4.17), the displacement and stress fields of Line 3 caused by a radial load applied at Line 4 can be written as

$$\mathbf{u} = \boldsymbol{\beta}_{3,4r}\mathrm{e}^{\mathrm{i}\omega t}, \qquad \boldsymbol{\tau} = \boldsymbol{\varepsilon}_{3,4r}\mathrm{e}^{\mathrm{i}\omega t}, \tag{4.18}$$

where

$$\boldsymbol{\beta}_{3,4r} = \begin{pmatrix} \beta_{3\theta,4r} \\ \beta_{3r,4r} \end{pmatrix} = \frac{1}{2r_t\pi} \begin{pmatrix} 0 \\ m^s_{22,0} \end{pmatrix} + \frac{1}{r_t\pi} \sum_{n=1}^{\infty} \begin{pmatrix} m^s_{12,n} \sin(n\theta'_3) \\ m^s_{22,n} \cos(n\theta'_3) \end{pmatrix} \tag{4.19}$$

and

$$\boldsymbol{\varepsilon}_{3,4r} = \begin{pmatrix} \varepsilon_{3r\theta,4r} \\ \varepsilon_{3rr,4r} \end{pmatrix} = \frac{1}{2r_t\pi} \begin{pmatrix} 0 \\ k^s_{22,0} \end{pmatrix} + \frac{1}{r_t\pi} \sum_{n=1}^{\infty} \begin{pmatrix} k^s_{12,n} \sin(n\theta'_3) \\ k^s_{22,n} \cos(n\theta'_3) \end{pmatrix}. \tag{4.20}$$

When the response of a double-deck tunnel to tangential loads applied at $\theta_1 = 0$ and $\theta_2 = \pi$ is calculated, only the antisymmetric formulation formulation of the PiP model is required. In this case, Eq. (D.48) becomes

$$\begin{aligned} \mathbf{u} &= \mathbf{U}\mathrm{e}^{\mathrm{i}\omega t} = \sum_{n=0}^{\infty} \mathbf{S}^a_{2\mathrm{D}} \mathbf{U}^a_n \mathrm{e}^{\mathrm{i}\omega t}, \\ \boldsymbol{\tau} &= \mathbf{T}\mathrm{e}^{\mathrm{i}\omega t} = \sum_{n=0}^{\infty} \mathbf{S}^a_{2\mathrm{D}} \mathbf{T}^a_n \mathrm{e}^{\mathrm{i}\omega t}. \end{aligned} \tag{4.21}$$

The load coefficients for Line 1 are given by

$$F^{t,a}_{1r,n} = 0, \qquad F^{t,a}_{1\theta,n} = \begin{cases} \dfrac{1}{2\pi r_t}, & n = 0, \\ \dfrac{1}{\pi r_t}, & n > 0, \end{cases} \tag{4.22}$$

while the load coefficients for Line 2 are

$$F^{t,a}_{2r,n} = 0, \qquad F^{t,a}_{2\theta,n} = \begin{cases} \dfrac{1}{2\pi r_t}, & n = 0, \\ \dfrac{(-1)^n}{\pi r_t}, & n > 0. \end{cases} \tag{4.23}$$

The displacement and stress fields of the double-deck tunnel are detailed in the next subsection.

4.1.3 Coupling both systems

As was mentioned in Chapter 3, the interaction between the tunnel walls and the interior floor of a double-deck tunnel depends on the construction method used to build it. When the interior floor is a separate precast slab structure supported on the tunnel walls simply supported connections at both edges of the interior floor are considered (see Fig. 4.1). Omitting the terms $\mathrm{e}^{\mathrm{i}\omega t}$, the coupling conditions of the plain-strain case can be expressed as

$$\begin{array}{rclrcl} W_p(0) & = & -U_\theta(r_t,0), & W_p(L_p) & = & U_\theta(r_t,\pi), \\ F_1^p & = & -F_{1\theta}^t, & F_2^p & = & -F_{2\theta}^t. \end{array} \tag{4.24}$$

The related deflections and displacements can be written in terms of the subsystems receptances as

$$\begin{array}{rcl} W_p(0) & = & -\alpha_{11}F_1^p - \alpha_{12}F_2^p + \alpha_{14}F_4^p, \\ W_p(L_p) & = & -\alpha_{21}F_1^p - \alpha_{22}F_2^p + \alpha_{24}F_4^p, \\ U_\theta(r_t,0) & = & \beta_{1\theta,1\theta}F_{1\theta}^t - \beta_{1\theta,2\theta}F_{2\theta}^t, \\ U_\theta(r_t,\pi) & = & \beta_{2\theta,1\theta}F_{1\theta}^t - \beta_{2\theta,2\theta}F_{2\theta}^t, \end{array} \tag{4.25}$$

where the signs are defined by the positive directions defined in each subsystem.

The coupling loads are obtained inserting Eq. (4.25) into Eq. (4.24). The system of equations obtained is

$$\begin{pmatrix} -(\beta_{1\theta,1\theta}+\alpha_{11}) & -\alpha_{12}+\beta_{1\theta,2\theta} \\ -\alpha_{21}+\beta_{2\theta,1\theta} & -(\alpha_{22}+\beta_{2\theta,2\theta}) \end{pmatrix} \begin{pmatrix} F_{1\theta}^t \\ F_{2\theta}^t \end{pmatrix} = \begin{pmatrix} \alpha_{14} \\ \alpha_{24} \end{pmatrix} F_4^p. \tag{4.26}$$

The required plate receptances, calculated using Eq. (4.12), are

$$\begin{array}{rclrcl} \alpha_{14} & = & \sum_{n=1}^{\infty} W_n(0)W_n(y_4)B_n, & \alpha_{24} & = & \sum_{n=1}^{\infty} W_n(y_4)W_n(L_p)B_n, \\ \alpha_{11} & = & \sum_{n=1}^{\infty} W_n(0)^2 B_n, & \alpha_{12} & = & \sum_{n=1}^{\infty} W_n(0)W_n(L_p)B_n. \end{array} \tag{4.27}$$

Some considerations can be used to avoid unnecessary calculations. First, because the plate eigenmodes are symmetric or antisymmetric, $\alpha_{11} = \alpha_{22}$. Second, due to the Maxwell reciprocity principle, $\alpha_{12} = \alpha_{21}$. And finally, if $y_4 = L_p/2$, only symmetric modes are excited and $\alpha_{14} = \alpha_{24}$.

For the PiP model, the required receptances are obtained substituting Eqs. (4.22) and (4.23) into the tangential component of Eq. (4.16), obtaining

$$\begin{array}{rcl} \beta_{1\theta,1\theta} & = & \beta_{2\theta,2\theta} = \frac{1}{2r_t\pi}m_{11,0}^a + \frac{1}{r_t\pi}\sum_{n=1}^{\infty} m_{11,n}^a, \\ \beta_{1\theta,2\theta} & = & \beta_{2\theta,1\theta} = \frac{1}{2r_t\pi}m_{11,0}^a + \frac{1}{r_t\pi}\sum_{n=1}^{\infty} m_{11,n}^a(-1)^n. \end{array} \tag{4.28}$$

Once the coupling forces are determined, the displacement and stress fields at Line 3 can be written as

$$\mathbf{u} \;=\; \boldsymbol{\gamma}_{3,4z}\mathrm{e}^{\mathrm{i}\omega t}, \quad \boldsymbol{\tau} \;=\; \boldsymbol{\varsigma}_{3,4z}\mathrm{e}^{\mathrm{i}\omega t}, \tag{4.29}$$

where $\boldsymbol{\gamma}_{3,4z}$ is the double-deck tunnel receptance at Line 3 when a load is applied at Line 4 and $\boldsymbol{\varsigma}_{3,4z}$ is the corresponding stress frequency response function. These functions are given by

$$\boldsymbol{\gamma}_{3,4z} = \begin{pmatrix} \gamma_{3\theta,4z} \\ \gamma_{3r,4z} \end{pmatrix} \mathrm{e}^{\mathrm{i}\omega t} = \left[\begin{pmatrix} \beta_{3\theta,1\theta} \\ \beta_{3r,1\theta} \end{pmatrix} F^t_{1\theta} - \begin{pmatrix} \beta_{3\theta,2\theta} \\ \beta_{3r,2\theta} \end{pmatrix} F^t4_{2\theta} \right] \mathrm{e}^{\mathrm{i}\omega t} \tag{4.30}$$

and

$$\boldsymbol{\varsigma}_{3,4z} = \begin{pmatrix} \varsigma_{3r\theta,4z} \\ \varsigma_{3rr,4z} \end{pmatrix} \mathrm{e}^{\mathrm{i}\omega t} = \left[\begin{pmatrix} \varepsilon_{3r\theta,1\theta} \\ \varepsilon_{3rr,1\theta} \end{pmatrix} F^t_{1\theta} - \begin{pmatrix} \varepsilon_{3r\theta,2\theta} \\ \varepsilon_{3rr,2\theta} \end{pmatrix} F^t_{2\theta} \right] \mathrm{e}^{\mathrm{i}\omega t}. \tag{4.31}$$

4.2 Power flow calculations

The mean local power flow P at a certain point of the soil is defined as [89]

$$P = \frac{1}{T_0} \int_0^{T_0} \{\mathrm{Re}[v_r(t)]\mathrm{Re}[\tau_{rr}(t)] + \mathrm{Re}[v_\theta(t)]\mathrm{Re}[\tau_{r\theta}(t)]\}\mathrm{d}t, \tag{4.32}$$

where T_0 is the integration time and where plane strain conditions have been assumed again. The radial and tangential velocities of the considered point, $v_r(t)$ and $v_\theta(t)$, are obtained differentiating the first of Eq. (D.48):

$$\mathbf{v} = \begin{pmatrix} v_\theta \\ v_r \end{pmatrix} = \mathrm{i}\omega \begin{pmatrix} U_\theta \\ U_r \end{pmatrix} \mathrm{e}^{\mathrm{i}\omega t}. \tag{4.33}$$

Substituting the second one of Eq. (D.48) and Eq. (4.33) into Eq. (4.32) and separating the power flow into a radial component P_r and a tangential component P_θ, Eq. (4.32) can be written as

$$\begin{aligned} P \;&=\; P_\theta + P_r = \\ &\frac{1}{T_0} \int_0^{T_0} \left\{ \mathrm{Re}\left[\mathrm{i}\omega U_\theta \mathrm{e}^{\mathrm{i}\omega t}\right] \mathrm{Re}\left[T_\theta \mathrm{e}^{\mathrm{i}\omega t}\right] + \mathrm{Re}\left[\mathrm{i}\omega U_r \mathrm{e}^{\mathrm{i}\omega t}\right] \mathrm{Re}\left[T_r \mathrm{e}^{\mathrm{i}\omega t}\right] \right\} \mathrm{d}t. \end{aligned} \tag{4.34}$$

For the double-deck tunnel, using Eqs. (4.30) and (4.31), the previous equation can be split into

$$\begin{aligned} P_r &= \frac{1}{T_0}\int_0^{T_0} \mathrm{Re}[\mathrm{i}\omega\gamma_{3r,4z}\mathrm{e}^{\mathrm{i}\omega t}]\mathrm{Re}[\varsigma_{3rr,4z}\mathrm{e}^{\mathrm{i}\omega t}]\mathrm{d}t, \\ P_\theta &= \frac{1}{T_0}\int_0^{T_0} \mathrm{Re}[\mathrm{i}\omega\gamma_{3\theta,4z}\mathrm{e}^{\mathrm{i}\omega t}]\mathrm{Re}[\varsigma_{3r\theta,4z}\mathrm{e}^{\mathrm{i}\omega t}]\mathrm{d}t. \end{aligned} \tag{4.35}$$

Operating, Eq. (4.35) reduces to

$$\begin{aligned} P_r = & -\frac{\omega}{T_0(2\pi)^2}\int_0^{T_0}\{\mathrm{Im}\left[\gamma_{3r,4z}\right]\mathrm{Re}\left[\varsigma_{3rr,4z}\right]\cos^2(\omega t) \\ & -\mathrm{Im}\left[\varsigma_{3rr,4z}\right]\mathrm{Re}\left[\gamma_{3r,4z}\right]\sin^2(\omega t) \\ & +\Big(\mathrm{Re}\left[\gamma_{3r,4z}\right]\mathrm{Re}\left[\varsigma_{3rr,4z}\right]-\mathrm{Im}\left[\gamma_{3r,4z}\right]\mathrm{Im}\left[\varsigma_{3rr,4z}\right]\Big)\sin(\omega t)\cos(\omega t)\}\mathrm{d}t \end{aligned} \tag{4.36}$$

and an equivalent expression for P_θ. If the integration time is chosen to be a positive integer number of times n the period of the harmonic load, then

$$T_0 = nT = \frac{2\pi n}{\omega}, \quad n > 0$$

and, integrating Eq. (4.36) for both components of the power flow and adding them, the following result is obtained

$$\begin{aligned} P = & \frac{\omega}{2}\{\mathrm{Re}[\gamma_{3\theta,4z}]\mathrm{Im}[\varsigma_{3r\theta,4z}]-\mathrm{Im}[\gamma_{3\theta,4z}]\mathrm{Re}[\varsigma_{3r\theta,4z}] \\ & +\mathrm{Re}[\gamma_{3r,4z}]\mathrm{Im}[\varsigma_{3rr,4z}]-\mathrm{Im}[\gamma_{3r,4z}]\mathrm{Re}[\varsigma_{3rr,4z}]\}. \end{aligned} \tag{4.37}$$

Finally, the mean power flow $\tilde{P}$ radiated through a circular section defined by angles θ_1 and θ_2 and radius r_0 is obtained integrating Eq. (4.37). The resulting expression is

$$\begin{aligned} \tilde{P}(\theta_1,\theta_2) = & \frac{\omega}{2}\int_{\theta_1}^{\theta_2}\{\mathrm{Re}[\gamma_{3\theta,4z}]\mathrm{Im}[\varsigma_{3r\theta,4z}]-\mathrm{Im}[\gamma_{3\theta,4z}]\mathrm{Re}[\varsigma_{3r\theta,4z}] \\ & +\mathrm{Re}[\gamma_{3r,4z}]\mathrm{Im}[\varsigma_{3rr,4z}]-\mathrm{Im}[\gamma_{3r,4z}]\mathrm{Re}[\varsigma_{3rr,4z}]\}r_0\mathrm{d}\theta. \end{aligned} \tag{4.38}$$

The previous development is also valid for the simple tunnel case with a radial load applied on its bottom just replacing the receptances $\gamma_{3r,4z}$, $\gamma_{3\theta,4z}$ by $\beta_{3r,4r}$ and $\beta_{3\theta,4r}$ and the stresses responses $\varsigma_{3rr,4z}$ and $\varsigma_{3r\theta,4z}$ by $\varepsilon_{3rr,4r}$ and $\varepsilon_{3r\theta,4r}$.

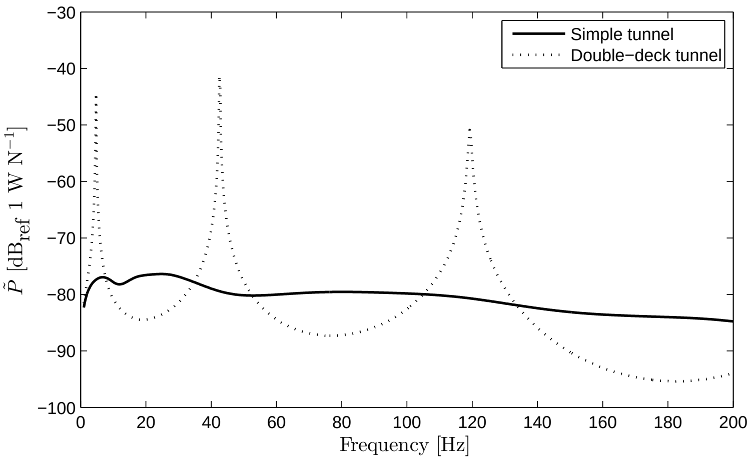

FIG. 4.4: Mean upwards power flow comparison between a simple tunnel and a double-deck tunnel with the load applied at the middle point of the interior floor. Results are plotted for $r = 10$ m.

4.3 Numerical results and discussion

Because the frequency range of interest in building response to train-induced vibrations is 1-80 Hz [76], the forced response of the plate is calculated using the eigenmodes found between 0 and 400 Hz. The same consideration has been made for the ring modes of the tunnel-soil structure. Also, because the inverted matrices in Eq. (D.51) are usually badly conditioned, an LU decomposition of them is performed to avoid numerical problems.

The mechanical parameters used for the interior floor, the tunnel and the soil models are detailed in Tables 3.1, 3.2 and 3.3 respectively.

In Fig. 4.4 a comparison between the power flow radiated through the upper half of a 10 m radius circumference for both types of tunnels is presented. Both cases are calculated using Eq. (4.32), taking into account that $\theta_1^{'} = \pi/2$ and $\theta_2^{'} = 3\pi/2$ for the simple tunnel and $\theta_1 = 0$ and $\theta_2 = \pi$ for the double-deck tunnel. The line load is applied at the centre of the plate, $y_4 = 5.45$ m. The calculations are done with a frequency resolution of $\Delta f = 0.25$ Hz from 1 to 200 Hz. As has been stated by Hussein and Hunt [89], when no wave reflection is considered, the upwards power flow is the one received by surface buildings. With the considered assumptions, the results clearly indicate that, for certain frequency ranges, the mean power flow radiated by double-deck tunnel reaches much higher values than the one radiated by the simple tunnel. As detailed in Table 4.1, the radiation peaks appear at frequencies close to those of the transverse eigenmodes of a strip plate with simple supported (SS) edges. This result can be understood considering the limit case of a tunnel-soil system much more rigid than the plate; In this case, the boundary conditions considered at the edges of the plate become the ones of the SS case,

Peak/Mode number	Frequency [Hz]	SS-SS eigenfrequency [Hz]
1	4.69	4.70
2	18.90	18.81
3	42.60	42.32
4	75.99	75.25
5	119.31	117.56
6	170.11	169.31

TABLE 4.1: Comparison between the frequencies where the radiated power flow for a double-deck tunnel is maximum and the transverse eigenfrequencies of a SS-SS strip plate.

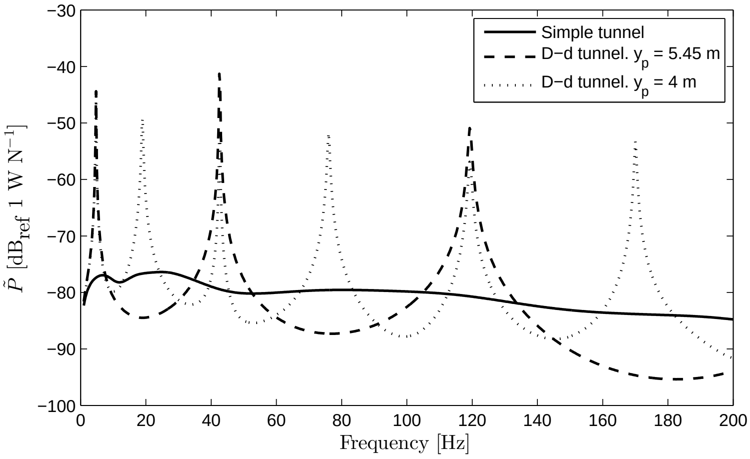

FIG. 4.5: Mean upwards power flow of a double-deck tunnel for different positions of the applied load. The simple tunnel case is also plotted.

which are written as

$$W_p\bigg|_{y_p=0,L_p} = 0, \qquad \frac{\mathrm{d}^2 W_p}{\mathrm{d}y_p^2}\bigg|_{y_p=0,L_p} = 0. \tag{4.39}$$

This fact can be of great help in the case of a tunnel embedded in hard ground, where the maximum radiation frequencies can be directly approximated to the roots of

$$\sin(\kappa_n L_p) = 0. \tag{4.40}$$

Fig. 4.5 presents the mean power flow radiated upwards by a double-deck tunnel for different positions of the external load. New peaks appear when the antisymmetric modes of the plate are excited increasing the differences between the radiation behaviour of both tunnels. The simple tunnel case is also plotted in the comparison.

Figs. 4.6 and 4.7 show the total radiated power flow for different values of the flexural

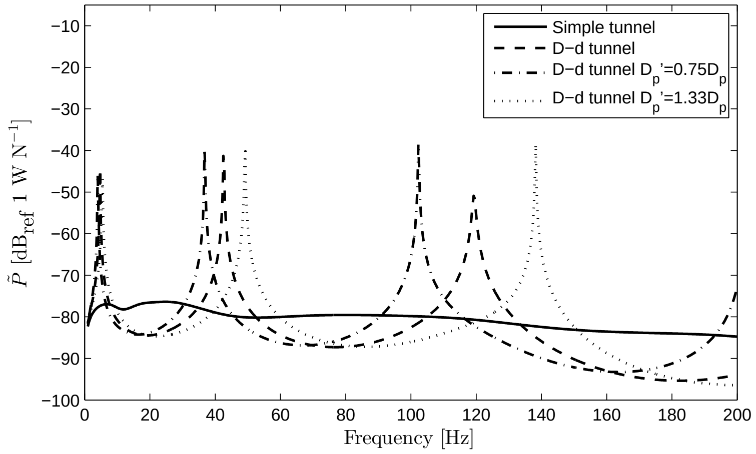

FIG. 4.6: Comparison of mean upwards power flow for different values of the flexural rigidity of the plate (D') when the load is applied at $y_p = 5.45$ m. The simple tunnel case is also plotted.

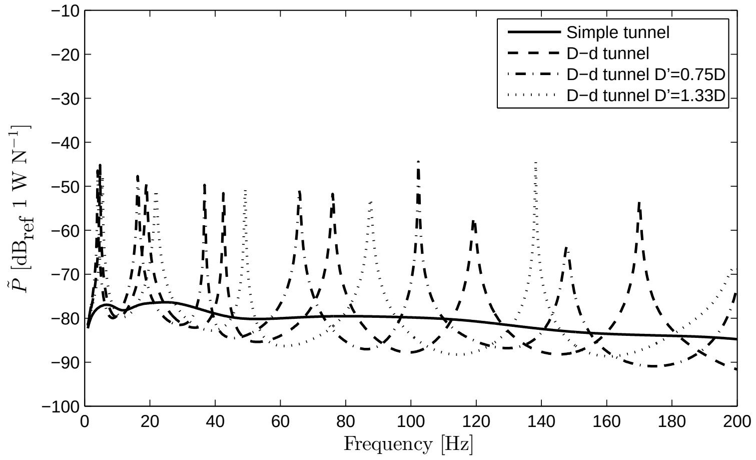

FIG. 4.7: Comparison of mean upwards power flow for different values of the flexural rigidity of the plate (D') when the load is applied at $y_p = 4$ m. The simple tunnel case is also plotted.

rigidity of the plate in the case when the external load is applied at the centre of the plate ($y_p = 5.45$ m) and when it is applied at $y_p = 4$ m. The radiation peaks are shifted to lower frequencies when the flexural rigidity is reduced and to higher frequencies when it is increased.

All the previous results have been focused on the global value of the mean power flow radiated, without considering its angular distribution. Figs. 4.8 to 4.11 show the mean local power flow for the most significant one-third octave bands in train-induced ground vibrations. The first comparison is done with different color scales but the other three use the same. The results have been calculated considering a pink noise excitation, again with a frequency resolution of $\Delta f = 0.25$ Hz. The angular and radial resolutions are $\Delta\theta = \frac{\pi}{180}$ rad and $\Delta r = 0.25$ m respectively.

In Fig. 4.8, which presents the results for the one-third octave with nominal midband frequency of 40 Hz, the obtained double-deck tunnel radiation is several orders of magnitude higher than the simple tunnel one. This result agrees with the peak frequency of 42.60 Hz obtained in Table 4.1 for the total radiated power flow. The differences between both tunnels are much smaller for the other one-third octave bands considered. In Fig. 4.9, the energy radiated by the double-deck tunnel is slightly higher than the one radiated by the simple tunnel while in Figs. 4.10 and 4.11 the simple tunnel radiates more energy than the double-deck one. Clear differences between the radiation patterns of both tunnels are observed in all the one-third octave bands studied. The most important of them refers to the amount of energy radiated vertically in each case. For the simple tunnel, the highest values of local power flow are mainly obtained at positions where $|x_t| > y_t$. The opposite is found in the double-deck tunnel, where an important fraction of the vibration energy is radiated towards the vertical direction. Another phenomena seen in Fig. 4.10 and especially in Fig. 4.11 is the tunnel shadowing of the vibration radiated upwards in the simple tunnel case. This phenomena can also be seen in the double-deck tunnel radiation patterns presented in Figs. 4.8 and 4.9. However, the decay of the local power flow values in these cases is much more moderate than the one found in the simple tunnel.

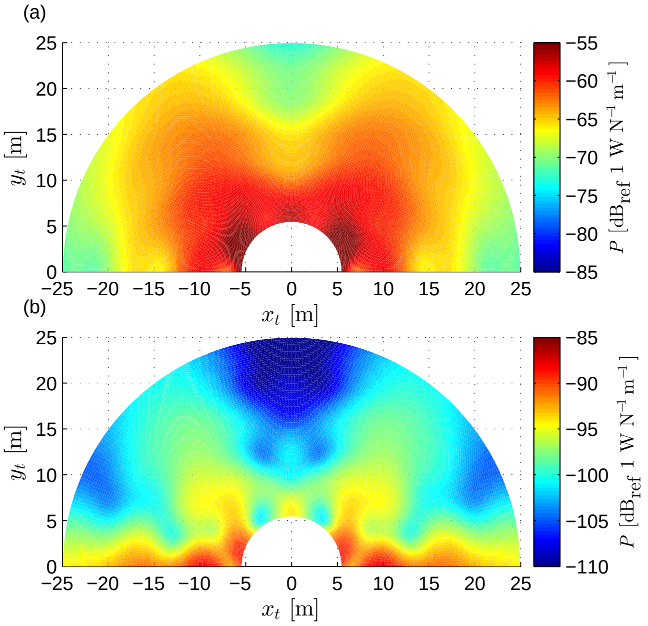

FIG. 4.8: Mean local power flow radiated upwards for the one-third octave with nominal midband frequency of 40 Hz. (a) Results for a double-deck tunnel. (b) Results for a simple tunnel. Different color scales are used.

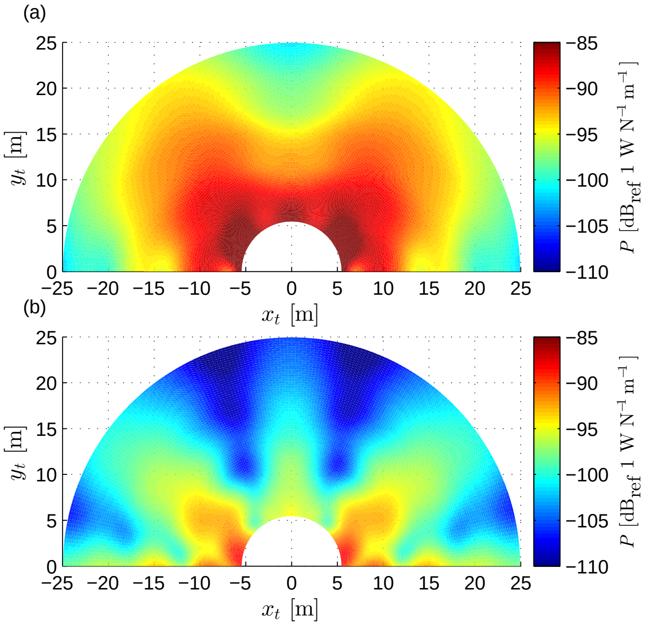

FIG. 4.9: Mean local power flow radiated upwards for the one-third octave with nominal midband frequency of 50 Hz. (a) Results for a double-deck tunnel. (b) Results for a simple tunnel.

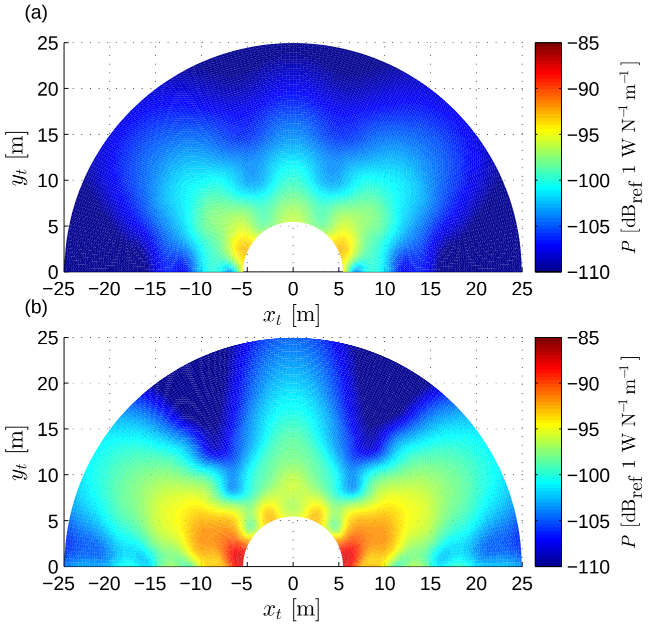

FIG. 4.10: Mean local power flow radiated upwards for the one-third octave with nominal midband frequency of 63 Hz. (a) Results for a double-deck tunnel. (b) Results for a simple tunnel.

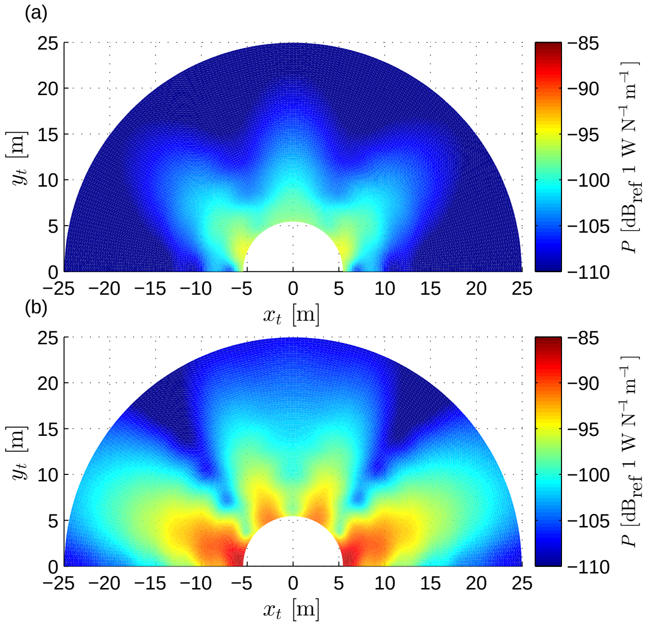

FIG. 4.11: Mean local power flow radiated upwards for the one-third octave with nominal midband frequency of 80 Hz. (a) Results for a double-deck tunnel. (b) Results for a simple tunnel.

4.4 Conclusions

An analytical model is presented for a double-deck circular tunnel under plane strain conditions. The receptance method has been used to obtain the forced response of the system to a harmonic line load. Classical thin plate theory is used to describe the dynamics of the plate and the two dimensional PiP formulation is considered for the tunnel and soil behaviours. The effects of changing the load position and of modifying the flexural rigidity of the plate are also studied. In the case of a stiff ground, a good approximation of the frequencies of maximum radiation is also proposed.

The mean power flow radiated by a double-deck tunnel is compared to the one radiated by a simple tunnel. Clear differences between their radiation magnitudes and patterns has been found. The ratio between the energy (or power) radiated upwards by the structures clearly depends on the excitation frequency considered. It has been found that, when this frequency is close to any of the transversal eigenfrequencies of the interior floor, the power radiated by the double-deck tunnel structure is several orders of magnitude higher than the one radiated by a simple tunnel. For frequencies far from any of these eigenfrequencies, this ratio is inverted, becoming the energy radiated by a simple tunnel slightly higher. From the radiation patterns of both tunnels, it is also concluded that the amount of energy directed vertically is much bigger for the double-deck tunnel case.

The presented method and a very similar comparison between the power flow radiated by a simple and by a double-deck tunnel have been recently published in [106].

Chapter 5

An energy flow study of a double-deck tunnel

This chapter presents an energy flow study of a double-deck tunnel structure excited by a static load moving at a constant speed. This type of excitation, known as quasi-static excitation, is the main source of ground-borne vibration in high speed trains [60, 61]. The chapter is divided into three sections. The first section derives the response of a generic tunnel model to a quasi static moving load, formulated in the stationary frame. The second section describes the proposed energy flow calculation, which considers the amount of energy that crosses a certain surface during the load circulation. Finally, the third section presents a numerical comparison between the energy radiated by a double-deck tunnel and the one radiated by a simple tunnel. The obtained results include the frequency content of the soil response, the total energy radiated upwards for a wide range of load speeds and the energy flow distribution for two types of soils. Important differences between the energy radiated by both structures are mainly found when the load circulates at very high speeds.

5.1 Response to a moving load

This section is devoted to obtain the displacement and stress fields caused by a unitary static load moving at a constant speed v_t. Assuming that the load is moving in the positive x-direction and that at a time $t = 0$ s its position is $x = 0$ m, it can be expressed as

$$p(x,t) = \delta(x - v_t t). \tag{5.1}$$

For obtaining the tunnel response to this type of excitation, the load is transformed to the wavenumber-frequency domain. Instead of assuming a harmonic motion (as was done in Chapters 3 and 4), a Fourier transform of the form presented in Eq. (A.1) is applied to Eq. (5.1). The resulting expression is

$$P(x,\omega) = \frac{1}{v_t}\mathrm{e}^{-\mathrm{i}\frac{\omega x}{v_t}}. \tag{5.2}$$

Now, applying Eq. (A.3) to Eq (5.2), the load in the frequency-wavenumber domain is finally given by

$$\bar{P}(k_x,\omega) = \frac{1}{v_t}\delta\left(k_x - \frac{\omega}{v_t}\right). \tag{5.3}$$

In the frequency-wavenumber domain, the response of the tunnel is directly obtained by multiplying Eq. (5.3) by the response of the tunnel to a harmonic point load. The displacement field $\bar{\mathbf{U}}$ caused by the static moving load can be expressed as

$$\bar{\mathbf{U}}(k_x,\omega) = \bar{\mathbf{H}}_u\left(k_x,\omega\right)\frac{1}{v_t}\delta\left(k_x - \frac{\omega}{v_t}\right) \tag{5.4}$$

where $\bar{\mathbf{H}}_u$ is the displacement field generated by a harmonic point load.

To obtain the displacement field in the space-time domain, Eq. (5.4) has to be properly antitransformed. First, the displacement in the space-frequency domain is obtained applying Eq. (A.4) to Eq. (5.4). Using the properties of the Dirac's delta, the result can be written as

$$\mathbf{U}(x,\omega) = \frac{1}{(2\pi)}\frac{1}{v_t}\bar{\mathbf{H}}_u\left(\frac{\omega}{v_t},\omega\right)\mathrm{e}^{-\mathrm{i}\left(\frac{\omega x}{v_t}\right)}. \tag{5.5}$$

The displacement field in the space-time domain is obtained applying Eq. (A.2) to Eq. (5.5), which gives the following result

$$\mathbf{u}(x,t) = \frac{1}{(2\pi)^2 v_t}\int_{-\infty}^{\infty}\bar{\mathbf{H}}_u\left(\frac{\omega}{v_t},\omega\right)\mathrm{e}^{\mathrm{i}\omega t'}\mathrm{d}\omega, \tag{5.6}$$

where $t' = t - \dfrac{x}{v_t}$.

As Xing and Price [107] expose, in a power/energy flow analysis, the obtained results must be measurable quantities. Due to this, in the power flow definition only the real part of the velocity of vibration and stress have to be considered, because they are the ones carrying their physical meaning. Taking this requirement into account, the velocity of vibration field, which is directly obtained from the displacement field by derivation, should be written as

$$\mathbf{v}(x,t) = \mathrm{Re}\left[\dot{\mathbf{u}}(x,t)\right] = \frac{1}{(2\pi)^2 v_t}\mathrm{Re}\left[\int_{-\infty}^{\infty}\mathrm{i}\omega\bar{\mathbf{H}}_u\left(\frac{\omega}{v_t},\omega\right)\mathrm{e}^{\mathrm{i}\omega t'}\mathrm{d}\omega\right]. \tag{5.7}$$

The stress field, which is obtained following the steps previously performed for the displacement field, can be written as

$$\boldsymbol{\tau}(x,t)=\frac{1}{(2\pi)^2 v_t}\mathrm{Re}\left[\int_{-\infty}^{\infty}\bar{\mathbf{H}}_\tau\left(\frac{\omega}{v_t},\omega\right)\mathrm{e}^{\mathrm{i}\omega t'}\mathrm{d}\omega\right], \tag{5.8}$$

where $\bar{\mathbf{H}}_\tau$ is the stress response of the system to a harmonic point load. As in the case of the displacement and velocity of vibration fields, this expression is not restricted to a particular tunnel model.

5.2 Energy flow calculation

The circulation of a static load along a tunnel generates a transient response on the soil. It is due to the nature of this response that a power flow calculation like the one presented in Chapter 4 is replaced in this chapter by an energy flow calculation.

The energy flow E that crosses a certain surface S during the load circulation is expressed as

$$E=\int_{-\infty}^{\infty}\tilde{P}(t)\mathrm{d}t, \tag{5.9}$$

where $\tilde{P}(t)$ is the power flow radiated across the surface and is given by

$$\tilde{P}(t)=\int_S P(x,\theta,t)\mathrm{d}S=\int_S \mathbf{v}(x,\theta,t)\cdot\boldsymbol{\tau}(x,\theta,t)\mathrm{d}S. \tag{5.10}$$

Because the tunnel is assumed to be embedded in a full-space, no wave reflections are considered and the only radiation of interest is the one propagating upwards [89]. With this in mind, the chosen surface of integration is the cylindrical surface plotted with wider lines in Fig 5.1. The proposed surface is defined by the measuring radius r_m, the space resolution Δx and the angles θ_1 and θ_2, which will depend on the considered origin of the angular coordinate, but will obey that $\theta_2-\theta_1=\pi$ rad. Substituting Eq. (5.10) into Eq. (5.9), the total energy radiated across the surface can be written as

$$E=\int_{x_1}^{x_2}\mathrm{d}x\int_{\theta_1}^{\theta_2}r_m\mathrm{d}\theta\int_{-\infty}^{\infty}P(x,\theta,t)\mathrm{d}t, \tag{5.11}$$

where $x_1=x_m-\dfrac{\Delta x}{2}$ and $x_2=x_m-\dfrac{\Delta x}{2}$.

Some considerations are used in order to simplify the previous calculation. Because the width of the considered surface in the load moving direction is equal to the chosen numerical resolution Δx (see Appendix A), the integral of the energy radiated in the

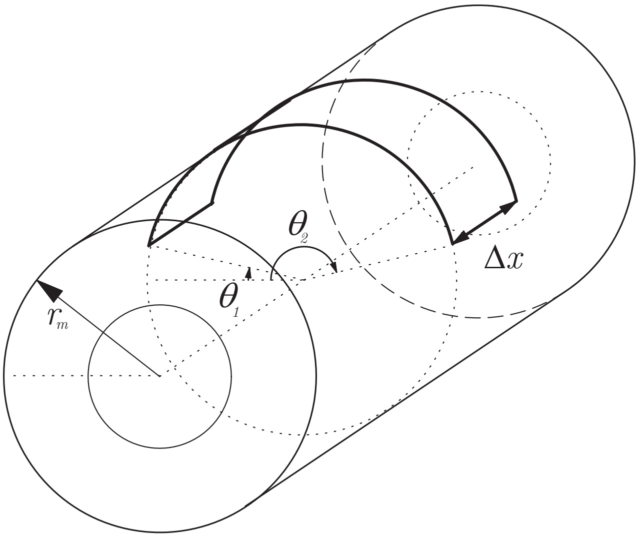

FIG. 5.1: Integration surface chosen for the proposed energy flow calculation.

x-direction is simply given by the multiplication of the radiated energy at $x = x_m$ by Δx. Also, because the system is infinite in the x-direction, the energy radiated across the proposed surface is independent of the cross-section x_m considered and the results are obtained at a cross-section $x_m = 0$ for simplicity. Using both properties, the energy radiated across the defined surface can be written as

$$E = r_0 \, \Delta x \int_{\theta_1}^{\theta_2} \int_{-\infty}^{\infty} \mathbf{v}(0,\theta,t) \cdot \boldsymbol{\tau}(0,\theta,t) \mathrm{d}t \mathrm{d}\theta, \tag{5.12}$$

where

$$\mathbf{v}(0,\theta,t) = \frac{1}{(2\pi)^2 v_t} \mathrm{Re} \left[\int_{-\infty}^{\infty} \mathrm{i}\omega \bar{\mathbf{H}}_u \left(\frac{\omega}{v_t}, \omega \right) \mathrm{e}^{\mathrm{i}\omega t} \mathrm{d}\omega \right] \tag{5.13}$$

and

$$\boldsymbol{\tau}(0,\theta,t) = \frac{1}{(2\pi)^2 v_t} \mathrm{Re} \left[\int_{-\infty}^{\infty} \bar{\mathbf{H}}_\tau \left(\frac{\omega}{v_t}, \omega \right) \mathrm{e}^{\mathrm{i}\omega t} \mathrm{d}\omega \right]. \tag{5.14}$$

In both results it has been used that $t' = t$ for the considered cross-section.

5.3 Numerical results

This section presents a comparison between the energy radiated by the double-deck tunnel presented in Chapter 3 and the one radiated by a simple tunnel. Before obtaining the energy flow results, the frequency content of both tunnel responses is presented. The comparison of the energy radiated for a wide range of load speeds and the energy flow distribution on the surrounding ground generated by both types of tunnels are also plotted and discussed.

5.3.1 Frequency spectra

This subsection presents the frequency content of the velocity of vibration and stress fields of a point of the soil for different values of the load speed. These frequency distributions are the transformed expressions of $\mathbf{v}$ and $\boldsymbol{\tau}$, which need to be calculated to obtain, using Eq. (5.12), the energy flow radiated by the structure under the action of a static moving load. This load is applied at the bottom of the simple tunnel and centre of the interior floor floor of the double-deck tunnel.

The frequency spectra of the soil's velocity of vibration and stress for load speeds of 40, 80 and 200 m s^{-1} are shown in Figs. 5.2 to 5.4. The third speed can't be considered as a realistic speed for a train circulating in a tunnel but it is also studied in order to understand the dynamical response of the systems. The results are obtained at $r_m = 10$ m and at $\theta^{'} = \pi$ rad for the simple tunnel and $\theta = \pi/2$ rad for de double-deck tunnel (The results are obtained in the same position of the soil but different angular coordinate origins are used in both tunnels, as can be seen in Figs. 4.1 and 4.3). The numerical results are computed considering a frequency resolution $\Delta f = 0.05$ Hz with a sampling frequency $f_s = 200$ Hz for the two firsts speeds and $f_s = 400$ Hz for the third one. To ensure the obtention of accurate results (see Section 3.6.2), $N_r = 20$ ring modes and a truncation frequency $f_t = 4800$ Hz have been used. The interior floor, tunnel and soil properties used are those presented in Tables 3.1, 3.2 and 3.3.

In each figure, subplots (a) and (b) are the velocity of vibration and stress fields for the simple tunnel while subplots (c) and (d) are the same fields for the double-deck tunnel. Both fields are separated into their components but, due to the system symmetries in the chosen point of calculation, only the radial and tangential displacements are not null.

As can be seen from the figures, the higher the load speed is the wider the range of significant frequencies becomes. The soil response when the load speed is 40 m s^{-1} is almost negligible over 5 Hz for both tunnels. When the load moves at 80 m s^{-1}, their response is significant up to values around 10 Hz. Finally, for a load speed of 200 m s^{-1}, while the double-deck tunnel response is almost zero over 30 Hz, the simple tunnel shows a much more smooth decay than in the previous cases (see Fig 5.5). Despite this, the loss of accuracy caused by considering a sampling frequency of 200 Hz is negligible, at least for the calculations performed in this chapter. If very accurate results are desired, the

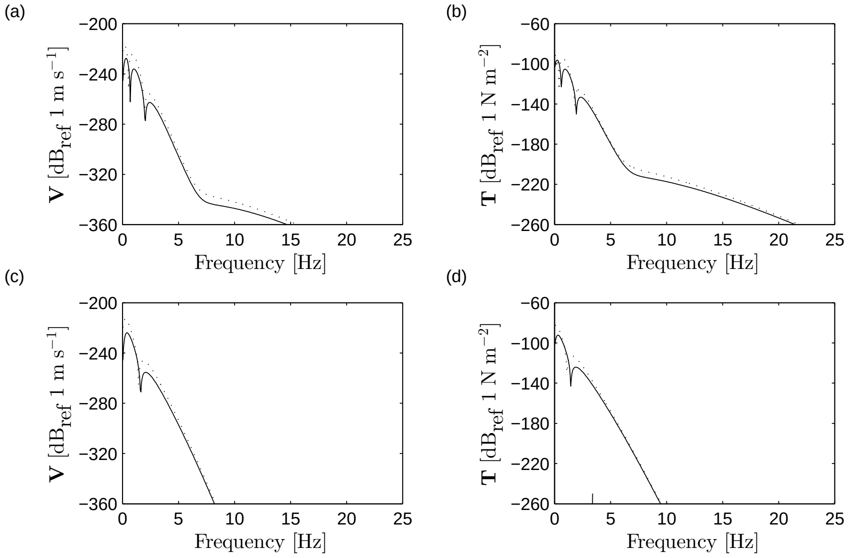

FIG. 5.2: Soil's velocity of vibration and stress fields at $r_m = 10$ m and $\theta' = \pi$ rad or $\theta = \pi/2$ rad for a simple and for a double-deck tunnel (subplots (a)-(b) and (c)-(d), respectively) when the moving load speed is 40 m s^{-1}. Only the axial (continuous line) and radial (dotted line) components of the fields are not null.

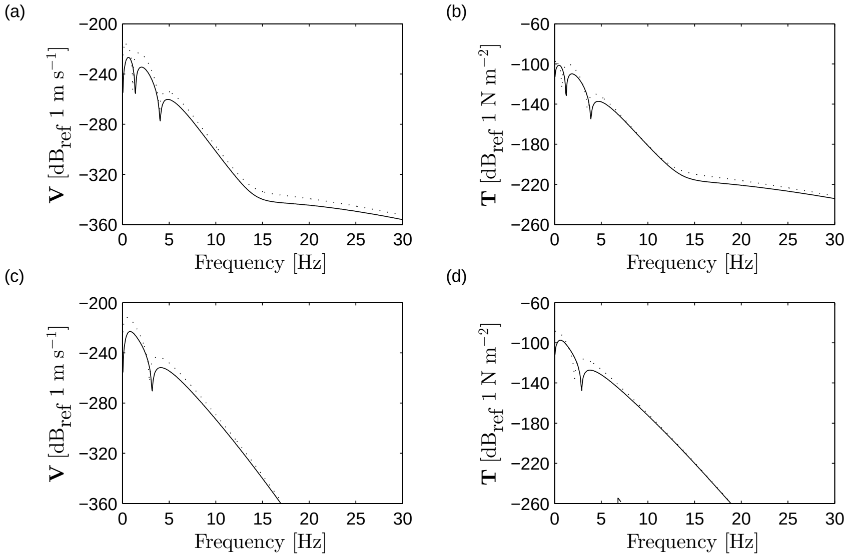

FIG. 5.3: Soil's velocity of vibration and stress fields at $r_m = 10$ m and $\theta' = \pi$ rad or $\theta = \pi/2$ rad for a simple and for a double-deck tunnel (subplots (a)-(b) and (c)-(d), respectively) when the moving load speed is 80 m s^{-1}. Only the axial (continuous line) and radial (dotted line) components of the fields are not null.

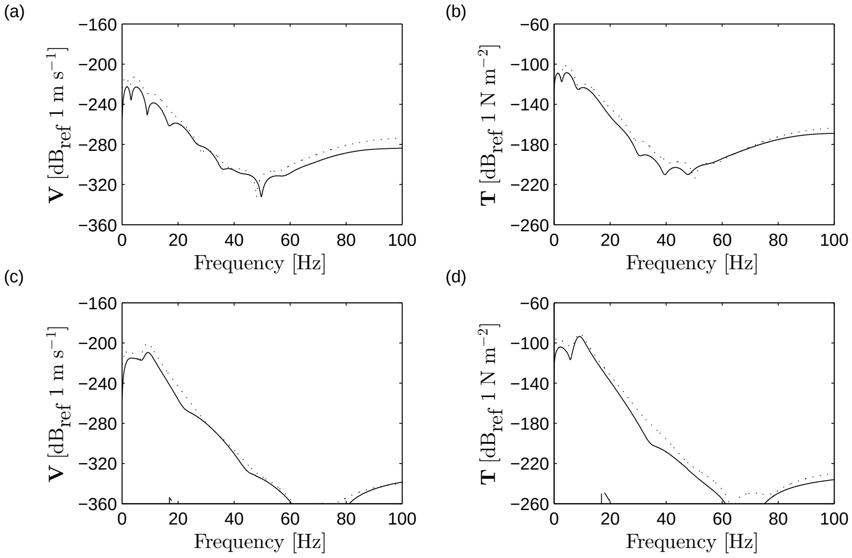

FIG. 5.4: Soil's velocity of vibration and stress fields at $r_m = 10$ m and $\theta' = \pi$ rad or $\theta = \pi/2$ rad for a simple and for a double-deck tunnel (subplots (a)-(b) and (c)-(d), respectively) when the moving load speed is 200 m s^{-1}. Only the axial (continuous line) and radial (dotted line) components of the fields are not null.

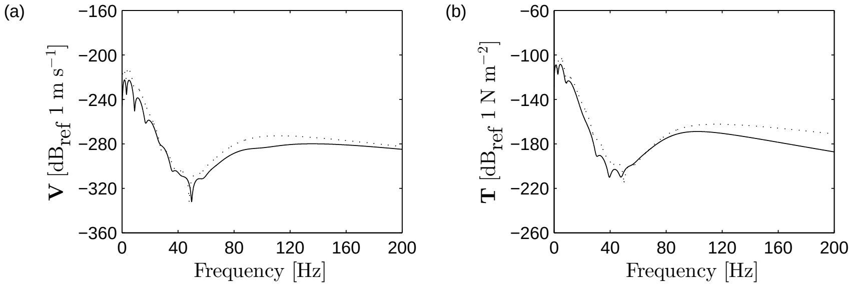

FIG. 5.5: Soil's velocity of vibration and stress fields at $r_m = 10$ m and $\theta' = \pi$ rad for a simple tunnel when the moving load speed is 200 m s^{-1}. Results are plotted up to 200 Hz. Only the axial (continuous line) and radial (dotted line) components of the fields are not null.

response at higher excitation frequencies has to be taken into account but, if a higher sampling frequency is considered, the previously defined values of N_r and f_t may no longer ensure the convergence of the results.

5.3.2 Power flow results

Fig. 5.6 shows a comparison between the power flow $\tilde{P}$ radiated by a simple and a double-deck tunnels for the same load speeds previously considered. The result is obtained at $r_m = 10$ m and considering a space resolution $\Delta x = 1$ m. For the simple tunnel $\theta_1' = \pi/2$ rad and $\theta_2' = 3\pi/2$ rad and for the double-deck tunnel $\theta_1 = 0$ rad and $\theta_2 = \pi$ rad. Again,

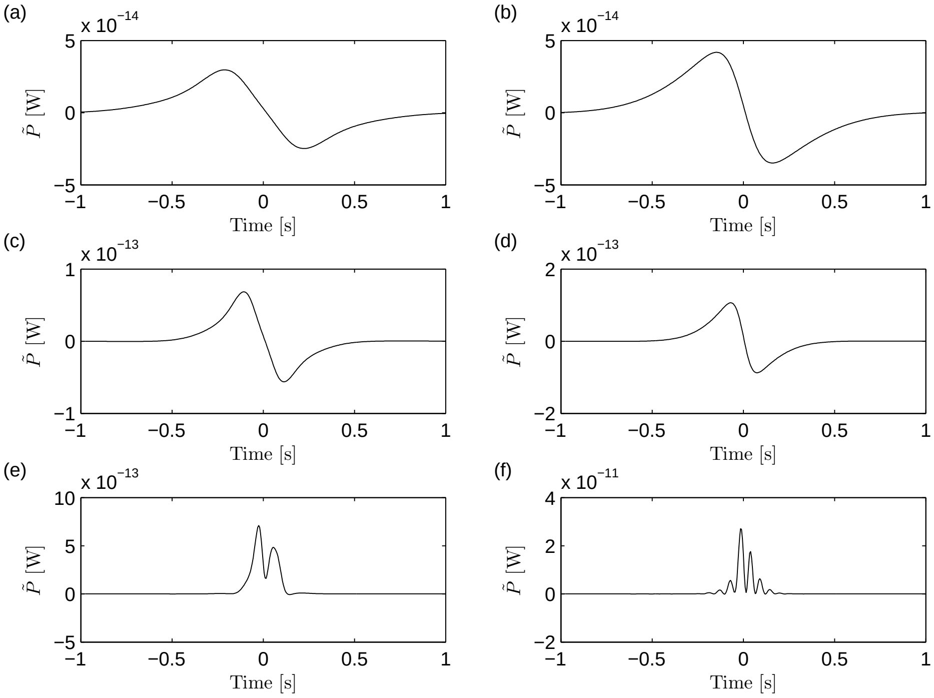

FIG. 5.6: Comparison of the power flow radiated upwards by a simple tunnel (subplots (a),(c) and (e)) and a double-deck tunnel (subplots (b),(d) and (f)) at $r_m = 10m$. Results are obtained for three different load speeds: 40 m s^{-1} (subplots (a) and (b)), 80 m s^{-1} (subplots (c) and (d)) and 200 m s^{-1} (subplots (e) and (f)).

the calculations have been performed considering $\Delta f = 0.05$ Hz, $f_s = 200$ Hz, $N_r = 20$ and $f_t = 4800$ Hz. With the chosen frequency resolution $\Delta f = 0.05$ Hz, the response of the soil is obtained for $t \in [-10, 10]$ s. However, as can be seen in the six subfigures, because of the transient nature of the excitation, the soil response is only significant in a small time interval around $t = 0$ s and the results are only plotted in the range $[-1, 1]$ s.

Two numerical considerations are done when the velocity of vibration and stress fields $\mathbf{V}$ and $\mathbf{T}$ are antitransformed to the time domain. One, the velocity of vibration and stress fields at $\omega = 0$ are not calculated but defined as zero. Because of the term iω of Eq. (5.13), this definition has no change on the results and allows to avoid the numerical instabilities found in this case. The other, because the velocity of vibration and stress fields defined in Eq. (5.13) and (5.14) must be real valued, its frequency spectra obeys that $F(-\omega) = F^*(\omega)$, where the asterisk means complex conjugate. Using this property, the calculation of negative frequencies is unnecessary.

Comparing the obtained power flow of both tunnels it is found that, while the dynamic response of both tunnels is very similar for load speeds of 40 and 80 m s^{-1}, clear differences between the power flow magnitude and the shape of the response are obtained for a load speed of 200 m s^{-1}. It seems that, at this unrealistic speed, the interaction of the interior floor and the tunnel causes a heavy increase of the power radiated upwards. This effect is properly studied in the next subsection.

5.3.3 Total energy radiated upwards

This subsection presents a comparison between the total energy radiated upwards by both tunnel structures for a wide range of load speeds. The results are obtained computing Eq. (5.12) for load speeds between 25 and 250 m s^{-1} with a resolution $\Delta v_t = 2.5$ m s^{-1}. All the results are obtained considering a sampling frequency $f_s = 200$ Hz with a frequency resolution $\Delta f = 0.05$ Hz, which ensures enough precision of the results for the whole set of speeds. $N_r = 20$ samples, $f_t = 4800$ Hz and an angular resolution $\Delta\theta = \pi/60$ rad has been considered in the calculations.

In Fig 5.7, a comparison between the total energy radiated by the simple and the double-deck tunnels is presented. The mechanical parameters used are those presented in Tables 3.1, 3.2 and 3.3. The subplot (a) considers $r_m = 10$ m while the subplot (b) $r_m = 50$ m.

Two main behaviours found for both measuring distances should be highlighted. One, the existence, for both tunnels, of a narrow band of speeds where the radiated energy shows a fast increase. This narrow band is found at speeds between 135 and 145 m s^{-1}, values that are around the S-wave speed of the soil. The other, the heavy increase of the radiated energy by a double-deck tunnel when the load speed is over 200 m s^{-1}. It appears that when the load speed becomes similar to a phase speed of the interior floor-tunnel system, the energy radiated experiments a huge increase. These phenomena occurs at speeds much higher from those reached by any underground train so, in the range of realistic train speeds, the energy radiated by a double-deck tunnel in quasi-static loading conditions is similar to that radiated by a simple tunnel. The results obtained at $r_m = 50$ m show again the previously described phenomena with only a decrease of the value of the total energy radiated, mainly caused by the material damping of the soil.

A very similar comparison is performed in Fig 5.8, where the total energy radiated upwards for a typical Tertiary (subplot (a)) and a soft Quaternary soil (subplot (b)), is calculated. Their mechanical properties and P- and S-wave speeds are the ones detailed in Table 5.1. As before, a heavy increase of the total energy radiated occurs in a narrow

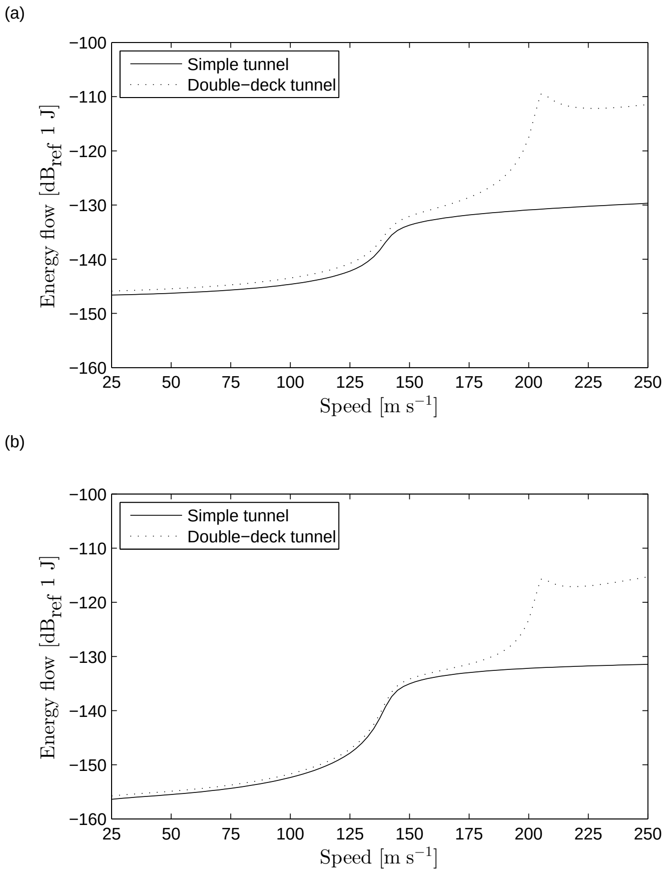

FIG. 5.7: Total energy radiated upwards for different values of the load speed and considering a simple and a double-deck tunnel. (a) Results at $r_m = 10$ m. (b) Results at $r_m = 50$ m.

Parameter	Tertiary soil	Quaternary soil
E_s	100 MPa	30 MPa
ν_s	0.3	0.3
ρ_s	1950 kg m^{-3}	1950 kg m^{-3}
c_P	262.74 m s^{-1}	143.91 m s^{-1}
c_S	140.44 m s^{-1}	76.92 m s^{-1}

TABLE 5.1: Mechanical parameters of the considered soils.

band of speeds that is independent of the type of tunnel considered. This increase is now found between 70 and 80 m s^{-1}, which is again around the S-wave phase speed of the soil. It is also found that reaching the P-wave speed has no influence on the radiated energy. This is particulary clear for the second type of soil, where the P-wave speed is much lower than the maximum speed considered in the calculations. The heavy increase of the energy radiated by the double-deck tunnel is again obtained for load

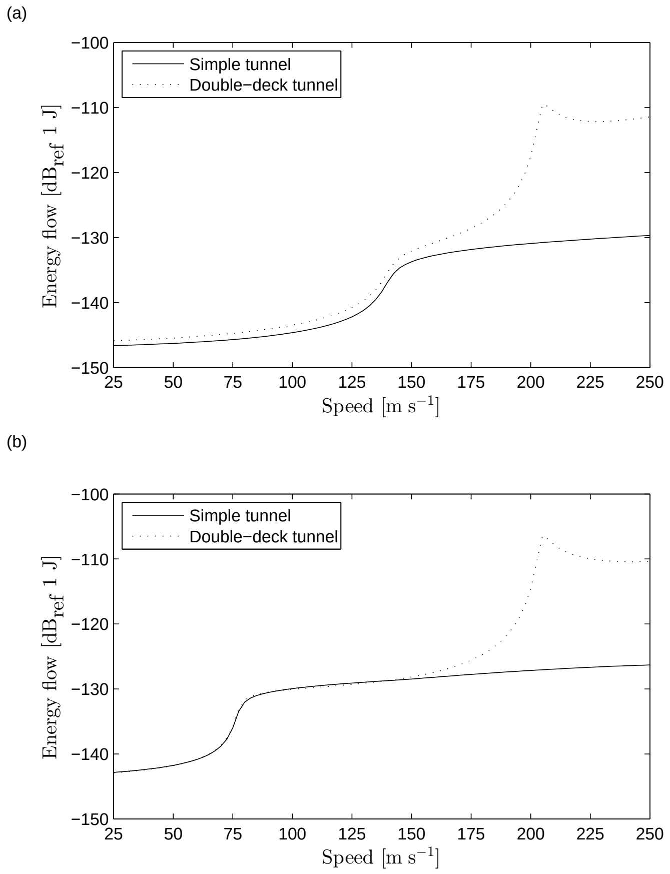

Fig. 5.8: Total energy radiated upwards for different values of the load speed and considering a simple and a double-deck tunnel. Two types of soil are considered: A typical Tertiary soil (a) and a soft Quaternary soil (b).

speeds above 200 m s^{-1}. The change of the soil properties has had almost no influence on this phenomena.

Fig. 5.9 shows the energy radiated by a double-deck tunnel for different positions of the static moving load. Significant differences are only obtained at high values of the load speed.

5.3.4 Energy flow distribution

The last result presented is a comparison between the energy flow distributions obtained for both tunnels. The comparisons are done considering a load speed of 40 and 80 m s^{-1} and for the two types of soil defined in Table 5.1. The results are presented in Figs. 5.10 to 5.13. Once more, a sampling frequency of 200 Hz with $\Delta f = 0.05$ Hz, $N_r = 20$ samples and $f_t = 4800$ Hz has been considered. The results are presented from $r_{\text{int}} =$

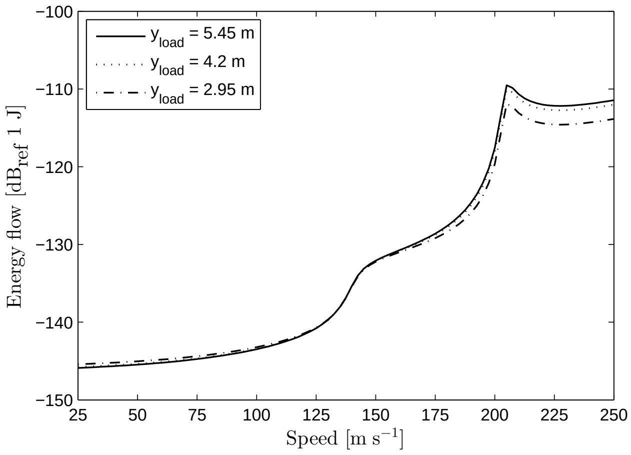

FIG. 5.9: Total energy radiated upwards for different positions and speeds of the load.

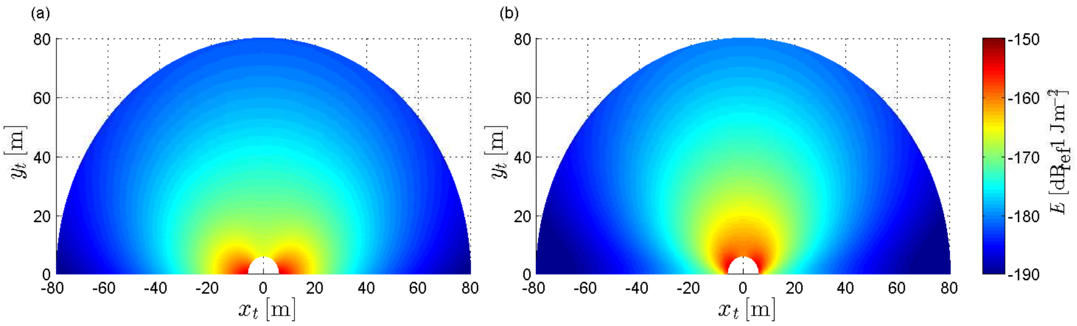

FIG. 5.10: Energy flow distribution in a Tertiary soil when $v_t = 40$ m s^{-1}, (a) for a simple tunnel and (b) for a double-deck tunnel.

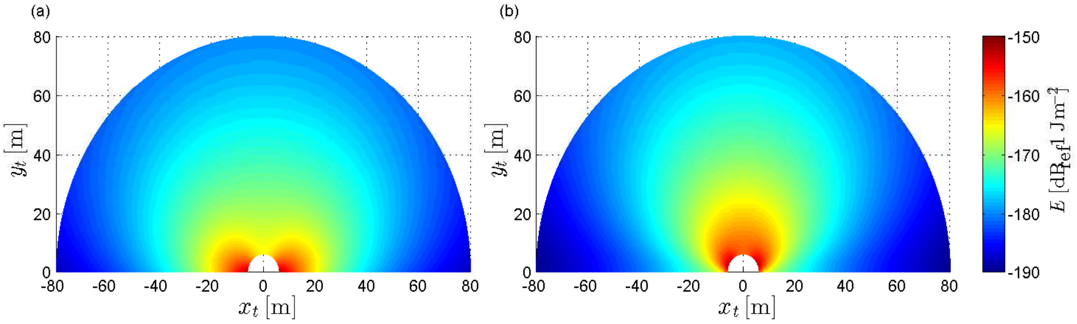

FIG. 5.11: Energy flow distribution in a Tertiary soil when $v_t = 80$ m s^{-1}, (a) for a simple tunnel and (b) for a double-deck tunnel.

6 m to $r_{\text{ext}} = 80$ m with an angular resolution $\Delta\theta = \pi/60$ rad and a radial resolution $\Delta r = 2$ m. A system of coordinates x_t, y_t equal to the one considered in Fig. 4.1 is defined in the considered cross-section. x_t should not be confused with the x-coordinate used along this chapter and Chapter 3.

For the Tertiary soil, where the considered load speeds are below the S-wave phase speed,

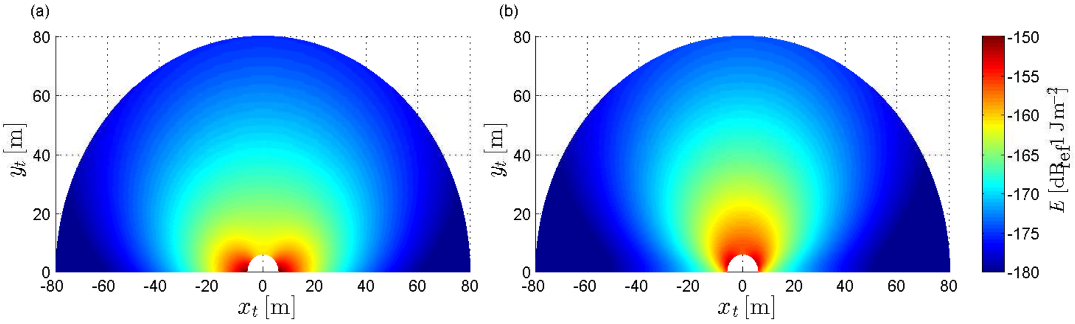

FIG. 5.12: Energy flow distribution in a Quaternary soil when $v_t = 40$ m s^{-1}, (a) for a simple tunnel and (b) for a double-deck tunnel.

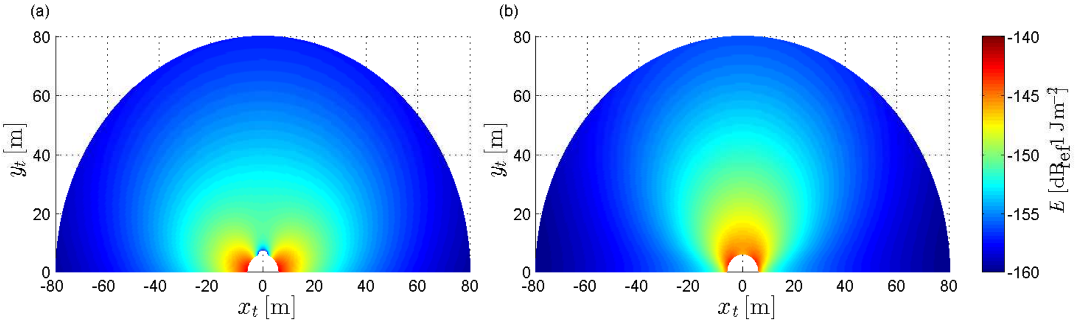

FIG. 5.13: Energy flow distribution in a Quaternary soil when $v_t = 80$ m s^{-1}, (a) for a simple tunnel and (b) for a double-deck tunnel. A different color scale has been used this time.

the radiated energy distribution doesn't exhibit significant changes when the load speed is doubled. In contrast, for the soft Quaternary soil, the effect of approaching the S-wave speed is clearly visible, showing an important increase of the total radiated energy in the second load speed case. However, the obtained distributions only show important changes in the total energy radiated, not in its distribution.

In all cases important differences are found between the radiation distribution of both tunnels. The region found directly upwards the tunnel receives a much higher amount of energy in the double-deck tunnel case. In the simple tunnel case, this region seems to be more shadowed by the tunnel structure and the smallest radiation values are found there.

5.4 Chapter conclusions

In this chapter, a comparison has been performed between the energy radiated by a simple and a double-deck tunnel when both are excited by a static load moving at a constant speed. The frequency spectrums of the velocity of vibration and stress fields generated by this type of load have been studied for different load speeds. The maximum frequency of interest has been found to be clearly dependent of the considered load speed but, in all cases, the obtained spectra is dominated by low frequencies. These results have been used to define an adequate frequency sampling for the energy flow calculations.

The total energy radiated upwards by both tunnels has been determined for a wide range of load speeds. The effects induced by the soil properties and the tunnel interior floor have clearly been identified by considering two different type of soils. For both soils, an increase of the radiated energy has been found when the load speed is similar to the S-wave phase speed. Important differences between both types of tunnel are only found for load speeds over 200 m s^{-1}, where the energy radiated by the double-deck tunnel is much higher than the one radiated by the simple tunnel. These load speeds are far above those typically found in underground trains and it can be concluded that, for typical train speeds and soil parameters, the responses of a double-deck and of a simple tunnel to a static moving load are similar.

The energy flow distributions for both type of tunnels and soils have also been presented for load speeds of 40 and 80 m s^{-1}. Only the radiation magnitude of the tunnels shows significant changes when these parameters are modified. Also, from a comparison between the radiation patterns of both tunnels it can be concluded that the region that lies directly upwards of the tunnel receives a much higher amount of energy in the double-deck tunnel case.

Chapter 6

Complete track-tunnel-soil model

In this chapter, a superstructure model is coupled to the upper deck of the double-deck tunnel model presented in Chapter 3. With this, a complete track-tunnel-soil model for a double-deck circular tunnel embedded in a full-space is obtained. The superstructure model considered is presented in the first section and coupled to the tunnel's interior floor in the second. The analytical formulation of the complete track-tunnel-soil model is finally presented in the third section. The proposed model uses again the receptance method [19] and separates the global structure into the track-interior floor system and the tunnel-soil system.

6.1 Superstructure model

The superstructure modelled in this work is the one that has been implemented in Line 9 of Barcelona Underground System, where, as can be seen in Fig. 6.1, the rails are fixed to the interior floor of the double-deck tunnel by means of Direct Fixation Fasteners (DFF).

Both rails are modelled as Bernoulli-Euler beams of infinite extent in the train circulating direction. Knothe and Grassie [64] determined that this is an adequate beam model for the range of frequencies studied in this work [74]. The DFF are modelled as a continuous massless distribution of springs and dashpots with a stiffness per unit of length k_F and a viscous damping per unit of length c_F, respectively.

FIG. 6.1: Direct Fixation Fasteners (DFF) used in Line 9 of Barcelona Underground System.

A scheme of the proposed model and the chosen Cartesian system of coordinates are presented in Fig. 6.2.

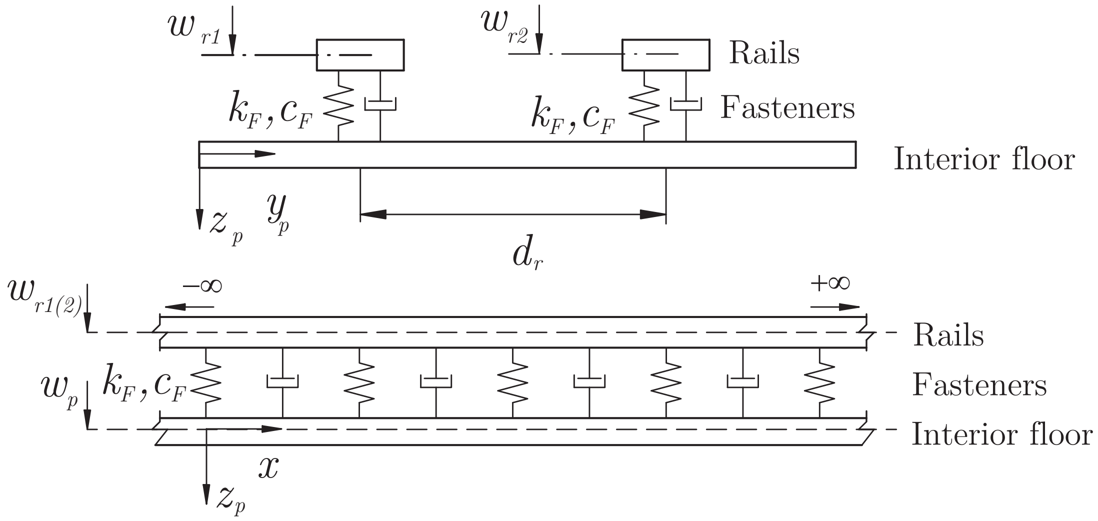

FIG. 6.2: Considered model for the rails fixed at the interior floor.

The positions where the rails are coupled to the interior floor are named y_1 and y_2 respectively. The rails are not necessarily centered in the middle of the plate but its separation is given by $d_r = y_2 - y_1$. It is assumed that only vertical loads are applied on the rails so, because in the beam model considered the vertical equation of motion is uncoupled from the horizontal and axial ones, only vertical displacements (deflections) are considered. These deflections are described by w_{r_1} and w_{r_2} respectively.

The equation of motion of both rails can be written as

$$\begin{aligned} E_r I_r \frac{\partial^4 w_{r_i}}{\partial x^4} + \rho_r S_r \frac{\partial^2 w_{r_i}}{\partial t^2} + k_F \left[w_{r_i} - w_p(y_i) \right] & + \\ c_F \left(\frac{\partial w_{r_i}}{\partial t} - \frac{\partial w_p(y_i)}{\partial t} \right) & = \quad p_i(x,t), \quad i = 1, 2, \end{aligned} \tag{6.1}$$

where E_r is the Young's modulus of the rail, I_r is its second moment of area, ρ_r is its density and S_r is its cross-sectional area. $w_p(y_i)$ are the deflections of the interior floor at the rails' positions and $p_i(x,t)$ are the applied loads on the rails (usually, the wheel-rail interaction forces).

Considering harmonic motion and applying Eq. (A.3), Eq. (6.1) takes the form

$$\left(E_r I_r k_x^4 - \rho_r S_r \omega^2 + k_F + \mathrm{i}\omega c_F \right) \bar{W}_{r_i} - \left(\mathrm{i}\omega c_F + k_F \right) \bar{W}_p(y_i) = \bar{P}_i, \tag{6.2}$$

where the notation defined in Section 3.1 has been used.

The loss of energy in the rails caused by microstructural friction mechanics is modelled assuming a complex valued Young's modulus E_r^* of the form

$$E_r^* = E_r \left(1 + \mathrm{i}\eta_E \right), \tag{6.3}$$

where η_E is the rail loss factor. In the same way, hysteretic damping is also considered in the fasteners by assuming a complex valued stiffness k_F^* of the form

$$k_F^* = k_F \left(1 + \mathrm{i}\eta_F \right), \tag{6.4}$$

being η_F the fastener loss factor. With this last definition, hysteretic or viscous damping can be used in the superstructure model.

6.2 Track-interior floor model

The coupling between the superstructure model described in Section 6.1 and the interior floor model presented in Section 3.3 is performed in the wavenumber-frequency domain. A general and a simplified coupling models are proposed. An alternative coupling model between an infinite plate and a track has been presented by Otero [1].

6.2.1 General rail coupling

When the rails are excited by external loads, the interior floor of the double-deck tunnel is also excited by rail-interior floor coupling loads, which can be expressed as

$$p(x, y_p, t) = (k_F^* + \mathrm{i}\omega c_F) \sum_{i=1}^{2} \delta(y_p - y_i) \left[w_{r_i}(x, t) - w_{p_i}(x, t) \right], \tag{6.5}$$

where $w_{p_i}(x, t) = w_p(x, y_i, t)$.

Assuming harmonic motion and applying Eq. (A.3) to Eq. (6.5), the wavenumber distribution of the applied load can be written as

$$\bar{P}(y_p) = (k_F^* + \mathrm{i}\omega c_F) \sum_{i=1}^{2} \delta(y_p - y_i)[\bar{W}_{r_i} - \bar{W}_p(y_i)] \tag{6.6}$$

and the load coefficients p_n, defined in Eq. (3.26), becomes

$$p_n = \frac{k_F^* + \mathrm{i}\omega c_F}{C_n} \sum_{i=1}^{2} \left[\bar{W}_{r_i} - \bar{W}_{p_i} \right] \bar{W}_n(y_i). \tag{6.7}$$

The interior floor deflection can be obtained by substituting Eq. (6.7) into Eq. (3.31). The resulting expression is

$$\bar{W}_p(y_p) = \sum_{i=1}^{2} \left[\bar{W}_{r_i} - \bar{W}_{p_i} \right] I_i(y_p), \tag{6.8}$$

where

$$I_i(y_p) = \left(k_F^* + \mathrm{i}\omega c_F \right) \sum_{n=1}^{\infty} \frac{\bar{W}_n(y_p)\bar{W}_n(y_i)\mathrm{e}^{\mathrm{i}\phi_n}}{C_n \rho_p h_p \sqrt{(\omega_n^2 - \omega^2)^2 + \omega_n^4 \eta_p^2}}. \tag{6.9}$$

In Eq. (6.8) the deflection of the interior floor at an arbitrary position y_p is related to its deflection at the position of both rails. The equations obtained considering the particular cases $y_p = y_1$ and $y_p = y_2$ are

$$\begin{aligned} \bar{W}_{r_1} I_1(y_1) - \bar{W}_{p_1} \left[1 + I_1(y_1) \right] + \bar{W}_{r_2} I_2(y_1) - \bar{W}_{p_2} I_2(y_1) &= 0, \\ \bar{W}_{r_1} I_1(y_2) - \bar{W}_{p_1} I_1(y_2) + \bar{W}_{r_2} I_2(y_2) - \bar{W}_{p_2} \left[1 + I_2(y_2) \right] &= 0. \end{aligned} \tag{6.10}$$

The unknown deflections can be obtained combining Eq. (6.10) with the equation of motion of both rails (Eq. (6.2) for $i = 1$ and $i = 2$). The system of equations obtained is

$$\begin{pmatrix} \Omega & 0 & -(\mathrm{i}\omega c_F + k_F^*) & 0 \\ 0 & \Omega & 0 & -(\mathrm{i}\omega c_F + k_F^*) \\ I_1(y_1) & I_2(y_1) & -(1+I_1(y_1)) & -I_2(y_1) \\ I_1(y_2) & I_2(y_2) & -I_1(y_2) & -(1+I_1(y_2)) \end{pmatrix} \begin{pmatrix} \bar{W}_{r_1} \\ \bar{W}_{r_2} \\ \bar{W}_{p_1} \\ \bar{W}_{p_2} \end{pmatrix} = \begin{pmatrix} \bar{P}_1 \\ \bar{P}_2 \\ 0 \\ 0 \end{pmatrix}, \tag{6.11}$$

where

$$\Omega = E_r^* I_r k_x^4 - \rho_r S_r \omega^2 + \mathrm{i}\omega c_F + k_F^*.$$

The deflections of both rails in the wavenumber domain are directly obtained from Eq. (6.11).

The developed track-interior floor model can be used to study the coupling between both rails. This study is performed comparing two responses: One, the response of a rail to a harmonic point load applied on it. The other, the response of this rail to a harmonic point load applied on the other rail. Following the receptance definitions used during this work and considering that the rails are positioned at Lines 4 and 5 (see Fig 6.3), the previous receptances are defined as $\alpha_{44}^{\text{r-p}}$ and $\alpha_{45}^{\text{r-p}}$, respectively.

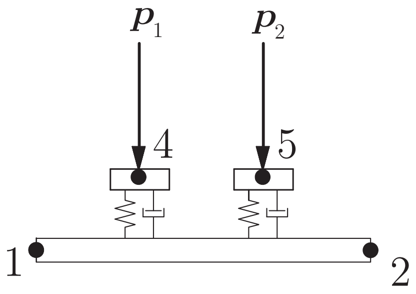

FIG. 6.3: Edge and rails positions for the general rail-plate coupling.

For both cases, it has been considered that the interior floor is simply supported at both edges, which is a good approximation when the tunnel is embedded in a hard ground. The mechanical parameters used for the rail and fasteners are presented in Table 6.1. The ones used for the interior floor model are those presented in Table 3.1. Hysteretic damping is considered for the fasteners.

The results have been calculated considering $N = 8192$ samples with a space resolution $\Delta x = 0.5$ m. Good precision has been obtained taking a truncation frequency $f_t = 4800$ Hz. To ensure that Eq. 6.11 is properly solved, an **LU** decomposition is performed. Results are presented from 1 to 200 Hz with a frequency resolution $\Delta f = 0.5$ Hz.

Fig. 6.4 presents the receptances $\alpha_{44}^{\text{r-p}}$ and $\alpha_{45}^{\text{r-p}}$ for two different cross-sections: $x_m = 0$ m and $x_m = 20$ m. The results in the first cross-section show a weak coupling between

Parameter	Value
S_r	$6.93 \cdot 10^{-3}$ m^2
I_r	$23.5 \cdot 10^{-6}$ m^4
E_r	$207 \cdot 10^9$ Pa
ρ_r	7850 kg m^{-3}
η_E	0.01
k_F^*	$192 \cdot 10^6$ N m^{-2}
η_F	0.2

TABLE 6.1: Mechanical parameters used in the rail and fasteners models. Results taken from [1].

the rails except in the region around 5 Hz, where their deflection is almost equal. At $x_m = 20$ m the rails deflections have a similar magnitude for almost all the considered frequencies.

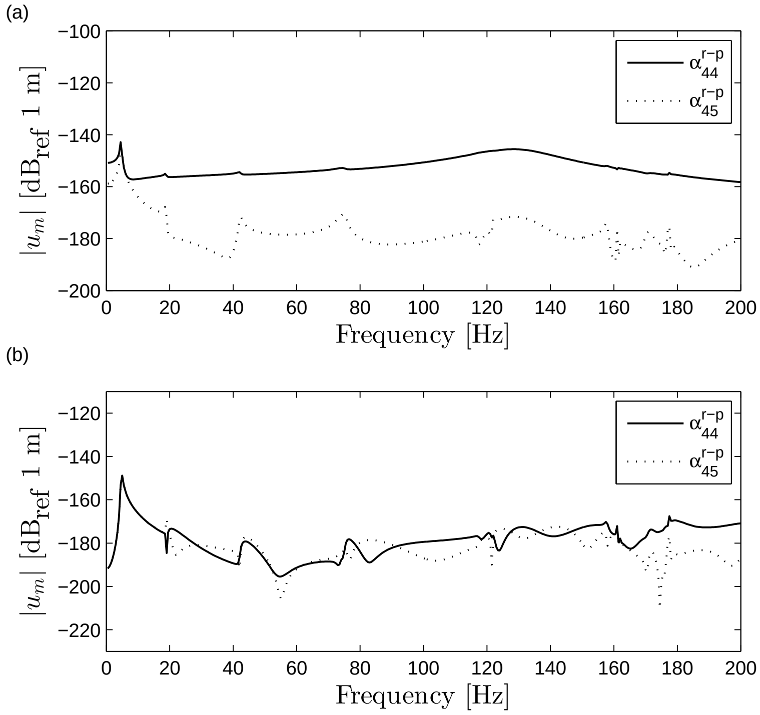

FIG. 6.4: Comparison between the receptances $\alpha_{44}^{\text{r-p}}$ and $\alpha_{45}^{\text{r-p}}$ of the track-interior floor system. The interior floor is assumed to be simply supported on a rigid wall. (a) Results at $x_m = 0$ m. (b) Results at $x_m = 20$ m.

In Fig. 6.5, the relative rail-interior floor deflection is calculated at the same cross-sections considered in the previous figure. From the results are $x_m = 0$ m, it becomes clear that deflections previously found around 5 Hz were mainly caused by the interior floor deflection. The relative deflection of rail 2 is now much lower than the one found in rail 1. It can be also seen that, the frequency response of $W_{r_1} - W_{p_1}$ at $x_m = 0$ m is the one expected of a single degree of freedom system. This can be justified noting that, at this cross-section, the direct response of the beam is equal to the one found for a lumped-mass system.

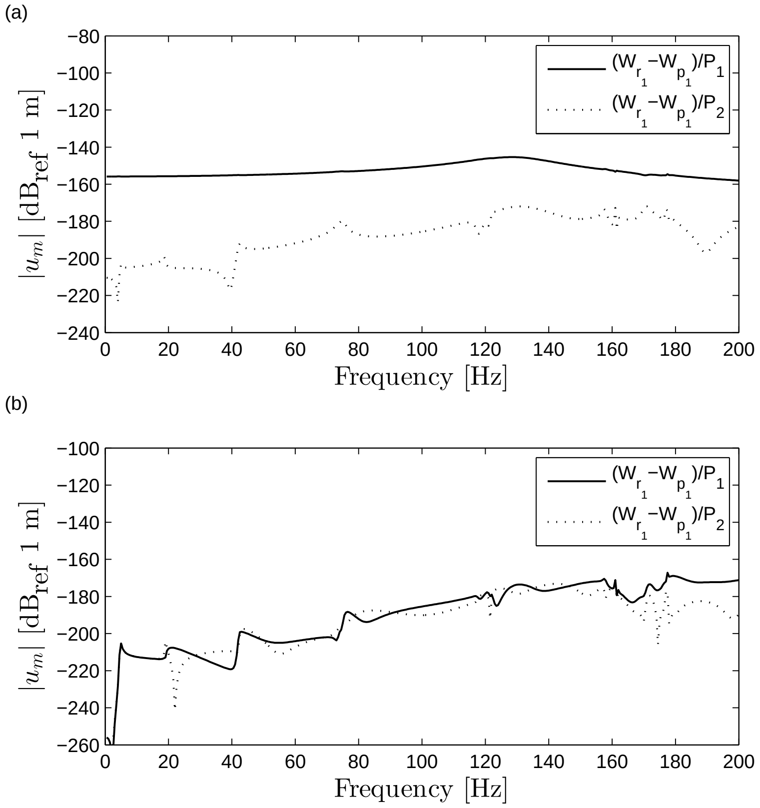

FIG. 6.5: Comparison between the relative rail-plate displacement $W_{r_1} - W_{p_1}$ for a harmonic load applied at rail 1 and at rail 2. The interior floor is assumed to be simply supported on a rigid wall. (a) Results at $x_m = 0$ m. (b) Results at $x_m = 20$ m.

6.2.2 Simplified rail-plate coupling

It is now assumed that when a load is applied on one of the rails the dynamic response of the other rail can be ignored. With this, the deflection of the interior floor becomes

$$\bar{W}(y_p) = \left[\bar{W}_{r_i} - \bar{W}_{p_i}\right] I_i(y_p). \tag{6.12}$$

As in the general case, considering $y_p = y_i$,

$$I_i(y_p)\bar{W}_{r_i} - \left[1 + I_i(y_p)\right] \bar{W}_{p_i} = 0, \tag{6.13}$$

which, combined with Eq. (6.2), gives the following system of equations

$$\begin{pmatrix} \Omega & -(\mathrm{i}\omega c_F + k_F^*) \\ I_i(y_i) & -\left[1 + I_i(y_i)\right] \end{pmatrix} \begin{pmatrix} \bar{W}_{r_i} \\ \bar{W}_{p_i} \end{pmatrix} = \begin{pmatrix} \bar{P}_i \\ 0 \end{pmatrix}. \tag{6.14}$$

Again, the deflection of the rail is directly obtained from Eq. (6.14) while the deflection of the interior floor is given by substituting the results of this equation into Eq. (6.12).

6.3 Track-tunnel-soil model

A complete track-tunnel-soil model for a double-deck tunnel is obtained coupling the superstructure-interior floor model with the PiP model. This coupling is again performed using the receptance method [19]. The free body diagrams of both systems, ignoring again the axial distribution of the loads, is presented in Fig. 6.6. The rails are fixed to the interior floor at Lines 4 and 5 while the edges are again positioned at Lines 1 and 2. For the case of the superstructure-interior floor system, external load $f_4^{\text{r-p}}$ and $f_5^{\text{r-p}}$ are considered on rails 1 and 2 and coupling loads $f_1^{\text{r-p}}$ and $f_2^{\text{r-p}}$ are considered on edges left and right.

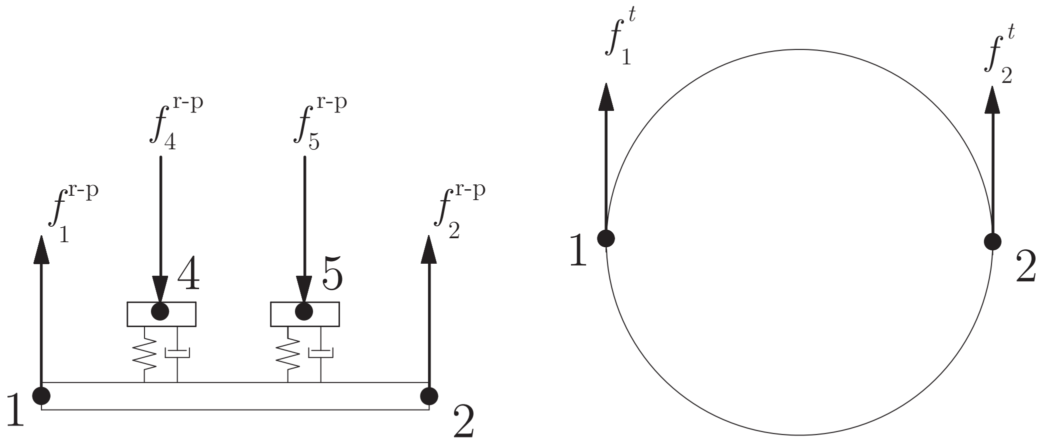

FIG. 6.6: (a) Free body diagram of the tunnel-soil system. (b) Free body diagram of the superstructure-interior floor system.

In the wavenumber-frequency domain the deflection of the interior floor is written as

$$\bar{W}_{p_i} = -\bar{\alpha}_{i1}^{\text{r-p}} \bar{F}_1^{\text{r-p}} - \bar{\alpha}_{i2}^{\text{r-p}} \bar{F}_2^{\text{r-p}} + \bar{\alpha}_{i4}^{\text{r-p}} \bar{F}_4^{\text{r-p}} + \bar{\alpha}_{i5}^{\text{r-p}} \bar{F}_5^{\text{r-p}}, \tag{6.15}$$

while the tunnel displacements are again given by Eq. (3.64).

The same type of coupling conditions considered in Section 3.5 are used for this case. They are expressed as

$$\begin{aligned} \bar{W}_p(0) &= -\bar{U}^t_{1\theta}, & \bar{F}^{\text{r-p}}_1 &= -\bar{F}^t_1, \\ \bar{W}_p(L_p) &= \bar{U}^t_{2\theta}, & \bar{F}^{\text{r-p}}_2 &= -\bar{F}^t_2. \end{aligned} \tag{6.16}$$

The coupling loads are obtained substituting Eqs. (6.15) and (3.64) into Eq. (6.16). The resulting system of equations is

$$\begin{pmatrix} -(\bar{\alpha}^{\text{r-p}}_{11} + \bar{\beta}_{1\theta,1\theta}) & -\bar{\alpha}^{\text{r-p}}_{12} + \bar{\beta}_{1\theta,2\theta} \\ -\bar{\alpha}^{\text{r-p}}_{21} + \bar{\beta}_{2\theta,1\theta} & -(\bar{\alpha}^{\text{r-p}}_{22} + \bar{\beta}_{2\theta,2\theta}) \end{pmatrix} \begin{pmatrix} \bar{F}^t_1 \\ \bar{F}^t_2 \end{pmatrix} = \begin{pmatrix} \bar{\alpha}^{\text{r-p}}_{14} \\ \bar{\alpha}^{\text{r-p}}_{24} \end{pmatrix} \bar{F}^{\text{r-p}}_4 + \begin{pmatrix} \bar{\alpha}^{\text{r-p}}_{15} \\ \bar{\alpha}^{\text{r-p}}_{25} \end{pmatrix} \bar{F}^{\text{r-p}}_5. \tag{6.17}$$

The receptances $\bar{\alpha}^{\text{r-p}}_{14}$, $\bar{\alpha}^{\text{r-p}}_{24}$, $\bar{\alpha}^{\text{r-p}}_{15}$ and $\bar{\alpha}^{\text{r-p}}_{25}$ are calculated using any of the coupling models proposed in Section 6.2. For the calculation of the receptances $\bar{\alpha}^{\text{r-p}}_{11}$, $\bar{\alpha}^{\text{r-p}}_{12}$, $\bar{\alpha}^{\text{r-p}}_{21}$ and $\bar{\alpha}^{\text{r-p}}_{22}$ an additional assumption is done. Because, in these receptances, both the excitation and the response points are points of the interior floor, they can be approximated to the interior floor ones, so

$$\begin{aligned} \bar{\alpha}^{\text{r-p}}_{11} &\approx \bar{\alpha}_{11}, & \bar{\alpha}^{\text{r-p}}_{12} &\approx \bar{\alpha}_{12}, \\ \bar{\alpha}^{\text{r-p}}_{21} &\approx \bar{\alpha}_{21}, & \bar{\alpha}^{\text{r-p}}_{22} &\approx \bar{\alpha}_{22}, \end{aligned} \tag{6.18}$$

which can be calculated using Eq. (3.41). The required PiP receptances are the ones defined in Eq. (3.67).

Once the coupling loads are obtained, the displacement field of the tunnel-soil system is obtained from Eq. (3.64). In the space domain, it can be expressed as

$$\mathbf{U}_i = \frac{1}{2\pi} \int_{-\infty}^{\infty} \left[\bar{\gamma}^c_{i4} \bar{F}^p_4 + \bar{\gamma}^c_{i5} \bar{F}^p_5 \right] \mathrm{e}^{-\mathrm{i}k_x x} \mathrm{d}k_x, \tag{6.19}$$

where $\bar{\gamma}^c_{i4}$ and $\bar{\gamma}^c_{i5}$ are the soil receptances to point loads applied at rails 1 and 2, respectively.

6.4 Chapter conclusions

This chapter has presented a track-tunnel-soil model for a double-deck tunnel embedded in a full space. A superstructure model has been proposed and coupled to the interior floor of the tunnel and the track-interior floor structure has been used to study the degree of coupling between both rails by comparing their response to a harmonic point load. It has been found that these coupling is very important at certain excitation frequencies.

The track-interior floor model has been finally coupled to the PiP model to obtain the complete track-tunnel-soil model.

Chapter 7

Conclusions and further work

This chapter presents a summary of the main conclusions drawn in this work and also proposes some recommendations for further research on the topic.

7.1 Conclusions

A three-dimensional analytical model of the dynamic behaviour of a double-deck circular tunnel embedded in a full-space has been developed. The model uses the receptance method to obtain the structure response combining the responses of its interior floor and of the tunnel-soil system separately. The interior floor has been modelled using the classical thin plate theory while the well-established PiP model has been used for the tunnel-soil dynamics. With this model, the prediction of vibration levels generated by underground trains using efficient models is extended to a new type of tunnel infrastructure. Up to date, their response could only be calculated using numerical models.

In addition to the analytical formulation of the model, its numerical computation has also been described in depth. Well-behaved expression for the problem eigenmodes have been obtained, adequate methods for solving bad-conditioned systems have been applied and efficient and accurate numerical integration techniques have been used. Also, convergence studies have been performed to ensure the correctness of the obtained results.

The obtained results clearly show the importance that has the dynamic response of the interior floor to the vibrations generated in the soil. For the same type of loading conditions, the vibration levels generated by the double-deck tunnel have been compared to those caused by a simple tunnel finding significant differences .

In order to justify the proposed coupling conditions, the interaction loads have been compared to those obtained in a weak coupled model. Clear differences have been found between both cases except when an unrealistically rigid ground has been considered. Therefore, the coupling assumptions have been found to be necessary for representing the interior floor-tunnel interactions.

A power flow calculation has been developed to perform a global comparison between the dynamic response of a double-deck tunnel and the one of a simple tunnel. A harmonic line load has been considered in both cases, allowing to formulate the problem in plane-strain conditions. In addition to the power flow radiated upwards by both tunnels, their radiation patterns have also been calculated for the most significative one-third octave bands. The obtained results show that the ratio between the power flow radiated upwards by both structures clearly depends on the excitation frequency considered. When this frequency is close to any of the transversal eigenfrequencies of the interior floor, the power radiated by the double-deck tunnel structure is several orders of magnitude higher than the one radiated by a simple tunnel. Also, the amount of energy directed vertically is much bigger for the double-deck tunnel case. In addition to the previous results, the effects of changing the load position and of modifying the flexural rigidity of the plate have been also studied. In the case of a stiff ground, a good approximation of the frequencies of maximum power flow has been proposed.

A comparison has been performed between the radiated energy by a simple tunnel and by a double-deck tunnel excited with a static moving load. It has been found that the frequency spectrums of the velocity of vibration and stress fields are clearly dependent of the considered load speed. The total energy radiated upwards by both tunnels have been determined for a wide range of speeds. The effect of the soil properties and of the tunnel interior floor have been identified by considering two different type of soils in addition to the two different types of tunnels. An important increase of the radiated energy has been found when the load speed is similar to the S-wave phase speed. Important differences between the energy radiated by both tunnels are only found for load speeds over 200 m s^{-1}, where the energy radiated by the double-deck tunnel has a much higher value than the one radiated by the simple tunnel. The response of a double-deck tunnel to a load moving at typical train speeds is very similar to the one obtained for a simple tunnel. From a local energy flow computation it has been concluded that the differences between the radiation patterns of both tunnels are not significantly affected by changes in the load speed or soil stiffness.

A superstructure model has been also coupled to the interior floor in order to obtain a complete superstructure-tunnel-soil model. The superstructure has been firstly coupled to the interior floor and the coupling between both rails has been studied. The track-interior floor model has been coupled to the PiP model to obtain the complete track-tunnel-soil model for a double-deck tunnel.

7.2 Further work recommendations

The point where the presented work finishes can also be the starting point for new interesting researches and improvements of the presented model. Some of them are mentioned here with recommendations that may be interesting to follow.

Geometry of the interior floor

The proposed model considers the interior floor as an infinite thin plate of constant thickness but, in real cases, double-deck tunnels won't necessarily obey this assumption (see Fig. 1.1). However, an equivalent thin plate model can be considered for most of the interior floor structures, allowing to use the described model once the former is obtained. Another consideration that can be studied is the validity of the contact assumption between the interior floor and the tunnel structure. The assumed hypothesis can be improved by considering that the coupling loads obtained are not point loads applied on the tunnel but a have a certain angular distribution along the tunnel wall. It is expected that, the wider the interior floor-tunnel wall contact surface is the worse the point-contact hypothesis becomes.

Coupling conditions

The coupling conditions between the interior floor and the tunnel assumed in this work are equivalent to consider the interior floor simply supported on the walls of the tunnel. A pinned connection between the interior floor and the tunnel wall is a realistic hypothesis when the interior floor is a separate precast slab structure supported on the tunnel walls. For a different construction method of the double-deck tunnel structure, the real interaction between these parts may require to consider more complex coupling conditions. One type of improvement would be to add moments or/and inplane loads in the coupling assumptions and compare their effect on the soil response. Better knowledge on the real interaction between both systems could also be gained by measuring the response of a double-deck tunnel to an applied known load.

Soil model

In the present work, the double-deck tunnel is considered to be deeply buried in a homogeneous infinite media. Under this assumption, the soil can be considered as a full-space and surface results could be obtained by adding 6 dB to the former [93]. In a shallow tunnel case or in the case of considering a layered half-space, other formulations of the soil must be considered [92, 94]. The interaction of a double-deck tunnel structure with this new soil models may predict new dynamic responses that should be properly studied.

Experimental validation

A complete vehicle-superstructure-tunnel model will be obtained if a vehicle model is coupled to the double-deck tunnel model proposed in this work. This coupled model can be then validated by comparing the results predicted with experimental results from a train passage.

Appendix A

Fourier transforms and series

This appendix presents the definitions of the Fourier transforms and series used in this work and a brief description of how the defined Fourier antitransforms are numerically integrated.

A.1 Fourier transform

As Grundmann and Trommer discussed [108], when the Integral Transform Method can be applied to a problem, not only efficient solutions are obtained but a deeper understanding of the physical nature of the problem is gained. This is the case of the dynamical system considered where, with the application of a double Fourier transform, the problem is transformed from the space-time domain to the wavenumber-frequency domain and its solution can be easily obtained. Once the transformed solution is known, the proper Fourier antitransform allows to obtain the solution of the problem in the original domain.

In the next subsections, the considered definition of these Fourier transforms is presented together with its numerical treatment.

A.1.1 Definitions

A dynamical magnitude $f(x,t)$ defined in the space-time domain is transformed to the space-frequency domain applying the following Fourier transform

$$F(x,\omega)=\int_{-\infty}^{\infty} f(x,t)\mathrm{e}^{-\mathrm{i}\omega t}\mathrm{d}t. \tag{A.1}$$

The corresponding Fourier antitransform, which transforms $F(x,\omega)$ back to the space-time domain is given by

$$f(x,t)=\frac{1}{2\pi}\int_{-\infty}^{\infty}F(x,\omega)\mathrm{e}^{\mathrm{i}\omega t}\mathrm{d}\omega. \tag{A.2}$$

In the same way, a dynamical magnitude $F(x,\omega)$ defined in the space-frequency domain is transformed to the wavenumber-frequency domain applying the following Fourier transform

$$\bar{F}(k_x,\omega)=\int_{-\infty}^{\infty}F(x,\omega)\mathrm{e}^{\mathrm{i}k_x x}\mathrm{d}x. \tag{A.3}$$

The corresponding Fourier antitransform, which transforms $\bar{F}(k_x,\omega)$ back to the space-frequency domain is given by

$$F(x,\omega)=\frac{1}{2\pi}\int_{-\infty}^{\infty}\bar{F}(k_x,\omega)\mathrm{e}^{-\mathrm{i}k_x x}\mathrm{d}k_x. \tag{A.4}$$

When these integral transforms are applied to the system of partial differential equations that describe the dynamics of the problem, this system is reduced to one composed of ordinary differential equation or algebraic equations. The same set of equations are obtained if, instead of applying the previous Fourier transforms, the following type of solution is considered

$$f(x,t,\dots)=F(x,\dots)\mathrm{e}^{\mathrm{i}\omega t}=\bar{F}(\dots)\mathrm{e}^{\mathrm{i}(\omega t-k_x x)}. \tag{A.5}$$

In the presented work, a combination of both methods is usually applied. Harmonic motion is assumed and Eq. (A.3) is applied to transform the problem to the wavenumber domain.

A.1.2 Numerical integration: The Discrete Fourier Transform (DFT)

Except for a small set of cases where closed-form solutions can be obtained, the integrals of Eqs. (A.2) and (A.4) can only be solved using numerical integration methods. The chosen method to perform this will depend on the type of solution desired. Regardless of the method used, two parameters should be properly defined in any numerical integration: The integration limits and the integrand sampling.

A necessary condition to obtain a precise result of the Fourier antitransform is that the chosen inferior ($\mathrm{L_{inf}}$) and superior ($\mathrm{L_{sup}}$) integration limits ensure that

$$\bar{F}(k_x)\approx 0,\qquad k_x\in(-\infty,\mathrm{L_{inf}})\cup(\mathrm{L_{sup}},\infty). \tag{A.6}$$

where the condition has been defined for Eq. A.4 but an analogous condition is required in A.2.

Another requirement for the obtention of precise results is that the integrand has to be correctly sampled, specially in the case when the function contains sharp peaks. If the performed sampling is not smooth enough, the numerical integration won't be a correct approximation of the analytical one.

Considering again Eq. (A.4), if the results for only one position of the x-coordinate are desired, the numerical integration of this highly oscillating function can be performed using, for example, the Filon's method [109]. However, when results in a considerable number of positions is required, the use of the Discrete Fourier Transform (DFT) is much more efficient.

The DFT defined in this work is the one used by the numerical software MATLAB. The direct and inverse DFT are given by

$$F(q) = \mathrm{DFT}[f(p)] = \sum_{p=1}^{N} f(p)\mathrm{e}^{\frac{-2\pi\mathrm{i}(p-1)(q-1)}{N}}, \qquad q = 1, ..., N \tag{A.7}$$

and

$$f(p) = \mathrm{IDFT}[F(q)] = \frac{1}{N}\sum_{q=1}^{N} F(q)\mathrm{e}^{\frac{2\pi\mathrm{i}(p-1)(q-1)}{N}}, \qquad p = 1, ..., N, \tag{A.8}$$

where N is the number of samples.

The discrete expression of Eq. (A.4) can be written as

$$F(x_p) = \sum_{q=-N/2}^{N/2-1} \bar{F}_q \mathrm{e}^{-\mathrm{i}q\Delta k_x p\Delta x}\Delta k_x. \tag{A.9}$$

where the frequency dependance has been omitted and a wavenumber sampling of the following form has been considered

$$k_q = \left(q - \frac{N}{2}\right)\Delta k_x, \qquad q = 0, ..., N-1. \tag{A.10}$$

If the function samples are properly reordered and using that

$$\Delta x = \frac{2\pi}{N\Delta k_x}, \tag{A.11}$$

it can be seen that, Eq. (A.4) is obtained using the Inverse DFT and multiplying the result by Δx^{-1}. An analogous conclusion is found for Eq. (A.3), which can be calculated using the DFT and multiplying the result by Δx. Analogous results are found if Eq. (A.2) is considered.

The values $N\Delta x$ and $N\Delta k_x$ are the lengths of the space and wavenumber domains that have been sampled so farther information is ignored in the calculations. Also, the chosen wavenumber sampling (and its corresponding space one) have been defined considering an even number of samples. This is done this way because the DFT is computed using Fast Fourier Transform (FFT) algorithm [110], which is more efficient if N is a power of 2. In order to improve the efficiency of the FFT for the cases where the integrands present a smooth decay, some authors have proposed the use of a logarithmic change of variable [111]. Algorithms for performing a FFT with unequally spaced data have also been proposed [112, 113].

A.2 Fourier series

A function $f(t)$ is a periodic function if $f(t) = f(t+T)$, being T its period. Periodic functions can be decomposed as an infinite sum of harmonic functions as follows

$$f(t) = a_0 + \sum_{n=1}^{\infty} \left[a_n \cos\left(\frac{2\pi nt}{T}\right) + b_n \sin\left(\frac{2\pi nt}{T}\right) \right], \tag{A.12}$$

where

$$\begin{aligned} a_0 &= \frac{1}{T}\int_0^T f(t)\mathrm{d}t, \\ a_n &= \frac{2}{T}\int_0^T f(t)\cos\left(\frac{2\pi nt}{T}\right)\mathrm{d}t, \\ b_n &= \frac{2}{T}\int_0^T f(t)\sin\left(\frac{2\pi nt}{T}\right)\mathrm{d}t. \end{aligned} \tag{A.13}$$

Of particular interest during this text (see Section D.4) is the Fourier series decomposition of an angular Dirac's delta distribution. In this case $T = 2\pi$ and

$$\delta(\theta - \theta_i) = \frac{1}{2\pi} + \frac{1}{\pi}\sum_{n=1}^{\infty} \big(\cos(n\theta)\cos(n\theta_i) + \sin(n\theta)\sin(n\theta_i)\big), \tag{A.14}$$

being θ_i the position where the load is applied. When the delta is placed at $\theta_i = 0$ or $\theta_i = \pi$, two cases considered in Section 3.4.2, the previous expression become

$$\begin{aligned} \delta(\theta) &= \frac{1}{2\pi} + \frac{1}{\pi}\sum_{n=1}^{\infty}\cos(n\theta), \\ \delta(\theta-\pi) &= \frac{1}{2\pi} + \frac{1}{\pi}\sum_{n=1}^{\infty}(-1)^n\cos(n\theta). \end{aligned} \tag{A.15}$$

Appendix B

Thin shell theory

This appendix presents a brief review of the thin shell theory results used during this work. The initial section defines the general thin shell equations while the following sections detail the results of interest for the particular cases of a thin plate and of a thin circular cylindrical shell.

B.1 General thin shell equations

The general equations of motion of a thin shell [19, 30] can be written as

$$
\begin{aligned}
L_1\{u_1,u_2,u_3\} - \rho_s h_s \frac{\partial^2 u_1}{\partial t^2} &= -q_1, \\
L_2\{u_1,u_2,u_3\} - \rho_s h_s \frac{\partial^2 u_2}{\partial t^2} &= -q_2, \\
L_3\{u_1,u_2,u_3\} - \rho_s h_s \frac{\partial^2 u_3}{\partial t^2} &= -\left[q_3 + \frac{1}{A_1 A_2}\left\{\frac{\partial(M_1 A_2)}{\partial \alpha_1} + \frac{\partial(M_2 A_1)}{\partial \alpha_2}\right\}\right],
\end{aligned}
\tag{B.1}
$$

where u_i is the displacement in the curvilinear surface coordinate α_i, ρ_s is the density of the shell, h_s is its thickness and $A_i = \partial^2 \vec{r}/\partial \alpha_i^2$ are the fundamental form or Lamé parameters. The considered positive directions of the external loads q_i, moments M_i and coordinates α_i are shown in Fig. B.1. Two particular cases of thin shells are used in this work, a thin strip plate and a thin circular cylindrical shell. They are detailed in the following sections.

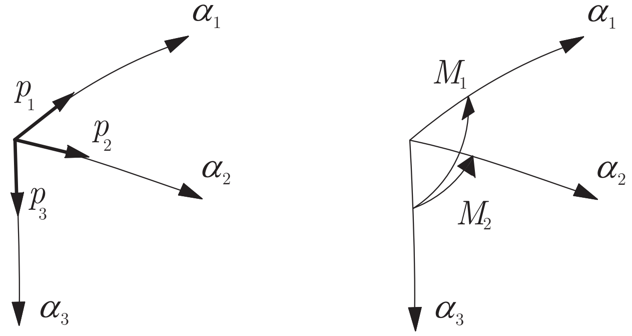

FIG. B.1: Positive signs considered for the loads and moments applied on the shell.

B.2 Thin plate

A thin plate can be considered as a thin shell with no curvature. In this case

$$\begin{array}{rclrclrcl} \alpha_1 & = & x, & \alpha_2 & = & y, & u_3 & = & w, \\ A_1 = A_2 & = & 1, & M_1 & = & M_y, & M_2 & = & M_x \end{array} \tag{B.2}$$

and the equation of motion for the transverse displacements w takes the form

$$L_3^{\mathrm{tp}}\{w\} - \rho_s h_s \frac{\partial^2 w}{\partial t^2} = -\left[q_3 + \left\{ \frac{\partial M_y}{\partial x} + \frac{\partial M_x}{\partial y} \right\} \right], \tag{B.3}$$

where $L_3^{\mathrm{tp}} = -D_p \nabla^4$.

The bending moments M_x and M_y are given by

$$M_x = -D_p \left(\frac{\partial^2 w_p}{\partial x^2} + \nu_p \frac{\partial^2 w_p}{\partial y^2} \right), \quad M_y = -D_p \left(\frac{\partial^2 w_p}{\partial y^2} + \nu_p \frac{\partial^2 w_p}{\partial x^2} \right). \tag{B.4}$$

The twisting moment M_{xy} can be written as

$$M_{xy} = -D_p(1-\nu_p)\frac{\partial^2 w_p}{\partial x \partial y}. \tag{B.5}$$

The transverse shearing forces Q_x and Q_y are given by

$$Q_x = -D_p \left(\frac{\partial^3 w_p}{\partial x^3} + \frac{\partial^3 w_p}{\partial x \partial^2 y} \right), \quad Q_y = -D_p \left(\frac{\partial^3 w_p}{\partial y \partial^2 x} + \frac{\partial^3 w_p}{\partial y^3} \right). \tag{B.6}$$

Finally, the Kelvin-Kirchoff edge reactions V_x and V_y can be obtained from the previous expressions

$$V_x = Q_x + \frac{\partial M_{xy}}{\partial y}, \quad V_y = Q_y + \frac{\partial M_{xy}}{\partial x}. \tag{B.7}$$

Three types of basic boundary conditions are usually considered in the edges of a thin plate: Simply supported (SS), clamped (C) and free (F) edges. These boundary conditions will be defined considering the edge $y = y_e$, but analogous expression could be obtained for the edge $x = x_e$.

In a SS edge, both the deflection and the bending moment per unit of length M_y of the plate are zero. In terms of the deflection this can be written as

$$w_p\bigg|_{y=y_e} = 0, \qquad \frac{\partial^2 w_p}{\partial y^2} + \nu_p \frac{\partial^2 w_p}{\partial x^2}\bigg|_{y=y_e} = 0. \tag{B.8}$$

For a clamped edge, both the deflection and its slope vanish so:

$$w_p\bigg|_{y=y_e} = 0, \qquad \frac{\partial w_p}{\partial y}\bigg|_{y=y_e} = 0. \tag{B.9}$$

Finally, in a free boundary of the plate, the bending moment M_y and the Kelvin-Kirchoff edge reaction V_y are zero. In terms of the deflection

$$\frac{\partial^3 w_p}{\partial y^3} + (2-\nu_p)\frac{\partial^3 w_p}{\partial y \partial x^2}\bigg|_{y=y_e} = 0, \qquad \frac{\partial^2 w_p}{\partial y^2} + \nu_p \frac{\partial^2 w_p}{\partial x^2}\bigg|_{y=y_e} = 0. \tag{B.10}$$

B.3 Thin circular cylindrical shell

Several theories have been proposed to model the dynamics of a thin cylindrical shell [25–30]. Among them, the Flügge equations of a thin circular cylindrical shell [28] are the ones presented here. In this case

$$\begin{array}{llllllll}
\alpha_1 = x, & \alpha_2 = \theta, & & \\
u_1 = u_x, & u_2 = u_\theta, & u_3 = u_r, & \\
q_1 = q_x, & q_2 = q_\theta, & q_3 = q_r, & \\
A_1 = 1, & A_2 = r_s, & M_1 = M_\theta, & M_2 = M_x,
\end{array} \tag{B.11}$$

where r_s is the radius of the shell and Eq. (B.1) is takes the form

$$\begin{aligned}
&r_s\frac{\partial^2 u_x}{\partial x^2} + \frac{1-\nu_s}{2r_s}\frac{\partial^2 u_x}{\partial \theta^2} + \frac{1+\nu_s}{2}\frac{\partial^2 u_\theta}{\partial x \partial \theta} - \rho_s r_s \frac{1-\nu_s^2}{E_s}\frac{\partial^2 u_x}{\partial t^2} - \\
&\nu_s \frac{\partial u_r}{\partial x}\frac{h_s^2}{12}\left[\frac{(1-\nu_s)}{2r_s^3}\frac{\partial^2 u_x}{\partial \theta^2} + \frac{\partial^3 u_r}{\partial x^3} - \frac{(1-\nu_s)}{2r_s^2}\frac{\partial^3 u_r}{\partial x \partial \theta^2}\right] = -r_s\frac{1-\nu_s^2}{E_s h_s}q_x,
\end{aligned} \tag{B.12}$$

$$\begin{aligned}&\frac{1+\nu_s}{2}\frac{\partial^2 u_x}{\partial x\partial\theta} + r_s\frac{1-\nu_s}{2}\frac{\partial^2 u_\theta}{\partial x^2} + \frac{1}{r_s}\frac{\partial^2 u_\theta}{\partial\theta^2} - \frac{1}{r_s}\frac{\partial u_r}{\partial\theta} - \rho_s r_s\frac{1-\nu_s^2}{E_s}\frac{\partial^2 u_\theta}{\partial t^2} + \\ &\frac{h_s^2}{12}\left[\frac{3(1-\nu_s)}{2r_s}\frac{\partial^2 u_\theta}{\partial x^2} + \frac{(3-\nu_s)}{2r_s}\frac{\partial^3 u_r}{\partial x^2\partial\theta}\right] = -r_s\frac{1-\nu^2}{E_s h_s}q_\theta,\end{aligned} \tag{B.13}$$

$$\begin{aligned}&\nu\frac{\partial u_x}{\partial x} + \frac{1}{r_s}\frac{\partial u_\theta}{\partial\theta} - \frac{u_r}{r_s} - \rho_s r_s\frac{1-\nu_s^2}{E_s}\frac{\partial^2 u_r}{\partial t^2} + \\ &\frac{h_s^2}{12}\left[r_s\frac{\partial^4 u_r}{\partial x^4} + \frac{2}{r_s}\frac{\partial^4 u_r}{\partial x^2\partial\theta^2} + \frac{1}{r_s^3}\frac{\partial^4 u_r}{\partial\theta^4} + \frac{\partial^3 u_x^t}{\partial x^3} - \frac{(1-\nu_s)}{2r_s^2}\frac{\partial^3 u_x}{\partial x\partial\theta^2}\right] + \\ &\frac{h_s^2}{12}\left[\frac{(3-\nu_s)}{2r_s}\frac{\partial^3 u_\theta}{\partial x^2\partial\theta} + \frac{u_r}{r_s^3} + \frac{2}{r_s^3}\frac{\partial^2 u_r}{\partial\theta^2}\right] = \\ &-r_s\frac{1-\nu^2}{E_s h_s}\left(q_r + \frac{1}{r_s}\left[\frac{\partial(M_\theta r_s)}{\partial x} + \frac{\partial M_x}{\partial\theta}\right]\right).\end{aligned} \tag{B.14}$$

where ρ_s is the density of the shell, h_s is its thickness, E_s is its Young modulus and ν_s is its Poisson's ratio. The cylindrical system of coordinates used and the positive directions of the displacement and stress fields can be seen in Fig. B.2.

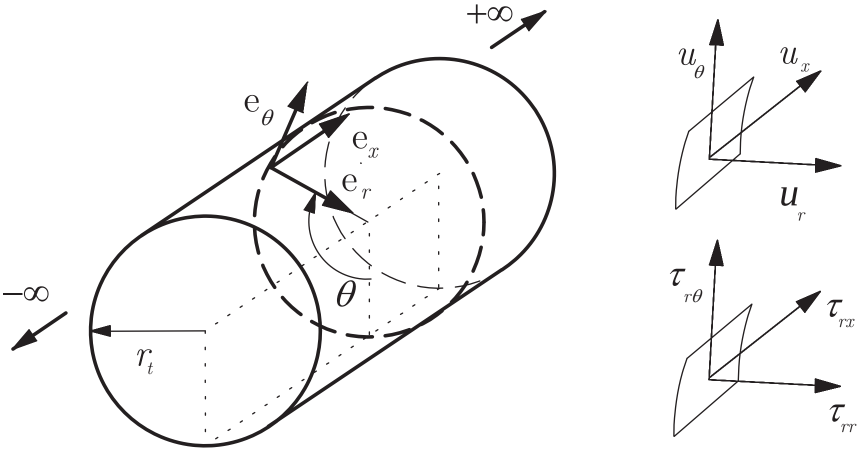

FIG. B.2: Thin circular cylindrical shell model used for the tunnel. Positive displacements and stresses are also defined.

Appendix C

Linear Elasticity

This appendix begins with a brief review of the linear elastic equations in cylindrical coordinates, which are used in Appendix D to represent the soil behaviour. Some important relations between the most used elastic constants and two different types of damping formulations are also presented.

C.1 Elasticity equations in cylindrical coordiantes

When small strains are considered, the displacement of an isotropic elastic media obeys the Navier's equation [114]

$$(\lambda_s + \mu_s)\nabla\nabla \cdot \mathbf{u} + \mu_s \nabla^2 \mathbf{u} = \rho_s \frac{\partial^2}{\partial t^2}\mathbf{u}, \tag{C.1}$$

where λ_s is the first Lamé constant, μ_s is the shear modulus or second Lamé constant, ρ_s is the soil density and where gravity forces haven't been considered.

Eq. (C.1) can be solved applying the Helmholz decomposition, which states that

$$\mathbf{u} = \nabla\phi + \nabla \times \boldsymbol{\psi}, \qquad \nabla \times \boldsymbol{\psi} = \mathbf{F}, \tag{C.2}$$

where $\mathbf{F}$ is an arbitrary function. Using Eq. (C.2) in Eq. (C.1), the following scalar and a vectorial wave equations are obtained

$$\nabla^2\phi = \frac{1}{c_P^2}\frac{\partial^2\phi}{\partial t^2}, \qquad \nabla^2\boldsymbol{\psi} = \frac{1}{c_S^2}\frac{\partial^2\boldsymbol{\psi}}{\partial t^2}, \tag{C.3}$$

where ϕ and $\boldsymbol{\psi}$ are the scalar and vectorial potentials and where

$$c_P = \sqrt{\frac{\lambda_s + 2\mu_s}{\rho_s}}, \qquad c_S = \sqrt{\frac{\mu_s}{\rho_s}} \tag{C.4}$$

are the phase speeds of the P-wave and S-wave respectively.

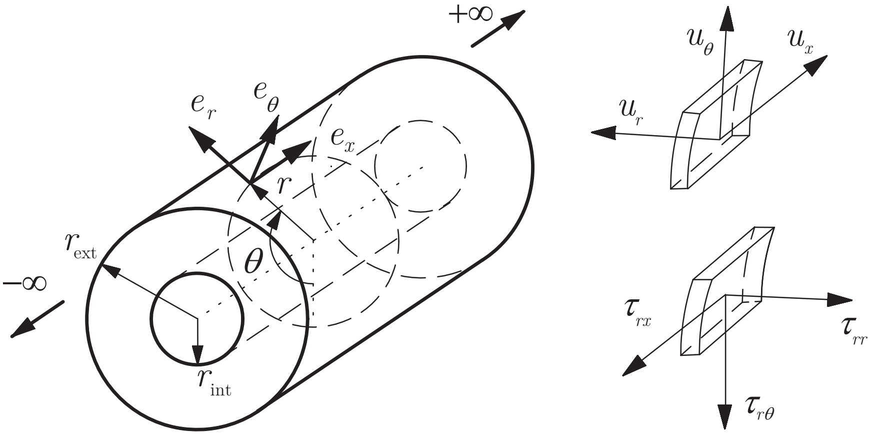

Fig. C.1: Thick cylindrical shell model used for the soil (and the tunnel). Positive displacements and stresses are also defined.

If a cylindrical system of coordinates of the form presented in Fig. C.1 is considered, the displacement and stress fields and the vectorial potential components are given by

$$\mathbf{u} = \begin{pmatrix} u_r \\ u_\theta \\ u_x \end{pmatrix}, \quad \boldsymbol{\tau} = \begin{pmatrix} \tau_{rr} \\ \tau_{r\theta} \\ \tau_{rx} \end{pmatrix}, \quad \boldsymbol{\psi} = \begin{pmatrix} \psi_r \\ \psi_\theta \\ \psi_x \end{pmatrix}, \tag{C.5}$$

In this system of coordinates, Eq. (C.2) becomes

$$\begin{aligned} u_r &= \frac{\partial \phi}{\partial r} + \frac{1}{r}\frac{\partial \psi_x}{\partial \theta} - \frac{\partial \psi_\theta}{\partial x}, \\ u_\theta &= \frac{1}{r}\frac{\partial \phi}{\partial \theta} + \frac{\partial \psi_r}{\partial x} - \frac{\partial \psi_x}{\partial x}, \\ u_x &= \frac{\partial \phi}{\partial x} + \frac{1}{r}\frac{\partial (r\psi_\theta)}{\partial r} - \frac{1}{r}\frac{\partial \psi_r}{\partial \theta}. \end{aligned} \tag{C.6}$$

The relation between the stresses and the potentials can be obtained substituting Eq (C.6) into the following equation

$$\begin{aligned}
\tau_{rr} &= (\lambda_s + 2\mu_s)\frac{\partial u_r}{\partial r} + \lambda_s\left(\frac{1}{r}\frac{\partial u_\theta}{\partial \theta} + \frac{u_r}{r}\right) + \lambda_s\frac{\partial u_x}{\partial x}, \\
\tau_{r\theta} &= \mu_s\left(\frac{1}{r}\frac{\partial u_r}{\partial \theta} + \frac{\partial u_\theta}{\partial r} - \frac{u_\theta}{r}\right), \\
\tau_{rx} &= \mu_s\left(\frac{\partial u_r}{\partial x} + \frac{\partial u_x}{\partial r}\right).
\end{aligned} \tag{C.7}$$

The positive directions of both fields have also been presented in Fig. C.1.

C.2 Elastic constants

An isotropic linear elastic media is completely defined by two independent elastic constants. In the previous equations, the two Lamé parameters have been used, but other elastic constants such as the Young modulus E_s, the Poisson ratio ν_s, the shear modulus G_s and the bulk modulus K_s can also be used. Some relation between them are presented here.

Knowing the couple (E_s, ν_s), the Lamé parameters can be obtained using

$$\lambda_s = \frac{E_s\nu_s}{(1+\nu_s)(1-2\nu_s)}, \qquad \mu_s = \frac{E_s}{2(1+\nu_s)}. \tag{C.8}$$

Knowing the Lamé parameters, the couple (E_s, ν_s) can be obtained from

$$E_s = \frac{\mu_s(3\lambda_s + 2\mu_s)}{\lambda_s + \mu_s} \qquad \nu_s = \frac{\lambda_s}{2(\lambda_s + \mu_s)}. \tag{C.9}$$

Finally, the bulk modulus can also be obtained from

$$K_s = \lambda_s + \frac{2\mu_s}{3} = \frac{E_s}{3(1-2\nu_s)}. \tag{C.10}$$

C.3 Material damping

To take into account the energy loss caused by microstructural friction mechanisms, the elastic model must be replaced by a viscoelastic one. A well-established procedure is to assume the validity of the correspondence principle [59] which states that the viscoelastic case can be obtained from the elastic one by considering complex valued elastic constants. Two damping theories are presented in the following sections. The former is the one used in this work.

C.3.1 Hysteretic damping

A typical definition of this type of damping considers complex valued Lamé parameters (λ_s^* and μ_s^*), which are defined as follows

$$\lambda_s^* + 2\mu_s^* = (\lambda_s + 2\mu_s)(1 + 2\mathrm{i}D_P\mathrm{sgn}(\omega)), \qquad \mu_s^* = \mu_s(1 + 2\mathrm{i}D_S\mathrm{sgn}(\omega)), \tag{C.11}$$

where D_P and D_S are the hysteretic damping ratios for P and S waves and where sgn refers to the sign function.

Other definition typically used are

$$K_s^* = K_s(1 + \mathrm{i}\eta_K), \quad \mu_s^* = \mu_s(1 + \mathrm{i}\eta_\mu), \quad E_s^* = E_s(1 + \mathrm{i}\eta_E), \tag{C.12}$$

where η_K, η_μ and η_E are the loss factors associated to this parameters.

In this work, the interior floor and tunnel hysteretic damping are defined using Eq. (C.12) while the soil hysteretic damping is defined using Eq. (C.12).

C.3.2 Rayleigh damping

The Rayleigh damping model considers that

$$E_s^* = E_s(1 + \mathrm{i}\omega\beta_R), \qquad \rho_s^* = \rho_s\left(1 + \frac{\alpha_R}{\mathrm{i}\omega}\right), \tag{C.13}$$

where ω is frequency and α_R and β_R are two independent constant. This type of damping can also be applied at the Lamé parameters as follows

$$\lambda_s^* = \lambda_s(1 + \mathrm{i}\omega\beta_R), \qquad \mu_s^* = \mu_s(1 + \mathrm{i}\omega\beta_R). \tag{C.14}$$

Appendix D

The Pipe-in-Pipe model

This appendix presents a brief review of the different formulations of the Pipe-in-Pipe (PiP) model, presented by Forrest and Hunt [17] as an analytical model for a deep buried cylindrical tunnel. The initial formulation has been later extended introducing a second load formulation [88], modifying the considered tunnel model and assuming plane-strain conditions [102].

The model considers the tunnel as a thin cylindrical infinite shell and the soil as a homogeneous and isotropic infinite elastic media with a cylindrical cavity in it. The coupling of both systems is performed in the wavenumber-frequency domain.

D.1 Thin cylindrical shell equations

Among the existing thin shell theories, Forrest and Hunt [17] considered ones proposed by Flügge's [28] (Eqs. (B.12) to (B.14)) to describe the dynamical behaviour of the tunnel. Considering harmonic motion and Eq. (A.4), the displacement field and the applied loads can be written as

$$\begin{aligned} \mathbf{u}^t &= \frac{1}{2\pi}\int_{-\infty}^{\infty} \bar{\mathbf{U}}^t \mathrm{e}^{\mathrm{i}(\omega t - k_x x)} \mathrm{d}k_x, \\ \mathbf{q} &= \frac{1}{2\pi}\int_{-\infty}^{\infty} \bar{\mathbf{Q}}^t \mathrm{e}^{\mathrm{i}(\omega t - k_x x)} \mathrm{d}k_x, \end{aligned} \tag{D.1}$$

where, performing a Fourier series decomposition, $\bar{\mathbf{U}}^t$ and $\bar{\mathbf{Q}}$ are written as

$$\begin{aligned} \bar{\mathbf{U}}^t &= \sum_{n=0}^{\infty} \left[\mathbf{S}^s \bar{\mathbf{U}}_n^s + \mathbf{S}^a \bar{\mathbf{U}}_n^a\right], \\ \bar{\mathbf{Q}} &= \sum_{n=0}^{\infty} \left[\mathbf{S}^s \bar{\mathbf{Q}}_n^s + \mathbf{S}^a \bar{\mathbf{Q}}_n^a\right], \end{aligned} \tag{D.2}$$

where

$$\mathbf{S}^s = \begin{pmatrix} \cos n\theta & 0 & 0 \\ 0 & \sin n\theta & 0 \\ 0 & 0 & \cos n\theta \end{pmatrix}, \quad \mathbf{S}^a = \begin{pmatrix} \sin n\theta & 0 & 0 \\ 0 & \cos n\theta & 0 \\ 0 & 0 & \sin n\theta \end{pmatrix}. \tag{D.3}$$

Transforming Eqs. (B.12) to (B.14)) to the wavenumber domain and substituting Eq. (D.2) into them, the following equations are obtained

$$\begin{aligned} \mathbf{A}^s \bar{\mathbf{U}}_n^{t,s} &= \frac{-r_t(1-\nu_t^2)}{E_t h_t} \bar{\mathbf{Q}}_n^s, \\ \mathbf{A}^a \bar{\mathbf{U}}_n^{t,a} &= \frac{-r_t(1-\nu_t^2)}{E_t h_t} \bar{\mathbf{Q}}_n^a. \end{aligned} \tag{D.4}$$

These two uncoupled sets of algebraic equations relate the n-th coefficient of the applied load decomposition with the n-th term of displacements decomposition. If one of them is known, the other is univocally obtained. The first set of equations corresponds to the symmetric loading distribution [17] while the second corresponds to the antisymmetric one [92]. The superscripts s and a are used here to identify each case. To simplify the notation, when an equation is valid for both formulations, these superscripts will be omitted.

The matrix $\mathbf{A}$ is defined as

$$\mathbf{A} = \begin{pmatrix} a_{12} & a_{14} & a_{16} \\ a_{22} & a_{24} & a_{26} \\ a_{32} & a_{34} & a_{36} \end{pmatrix}, \tag{D.5}$$

where

$$\begin{aligned} a_{11}^s &= \frac{\rho_t r_t (1-\nu_t^2)\omega^2}{E_t} - r_t k_x^2 - \frac{(1-\nu_t)n^2}{2r_t}\left(1 + \frac{h_t^2}{12 r_t^2}\right), \\ a_{12}^s &= \frac{(1+\nu_t)\mathrm{i}k_x n}{2}, \\ a_{13}^s &= -\nu_t \mathrm{i}k_x - \frac{h_t^2 \mathrm{i}k_x^3}{12} + \frac{h^2(1-\nu_t)\mathrm{i}k_x n^2}{24 r_t^2}, \end{aligned}$$

$$
\begin{aligned}
a^s_{21} &= \frac{-(1+\nu_t)\mathrm{i}k_x n}{2} = -a^s_{12},\\
a^s_{22} &= \frac{\rho_t r_t(1-\nu_t^2)\omega^2}{E_t} - \frac{r_t(1-\nu_t)k_x^2}{2}\left(1+\frac{h_t^2}{4r_t^2}\right) - \frac{n^2}{r_t},\\
a^s_{23} &= \frac{n}{r_t} + \frac{h_t^2(3-\nu_t)k_x^2 n}{24 r_t},\\
a^s_{31} &= \nu_t \mathrm{i}k_x + \frac{h_t^2 \mathrm{i}k_x^3}{12} - \frac{h^2(1-\nu_t)\mathrm{i}k_x n^2}{24 r_t^2} = -a^s_{13},\\
a^s_{32} &= \frac{n}{r_t} + \frac{h_t^2(3-\nu_t)k_x^2 n}{24 r_t} = a^s_{23},\\
a^s_{33} &= \frac{\rho_t r_t(1-\nu_t^2)\omega^2}{E_t} - \frac{h_t^2}{12}\left(r_t k_x^4 + \frac{2k_x^2 n^2}{r_t} + \frac{n^4}{r_t^3}\right) - \frac{1}{r_t} + \frac{h_t^2(2n^2-1)}{12 r_t^3}.
\end{aligned}
\tag{D.6}
$$

The antisymmetric loading coefficients are obtained from the following relations

$$
\begin{aligned}
a^a_{11} &= a^s_{11}, & a^a_{12} &= -a^s_{12}, & a^a_{13} &= a^s_{13},\\
a^a_{21} &= -a^s_{21}, & a^a_{22} &= a^s_{22}, & a^a_{23} &= -a^s_{23},\\
a^a_{31} &= a^s_{31}, & a^a_{32} &= -a^s_{32}, & a^a_{33} &= a^s_{33}.
\end{aligned}
\tag{D.7}
$$

D.2 Thick cylindrical shell equations

Thick cylindrical shell equations can be used to model the tunnel structure and an infinite soil with a cylindrical cavity in it. In the second case, the full-space is obtained considering the asymptotic case where the external radius of the shell tends to the infinite. The mathematical procedure followed to solve the problem is only outlined here. The details can be found the work presented by Gazis [115]. As in the thin shell case, two loading cases can be considered. The formulation is developed for the symmetric loading case but results for the antisymmetric case are also presented.

The solution of the problem is obtained decomposing the scalar and vector potentials in Fourier series and substituting the result into the transformed expression of Eqs. (C.3). The wave equations are then reduced to a system of Bessel differential equations of order n and $n+1$. Their solution, found using the following Gauge condition $\bar{\Psi}_{r,n} = -\bar{\Psi}_{\theta,n}$, can be written as

$$
\begin{aligned}
\bar{\Phi}_n &= A_n K_n(\nu_P r) + D_n I_n(\nu_P r),\\
\bar{\Psi}_{r,n} &= B_n K_{n+1}(\nu_S r) + E_n I_{n+1}(\nu_S r),\\
\bar{\Psi}_{\theta,n} &= -\bar{\Psi}_{r,n},\\
\bar{\Psi}_{x,n} &= C_n K_{n+1}(\nu_S r) + F_n I_{n+1}(\nu_S r),
\end{aligned}
\tag{D.8}
$$

where

$$
\nu_P^2 = k_x^2 - \frac{\omega^2}{c_P^2}, \qquad \nu_S^2 = k_x^2 - \frac{\omega^2}{c_S^2}.
\tag{D.9}
$$

The displacement and stress fields are obtained substituting Eqs. (D.8) into the transformed expressions of Eqs. (C.6) and (C.7). Their value at an arbitrary radius r can be written as

$$\bar{\mathbf{U}}_n = \mathbf{U}_{\mathrm{Th}}\Big|_r \mathbf{C}_n^{\mathrm{Th}}, \qquad \bar{\mathbf{T}}_n = \mathbf{T}_{\mathrm{Th}}\Big|_r \mathbf{C}_n^{\mathrm{Th}}, \tag{D.10}$$

where

$$\mathbf{C}_n^{\mathrm{Th}} = \begin{pmatrix} A_n & B_n & C_n & D_n & E_n & F_n \end{pmatrix}^T \tag{D.11}$$

has to be determined with the considered boundary conditions and where $\mathbf{U}_{\mathrm{Th}}\Big|_r$ and $\mathbf{T}_{\mathrm{Th}}\Big|_r$ are 3×6 matrices with the following coefficients

$$\begin{aligned}
u^s_{11} &= \frac{n}{r} I_n(\nu_P r) + \nu_P K_{n+1}(\nu_P r), & u^s_{12} &= \frac{n}{r} K_n(\nu_P r) - \nu_P K_{n+1}(\nu_P r),\\
u^s_{13} &= \mathrm{i}k_x I_{n+1}(\nu_S r), & u^s_{14} &= \mathrm{i}k_x K_{n+1}(\nu_S r),\\
u^s_{15} &= \frac{n}{r} I_n(\nu_S r), & u^s_{16} &= \frac{n}{r} K_n(\nu_S r),\\
u^s_{21} &= \frac{-n}{r} I_n(\nu_P r), & u^s_{22} &= \frac{-n}{r} K_n(\nu_P r),\\
u^s_{23} &= \mathrm{i}k_x I_{n+1}(\nu_S r), & u^s_{24} &= \mathrm{i}k_x K_{n+1}(\nu_S r),\\
u^s_{25} &= -\frac{n}{r} I_n(\nu_S r) - \nu_S I_{n+1}(\nu_S r), & u^s_{26} &= -\frac{n}{r} K_n(\nu_S r) + \nu_S K_{n+1}(\nu_S r),\\
u^s_{31} &= \mathrm{i}k_x I_n(\nu_P r), & u^s_{32} &= \mathrm{i}k_x K_n(\nu_P r),\\
u^s_{33} &= -\nu_S I_n(\nu_S r), & u^s_{34} &= \nu_S K_n(\nu_S r),\\
u^s_{35} &= 0, & u^s_{36} &= 0.
\end{aligned} \tag{D.12}$$

$$
\begin{aligned}
t^s_{12} &= \left(2\mu_s\frac{n^2-n}{r^2}-\lambda_s k_x^2+(\lambda_s+2\mu_s)\nu_P^2\right)K_n(\nu_P r)+2\mu_s\frac{\nu_P}{r}K_{n+1}(\nu_P r),\\
t^s_{14} &= -2\mu_s\mathrm{i}k_x\nu_S K_n(\nu_S r)-2\mu_s\mathrm{i}k_x\frac{n+1}{r}K_{n+1}(\nu_S r),\\
t^s_{16} &= 2\mu_s\frac{n^2-n}{r^2}K_n(\nu_S r)-2\mu_s\frac{n}{r}\nu_S K_{n+1}(\nu_S r),\\
t^s_{22} &= -2\mu_s\frac{n^2-n}{r^2}K_n(\nu_P r)+2\mu_s\frac{n}{r}\nu_P K_{n+1}(\nu_P r),\\
t^s_{24} &= -\mu_s\mathrm{i}k_x\nu_S K_n(\nu_S r)-2\mu_s\mathrm{i}k_x\frac{n+1}{r}K_{n+1}(\nu_S r),\\
t^s_{26} &= \left(-2\mu_s\frac{n^2-n}{r^2}-\mu_s\nu_S^2\right)K_n(\nu_S r)-2\mu_s\frac{\nu_S}{r}K_{n+1}(\nu_S r),\\
t^s_{32} &= 2\mu_s\mathrm{i}k_x\frac{n}{r}K_n(\nu_P r)-2\mu_s\mathrm{i}k_x\nu_P K_{n+1}(\nu_P r),\\
t^s_{34} &= \mu_s\frac{n}{r}\nu_S K_n(\nu_S r)-\mu_s(k_x^2+\nu_S^2)K_{n+1}(\nu_S r),\\
t^s_{36} &= \mu_s\mathrm{i}k_x\frac{n}{r}K_n(\nu_S r),\\
t^s_{11} &= \left(2\mu_s\frac{n^2-n}{r^2}-\lambda_s k_x^2+(\lambda_s+2\mu_s)\nu_P^2\right)I_n(\nu_P r)-2\mu_s\frac{\nu_P}{r}I_{n+1}(\nu_P r),\\
t^s_{13} &= 2\mu_s\mathrm{i}k_x\nu_S I_n(\nu_S r)-2\mu_s\mathrm{i}k_x\frac{n+1}{r}I_{n+1}(\nu_S r),\\
t^s_{15} &= 2\mu_s\frac{n^2-n}{r^2}I_n(\nu_S r)+2\mu_s\frac{n}{r}\nu_S I_{n+1}(\nu_S r),\\
t^s_{21} &= -2\mu_s\frac{n^2-n}{r^2}I_n(\nu_P r)-2\mu_s\frac{n}{r}\nu_P I_{n+1}(\nu_P r),\\
t^s_{23} &= \mu_s\mathrm{i}k_x\nu_S I_n(\nu_S r)-2\mu_s\mathrm{i}k_x\frac{n+1}{r}I_{n+1}(\nu_S r),\\
t^s_{25} &= \left(-2\mu_s\frac{n^2-n}{r^2}-\mu_s\nu_S^2\right)I_n(\nu_S r)+2\mu_s\frac{\nu_S}{r}I_{n+1}(\nu_S r),\\
t^s_{31} &= 2\mu_s\mathrm{i}k_x\frac{n}{r}I_n(\nu_P r)+2\mu_s\mathrm{i}k_x\nu_P I_{n+1}(\nu_P r),\\
t^s_{33} &= -\mu_s\frac{n}{r}\nu_S I_n(\nu_S r)-\mu_s(k_x^2+\nu_S^2)I_{n+1}(\nu_S r),\\
t^s_{35} &= \mu_s\mathrm{i}k_x\frac{n}{r}I_n(\nu_S r).
\end{aligned}
\tag{D.13}
$$

The antisymmetric loading coefficients are obtained from the following relations

$$\begin{array}{rclrclrcl}
u^a_{12} & = & u^s_{12}, & u^a_{14} & = & -u^s_{14}, & u^a_{16} & = & -u^s_{16},\\
u^a_{22} & = & -u^s_{22}, & u^a_{24} & = & u^s_{24}, & u^a_{26} & = & u^s_{26},\\
u^a_{32} & = & u^s_{32}, & u^a_{34} & = & -u^s_{34}, & u^a_{36} & = & -u^s_{36},\\
u^a_{11} & = & u^s_{11}, & u^a_{13} & = & -u^s_{13}, & u^a_{15} & = & -u^s_{15},\\
u^a_{21} & = & -u^s_{21}, & u^a_{23} & = & u^s_{23}, & u^a_{25} & = & u^s_{25},\\
u^a_{31} & = & u^s_{31}, & u^a_{33} & = & -u^s_{33}, & u^a_{35} & = & -u^s_{35}
\end{array} \tag{D.14}$$

and

$$\begin{array}{rclrclrcl}
t^a_{12} & = & t^s_{12}, & t^a_{14} & = & -t^s_{14}, & t^a_{16} & = & -t^s_{16},\\
t^a_{22} & = & -t^s_{22}, & t^a_{24} & = & t^s_{24}, & t^a_{26} & = & t^s_{26},\\
t^a_{32} & = & t^s_{32}, & t^a_{34} & = & -t^s_{34}, & t^a_{36} & = & -t^s_{36},\\
t^a_{11} & = & t^s_{11}, & t^a_{13} & = & -t^s_{13}, & t^a_{15} & = & -t^s_{15},\\
t^a_{21} & = & -t^s_{21}, & t^a_{23} & = & t^s_{23}, & t^a_{25} & = & t^s_{25},\\
t^a_{31} & = & t^s_{31}, & t^a_{33} & = & -t^s_{33}, & t^a_{35} & = & -t^s_{35}.
\end{array} \tag{D.15}$$

The soil is modelled as an infinite homogeneous isotropic elastic media with a circular cylindrical cavity in it. This is directly obtained considering that $r_{\text{ext}} \to \infty$ (see Fig. C.1). Because when $r \to \infty$ the displacement must satisfy the Sommerfeld radiation condition, a solution with physical meaning requires that $D_n = E_n = F_n = 0$, and the displacements and stress coefficients are given by

$$\bar{\mathbf{U}}_n = \mathbf{U}^{\text{fs}}\mathbf{C}_n, \quad \bar{\mathbf{T}}_n = \mathbf{T}^{\text{fs}}\mathbf{C}_n \tag{D.16}$$

where

$$\mathbf{C_n} = \begin{pmatrix} A_n & B_n & C_n \end{pmatrix}^T \tag{D.17}$$

and where the matrices $\mathbf{U}^{\text{fs}}$ and $\mathbf{T}^{\text{fs}}$ are 3×3 matrices constructed as follows

$$\mathbf{U}^{\text{fs}} = \begin{pmatrix} u_{12} & u_{14} & u_{16} \\ u_{22} & u_{24} & u_{26} \\ u_{32} & u_{34} & u_{36} \end{pmatrix}, \quad \mathbf{T}^{\text{fs}} = \begin{pmatrix} t_{12} & t_{14} & t_{16} \\ t_{22} & t_{24} & t_{26} \\ t_{32} & t_{34} & t_{36} \end{pmatrix}. \tag{D.18}$$

D.3 Tunnel/soil coupling

Once both subsystems have been transformed to the wavenumber-frequency domain and decomposed in Fourier series, the coupling between them is easily performed. This procedure is detailed here considering the tunnel as a thin shell and as a thick one.

D.3.1 Tunnel as a thin shell

The considered positive directions of the tunnel and soil displacement and stress fields have been presented in Figs. B.2 and C.1 respectively. Using the first ones for the soil displacements and stresses, Eq. (D.16) is rewritten as follows

$$\bar{\mathbf{U}}_n^{'} = \mathbf{U}_{\mathrm{th}}\mathbf{C}_n, \qquad \bar{\mathbf{T}}_n^{'} = \mathbf{T}_{\mathrm{th}}\mathbf{C}_n \tag{D.19}$$

where

$$\mathbf{U}_{\mathrm{th}} = \begin{pmatrix} u_{32} & u_{34} & u_{36} \\ u_{22} & u_{24} & u_{26} \\ -u_{12} & -u_{14} & -u_{16} \end{pmatrix}, \qquad \mathbf{T}_{\mathrm{th}} = \begin{pmatrix} -t_{32} & -t_{34} & -t_{36} \\ -t_{22} & -t_{24} & -t_{26} \\ t_{12} & t_{14} & t_{16} \end{pmatrix}. \tag{D.20}$$

Two coupling conditions are assumed at the interface between both systems. The first one, that the displacements of the soil and the tunnel are equal. The second one, that the stresses caused by each subsystem to the other are equal in magnitude and of opposite sign. Two loads are applied on the thin shell, the external load $\mathbf{p}$ which is applied on the interior surface of the tunnel, and the coupling load $\boldsymbol{\tau}_c$, applied on the exterior one. Considering both, Eq. (D.4) is then written as

$$\mathbf{A}_E\bar{\mathbf{U}}_n^t = (\bar{\mathbf{P}}_n - \bar{\mathbf{T}}_{c,n}). \tag{D.21}$$

where

$$\mathbf{A}_E = \frac{E_t h_t}{-r_t(1-\nu_t^2)}\mathbf{A}. \tag{D.22}$$

The equations of the soil at the interface are

$$\bar{\mathbf{U}}_n^{'}\Big|_{r_t} = \mathbf{U}_{\mathrm{th}}\Big|_{r_t}\mathbf{C}_n, \qquad \bar{\mathbf{T}}_n^{'}\Big|_{r_t} = \mathbf{T}_{\mathrm{th}}\Big|_{r_t}\mathbf{C}_n = \bar{\mathbf{T}}_{c,n}. \tag{D.23}$$

Due to the first coupling condition, $\bar{\mathbf{U}}_n^{'}\Big|_{r_t} = \bar{\mathbf{U}}_n^t$ and, substituting Eq. (D.23) into Eq. (D.21), the vector of unknown coefficients $\mathbf{C}_n$ can be written in terms of the coefficients of the transformed external load as

$$\mathbf{C}_n = \left(\mathbf{A}_E\mathbf{U}_{\mathrm{th}}\Big|_{r_t} + \mathbf{T}_{\mathrm{th}}\Big|_{r_t}\right)^{-1}\bar{\mathbf{P}}_n. \tag{D.24}$$

The displacement and stress coefficients at an arbitrary radius $r \geq r_t$ are given by

$$\bar{\mathbf{U}}_n^{'} = \mathbf{M}\bar{\mathbf{P}}_n \tag{D.25}$$

and

$$\bar{\mathbf{T}}_n' = \mathbf{K}\bar{\mathbf{P}}_n, \tag{D.26}$$

where

$$\mathbf{M} = \mathbf{U}_{\text{th}}\Big|_r \left(\mathbf{A}_E\mathbf{U}_{\text{th}}\Big|_{r_t} + \mathbf{T}_{\text{th}}\Big|_{r_t}\right)^{-1} \tag{D.27}$$

and

$$\mathbf{K} = \mathbf{T}_{\text{th}}\Big|_r \left(\mathbf{A}_E\mathbf{U}_{\text{th}}\Big|_{r_t} + \mathbf{T}_{\text{th}}\Big|_{r_t}\right)^{-1}. \tag{D.28}$$

Shell thickness correction

To take into account that one load is applied at the interior surface of the tunnel and the other at the exterior one, the following alternative expression of Eq. (D.21) has been proposed by Hussein [116]

$$\mathbf{A}_E\bar{\mathbf{U}}_n^t = \left(\frac{r_{\text{int}}}{r_t}\right)\bar{\mathbf{P}}_n - \left(\frac{r_{\text{ext}}}{r_t}\right)\bar{\mathbf{T}}_{c,n}, \tag{D.29}$$

being r_{int} and r_{ext} the interior and exterior radius of the tunnel respectively.

D.3.2 Tunnel as a thick shell

In this case, the tunnel and the soil equations are defined using the cylindrical system of coordinates defined in Fig. C.1. The displacement and stress Fourier series coefficients are then given by

$$\bar{\mathbf{U}}_n = \begin{cases} \mathbf{U}^{\text{fs}}\Big|_r \mathbf{C}_n, & r \geq \mathrm{r}_{\text{ext}} \\ \mathbf{U}_{\text{Th}}\Big|_r \mathbf{C}_n^{\text{Th}}, & \mathrm{r}_{\text{int}} \leq r \leq \mathrm{r}_{\text{ext}} \end{cases} \tag{D.30}$$

and

$$\bar{\mathbf{T}}_n = \begin{cases} \mathbf{T}^{\text{fs}}\Big|_r \mathbf{C}_n, & r \geq \mathrm{r}_{\text{ext}} \\ \mathbf{T}_{\text{Th}}\Big|_r \mathbf{C}_n^{\text{Th}}, & \mathrm{r}_{\text{int}} \leq r \leq \mathrm{r}_{\text{ext}} \end{cases} \tag{D.31}$$

where r_{int} and r_{ext} are the interior and exterior radius of the tunnel respectively. If an external load $\mathbf{p}$ is applied at the interior radius of the tunnel

$$\mathbf{T}_{\text{Th}}\Big|_{\mathrm{r}_{\text{int}}} \mathbf{C}_n^{\text{Th}} = -\mathbf{P}_n. \tag{D.32}$$

where the sign has been chosen considering the load directions opposite to the positive stress directions. At the exterior radius of the tunnel, the stress field is equal to the coupling stresses

$$\mathbf{T}_{\mathrm{Th}}\Big|_{\mathrm{r_{ext}}}\mathbf{C}_n^{\mathrm{Th}} = -\bar{\mathbf{T}}_n \tag{D.33}$$

An opposite coupling stress is applied at the soil cavity

$$\mathbf{T}^{\mathrm{fs}}\Big|_{\mathrm{r_{ext}}}\mathbf{C}_n = -\bar{\mathbf{T}}_n. \tag{D.34}$$

where has been used that the radius of the cavity is equal to the exterior radius of the tunnel.

Combining Eqs. (D.33) and (D.34),

$$\mathbf{T}_{\mathrm{Th}}\Big|_{\mathrm{r_{ext}}}\mathbf{C}_n^{\mathrm{Th}} = \mathbf{T}^{\mathrm{fs}}\Big|_{\mathrm{r_{ext}}}\mathbf{C}_n. \tag{D.35}$$

Assuming that the displacements at the surface of the soil cavity must be equal to the displacements at the outer radius of the tunnel

$$\mathbf{U}_{\mathrm{Th}}\Big|_{\mathrm{r_{ext}}}\mathbf{C}_n^{\mathrm{Th}} = \mathbf{U}^{\mathrm{fs}}\Big|_{\mathrm{r_{ext}}}\mathbf{C}_n. \tag{D.36}$$

Combining Eqs. (D.33), (D.35) and (D.36), the following system of equations is obtained

$$\begin{pmatrix} \mathbf{0}_{3\times 3} & \mathbf{T}_{\mathrm{Th}}\Big|_{\mathrm{r_{int}}} \\ \mathbf{T}^{\mathrm{fs}}\Big|_{\mathrm{r_{ext}}} & -\mathbf{T}_{\mathrm{Th}}\Big|_{\mathrm{r_{ext}}} \\ \mathbf{U}^{\mathrm{fs}}\Big|_{\mathrm{r_{ext}}} & -\mathbf{U}_{\mathrm{Th}}\Big|_{\mathrm{r_{ext}}} \end{pmatrix} \begin{pmatrix} \mathbf{C}_n \\ \mathbf{C}_n^{\mathrm{Th}} \end{pmatrix} = \begin{pmatrix} -\bar{\mathbf{P}}_n \\ \mathbf{0}_{6\times 1} \end{pmatrix}. \tag{D.37}$$

Once $\mathbf{C}_n$ and $\mathbf{C}_n^{\mathrm{Th}}$ are known, the displacements and stresses coefficients at any point of the soil or the tunnel are obtained using Eqs. (D.30) and (D.31).

D.4 Response to a distributed load

A harmonic load applied at $\theta = \theta_i$ and $r = r_t$ with an arbitrary distribution along the x-direction can be expressed as

$$\mathbf{p}(x,\theta,r,t) = \mathbf{P}\mathrm{e}^{\mathrm{i}\omega t} = \begin{pmatrix} P_x(x) \\ P_\theta(x) \\ P_r(x) \end{pmatrix} \frac{\delta(\theta-\theta_i)}{r_t}\mathrm{e}^{\mathrm{i}\omega t}. \tag{D.38}$$

This load is transformed to the wavenumber domain and decomposed in terms of ring modes. The transformed expression can be written as

$$\bar{\mathbf{P}} = \sum_{n=0}^{\infty} \left[\mathbf{S}^s \bar{\mathbf{P}}_n^s + \mathbf{S}^a \bar{\mathbf{P}}_n^a \right], \tag{D.39}$$

where

$$\bar{\mathbf{P}}_0^s = \frac{1}{2r_t\pi} \begin{pmatrix} \bar{P}_x \\ 0 \\ \bar{P}_r \end{pmatrix}, \qquad \bar{\mathbf{P}}_n^s = \frac{1}{r_t\pi} \begin{pmatrix} \bar{P}_x \cos(n\theta_i) \\ \bar{P}_\theta \sin(n\theta_i) \\ \bar{P}_r \cos(n\theta_i) \end{pmatrix}, \quad n > 0 \tag{D.40}$$

and

$$\bar{\mathbf{P}}_0^a = \frac{1}{2r_t\pi} \begin{pmatrix} 0 \\ \bar{P}_\theta \\ 0 \end{pmatrix}, \qquad \bar{\mathbf{P}}_n^a = \frac{1}{r_t\pi} \begin{pmatrix} \bar{P}_x \sin(n\theta_i) \\ \bar{P}_\theta \cos(n\theta_i) \\ \bar{P}_r \sin(n\theta_i) \end{pmatrix}, \quad n > 0. \tag{D.41}$$

The transformed displacement field is given by

$$\bar{\mathbf{U}} = \sum_{n=0}^{\infty} \left[\mathbf{S}^s \mathbf{M}^s \bar{\mathbf{P}}_n^s + \mathbf{S}^a \mathbf{M}^a \bar{\mathbf{P}}_n^a \right]. \tag{D.42}$$

where Eq. (D.25) and the sum of both formulations has been used.

Antitransforming Eq. (D.42), the displacement field can be finally written as

$$\mathbf{u} = \frac{1}{2\pi} \int_{-\infty}^{\infty} \sum_{n=0}^{\infty} \left[\mathbf{S}^s \mathbf{M}^s \bar{\mathbf{P}}_n^s + \mathbf{S}^a \mathbf{M}^a \bar{\mathbf{P}}_n^a \right] \mathrm{e}^{\mathrm{i}(\omega t - k_x x)} \mathrm{d}k_x. \tag{D.43}$$

An analogous expression for the stress field is obtained replacing the matrices **M** (Eq. (D.27)) by the matrices **K** (Eq. (D.28)) in the previous equation.

A radial harmonic point load applied at the bottom is given by

$$\mathbf{p} = \begin{pmatrix} 0 \\ 0 \\ 1 \end{pmatrix} \frac{\delta(\theta)\delta(x)}{r_t} \mathrm{e}^{\mathrm{i}\omega t}. \tag{D.44}$$

In this case, only the symmetric terms of Eqs. (D.40) and (D.41) remain. They are given by

$$\mathbf{P}_0^s = \frac{1}{2r_t\pi} \begin{pmatrix} 0 \\ 0 \\ 1 \end{pmatrix}, \qquad \mathbf{P}_n^s = \frac{1}{r_t\pi} \begin{pmatrix} 0 \\ 0 \\ 1 \end{pmatrix}, \quad n > 0 \tag{D.45}$$

and Eq (D.42) is reduced to

$$\bar{\mathbf{U}} = \frac{1}{2r_t\pi}\begin{pmatrix} m^s_{13,0} \\ 0 \\ m^s_{33,0} \end{pmatrix} + \frac{1}{r_t\pi}\sum_{n=1}^{\infty}\begin{pmatrix} m^s_{13,n}\cos(n\theta) \\ m^s_{23,n}\sin(n\theta) \\ m^s_{33,n}\cos(n\theta) \end{pmatrix}. \tag{D.46}$$

D.5 Plane-strain case

Plane-strain conditions are obeyed when the geometrical parameters, the mechanical parameters and the applied loads are invariant along the x-direction, and also, when these loads are perpendicular to this direction. The dynamic equations of the plane-strain case can be obtained from the transformed dynamic equations of the general case imposing that $k_x = 0$.

Using the thin shell system of coordinates (see Fig. B.2), the displacement and stress fields are reduced to

$$\mathbf{u} = \begin{pmatrix} u_\theta \\ u_r \end{pmatrix}, \quad \boldsymbol{\tau} = \begin{pmatrix} \tau_\theta \\ \tau_r \end{pmatrix} \tag{D.47}$$

As in the general case, the displacement and stress fields are written as

$$\begin{aligned} \mathbf{u} &= \mathbf{U}\mathrm{e}^{\mathrm{i}\omega t} = \sum_{n=0}^{\infty}\left[\mathbf{S}^s_{2\mathrm{D}}\mathbf{U}^s_n + \mathbf{S}^a_{2\mathrm{D}}\mathbf{U}^a_n\right]\mathrm{e}^{\mathrm{i}\omega t}, \\ \boldsymbol{\tau} &= \mathbf{T}\mathrm{e}^{\mathrm{i}\omega t} = \sum_{n=0}^{\infty}\left[\mathbf{S}^s_{2\mathrm{D}}\mathbf{T}^s_n + \mathbf{S}^a_{2\mathrm{D}}\mathbf{T}^a_n\right]\mathrm{e}^{\mathrm{i}\omega t}, \end{aligned} \tag{D.48}$$

where

$$\mathbf{S}^s_{2\mathrm{D}} = \begin{pmatrix} \sin n\theta & 0 \\ 0 & \cos n\theta \end{pmatrix}, \quad \mathbf{S}^a_{2\mathrm{D}} = \begin{pmatrix} \cos n\theta & 0 \\ 0 & \sin n\theta \end{pmatrix}. \tag{D.49}$$

The displacement and stress coefficients are again related to the external load coefficients by

$$\bar{\mathbf{U}}_n = \mathbf{M}_{2\mathrm{D}}\bar{\mathbf{P}}_n, \qquad \bar{\mathbf{T}}_n = \mathbf{K}_{2\mathrm{D}}\bar{\mathbf{P}}_n, \tag{D.50}$$

where the superscripts s and a have been again omitted and where

$$\begin{aligned} \mathbf{M}_{2\mathrm{D}} &= \mathbf{U}_{2\mathrm{D}}\Big|_r(\mathbf{A}_{\mathrm{E},2\mathrm{D}}\mathbf{U}_{2\mathrm{D}}\Big|_{r_t} + \mathbf{T}_{2\mathrm{D}}\Big|_{r_t})^{-1}, \\ \mathbf{K}_{2\mathrm{D}} &= \mathbf{T}_{2\mathrm{D}}\Big|_r(\mathbf{A}_{\mathrm{E},2\mathrm{D}}\mathbf{U}_{2\mathrm{D}}\Big|_{r_t} + \mathbf{T}_{2\mathrm{D}}\Big|_{r_t})^{-1}, \end{aligned} \tag{D.51}$$

where

$$\mathbf{A}_{\mathrm{E,2D}} = \frac{E_t h_t}{-r_t(1-\nu_t^2)} \begin{pmatrix} a_{11}^{\mathrm{2D}} & a_{12}^{\mathrm{2D}} \\ a_{21}^{\mathrm{2D}} & a_{22}^{\mathrm{2D}} \end{pmatrix} \tag{D.52}$$

and

$$\mathbf{U}_{\mathrm{2D}} = \begin{pmatrix} u_{21}^{\mathrm{2D}} & u_{22}^{\mathrm{2D}} \\ -u_{11}^{\mathrm{2D}} & -u_{12}^{\mathrm{2D}} \end{pmatrix}, \qquad \mathbf{T}_{\mathrm{2D}} = \begin{pmatrix} -t_{21}^{\mathrm{2D}} & -t_{22}^{\mathrm{2D}} \\ t_{11}^{\mathrm{2D}} & t_{12}^{\mathrm{2D}} \end{pmatrix}. \tag{D.53}$$

The coefficients are given by

$$\begin{aligned}
a_{11}^{\mathrm{2D},s} &= \frac{\rho r_t(1-\nu^2)\omega^2}{E} - \frac{n^2}{r_t}, \\
a_{12}^{\mathrm{2D},s} &= \frac{n}{r_t}, \\
a_{21}^{\mathrm{2D},s} &= a_{12}^{\mathrm{2D},s}, \\
a_{22}^{\mathrm{2D},s} &= \frac{\rho r_t(1-\nu^2)\omega^2}{E} - \frac{h_t^2}{12}\frac{n^4-2n^2+1}{r_t^3} - \frac{1}{r_t}, \\
u_{11}^{\mathrm{2D},s} &= \frac{n}{r}K_n(\nu_P r) - \nu_P K_{n+1}(\nu_P r), \\
u_{12}^{\mathrm{2D},s} &= \frac{n}{r}K_n(\nu_S r), \\
u_{21}^{\mathrm{2D},s} &= \frac{-n}{r}K_n(\nu_P r), \\
u_{22}^{\mathrm{2D},s} &= -\frac{n}{r}K_n(\nu_S r) + \nu_S K_{n+1}(\nu_S r), \\
t_{11}^{\mathrm{2D},s} &= \left(2\mu_s\frac{n^2-n}{r^2} + (\lambda_s+2\mu_s)\nu_P^2\right)K_n(\nu_P r) + 2\mu_s\frac{\nu_P}{r}K_{n+1}(\nu_P r), \\
t_{12}^{\mathrm{2D},s} &= 2\mu_s\frac{n^2-n}{r^2}K_n(\nu_S r) - 2\mu_s\frac{n}{r}\nu_S K_{n+1}(\nu_S r), \\
t_{21}^{\mathrm{2D},s} &= -2\mu_s\frac{n^2-n}{r^2}K_n(\nu_P r) + 2\mu_s\frac{n}{r}\nu_P K_{n+1}(\nu_P r), \\
t_{22}^{\mathrm{2D},s} &= \left(-2\mu_s\frac{n^2-n}{r^2} - \mu_s\nu_S^2\right)K_n(\nu_S r) - 2\mu_s\frac{\nu_S}{r}K_{n+1}(\nu_S r).
\end{aligned} \tag{D.54}$$

The antisymmetric loading formulation is given by

$$\begin{aligned}
a_{11}^{2\mathrm{D},a} &= a_{11}^{2\mathrm{D},s}, & a_{12}^{2\mathrm{D},a} &= -a_{12}^{2\mathrm{D},s},\\
a_{21}^{2\mathrm{D},a} &= -a_{21}^{2\mathrm{D},s}, & a_{22}^{2\mathrm{D},a} &= a_{22}^{2\mathrm{D},s},\\
u_{11}^{2\mathrm{D},a} &= u_{11}^{2\mathrm{D},s}, & u_{12}^{2\mathrm{D},a} &= -u_{12}^{2\mathrm{D},s},\\
u_{21}^{2\mathrm{D},a} &= -u_{21}^{2\mathrm{D},s}, & u_{22}^{2\mathrm{D},a} &= u_{22}^{2\mathrm{D},s},\\
t_{11}^{2\mathrm{D},a} &= t_{11}^{2\mathrm{D},s}, & t_{12}^{2\mathrm{D},a} &= -t_{12}^{2\mathrm{D},s},\\
t_{21}^{2\mathrm{D},a} &= -t_{21}^{2\mathrm{D},s}, & t_{22}^{2\mathrm{D},a} &= t_{22}^{2\mathrm{D},s}.
\end{aligned} \tag{D.55}$$

Bibliography

[1] J. Otero. *Contribución al estudio de las vibraciones producidas por el contacto rueda-carril y su transmisión al entorno.* PhD thesis, Universitat Politècnica de Catalunya, 2010.

[2] G. Bornitz. *Über die Ausbreitung der von Groszkolbenmaschinen erzeugten Bodenschwingungen in die Tiefe (About the propagation of ground vibrations generated by piston engines in depth).* J. Springer, 1931.

[3] D.D. Barkan. *Dynamics of bases and foundations.* McGraw-Hill, 1962.

[4] T.G. Gutowski and C.L. Dym. Propagation of ground vibration: A review. *Journal of Sound and Vibration*, 49(2):179–193, 1976.

[5] K. Chua, K. Lo, and T. Balendra. Building response due to subway train traffic. *Journal of Geotechnical Engineering*, 121(11):747–754, 1995.

[6] W. Gardien and H.G. Stuit. Modelling of soil vibrations from railway tunnels. *Journal of Sound and Vibration*, 267(3):605–619, 2003.

[7] C.J.C. Jones, D.J. Thompson, and M. Petyt. A model for ground vibration from railway tunnels. *Proceeding of the Institution of Civil Engineers-Transport*, 153 (2):121–129, 2002.

[8] L. Andersen and C.J.C. Jones. Coupled boundary and finite element analysis of vibration from railway tunnels–a comparison of two- and three-dimensional models. *Journal of Sound and Vibration*, 293(3-5):611–625, 2006.

[9] X. Sheng, C.J.C. Jones, and D.J. Thompson. Prediction of ground vibration from trains using the wavenumber finite and boundary element methods. *Journal of Sound and Vibration*, 293(3-5):575–586, 2006.

[10] S. François, M. Schevenels, P. Galvín, G. Lombaert, and G. Degrande. A 2.5D coupled FE-BE methodology for the dynamic interaction between longitudinally

invariant structures and a layered halfspace. *Computer Methods in Applied Mechanics and Engineering*, 199(23-24):1536–1548, April 2010.

[11] P. Galvín, S. François, M. Schevenels, E. Bongini, G. Degrande, and G. Lombaert. A 2.5D coupled FE-BE model for the prediction of railway induced vibrations. *Soil Dynamics and Earthquake Engineering*, 30:1500–1512, 2010.

[12] D. Clouteau, M. Arnst, T.M. Al-Hussaini, and G. Degrande. Freefield vibrations due to dynamic loading on a tunnel embedded in a stratified medium. *Journal of Sound and Vibration*, 283(1-2):173 – 199, 2005.

[13] X. Sheng, C.J.C. Jones, and M. Petyt. Ground vibration generated by a harmonic load acting on a railway track. *Journal of Sound and Vibration*, 225(1):3–28, 1999.

[14] X. Sheng, C.J.C. Jones, and M. Petyt. Ground vibration generated by load moving along railway track. *Journal of Sound and Vibration*, 228(1):129–156, 1999.

[15] V.V. Krylov. Low-frequency ground vibrations from underground trains. *Low Frequency Noise & Vibration*, 1995.

[16] A.V. Metrikine and A.C.W.M. Vrouwenvelder. Surface ground vibration due to a moving train in a tunnel: Two-dimensional model. *Journal of Sound and Vibration*, 234(1):43–66, 2000.

[17] J.A. Forrest and H.E.M. Hunt. A three-dimensional tunnel model for calculation of train-induced ground vibration. *Journal of Sound and Vibration*, 294(4):678–705, 2006.

[18] J.A. Forrest and H.E.M. Hunt. Ground vibration generated by trains in underground tunnels. *Journal of Sound and Vibration*, 294(4):706–736, 2006.

[19] W. Soedel. *Vibration of Shells and Plates*, volume 86 of *Mechanical Engineering*. Marcel Dekker, 1993.

[20] G. B. Warburton. The Vibration of Rectangular Plates. *Proceedings of the Institution of Mechanical Engineers*, 168(1):371–384, 1954.

[21] A.W. Leissa. Free Vibration Of Rectangular Plates. *Journal Of Sound And Vibration*, 31(3):257–293, 1973.

[22] A. Leissa. *Vibration of plates*. Acoustical Society of America, 1993.

[23] B. Liu and Y. Xing. Exact solutions for free in-plane vibrations of rectangular plates. *Acta Mechanica Solida Sinica*, 24(6):556–567, 2011.

[24] A. E. H. Love. The small free vibrations and deformation of a thin elastic shell. *Philosophical Transactions of the Royal Society of London. (A.)*, 179:491–546, 1888.

[25] L.H. Donnell. A discussion of thin shell theory. In *Proceedings of the Fifth International Congress of Applied Mechanics*, 1938.

[26] S. Timoshenko and S. Woinowsky-Krieger. *Theory of plates and shells.* McGraw-Hill Book Company, 1959.

[27] E. Reissner. A new derivation of the equations for the deformation of elastic shells. *American Journal of Mathematics*, 63(1):177–184, 1941.

[28] W. Flugge. *Stresses in shells.* Springer, 1967.

[29] J.L. Sanders Jr. *An improved first-approximation theory for thin shells.* 1959.

[30] A. Leissa. *Vibration of shells.* Acoustical Society of America, 1993.

[31] M.R. Peterson and D.E. Boyd. Free vibrations of circular-cylinders with longitudinal, interior partitions. *Journal of Sound and Vibration*, 60(1):45–62, 1978.

[32] R.S. Langley. A dynamic stiffness technique for the vibration analysis of stiffened shell structures. *Journal of Sound and Vibration*, 156(3):521–540, 1992.

[33] J. Missaoui, L. Cheng, and M.J. Richard. Free and forced vibration of a cylindrical shell with a floor partition. *Journal of Sound and Vibration*, 190(1):21–40, 1996.

[34] Y.S. Lee and M.H. Choi. Free vibrations of circular cylindrical shells with an interior plate using the receptance method. *Journal of Sound and Vibration*, 248 (3):477–497, 2001.

[35] Y.S. Lee, M.H. Choi, and J.H. Kim. Free vibrations of laminated composite cylindrical shells with an interior rectangular plate. *Journal of Sound and Vibration*, 265(4):795–817, 2003.

[36] Z.H. Wang, J.T. Xing, and W.G. Price. A study of power flow in a coupled plate-cylindrical shell system. *Journal of Sound and Vibration*, 271(3-5):863–882, 2004.

[37] Z. Zhao, M. Sheng, and Y. Yang. Vibration Transmission of a Cylindrical Shell with an Interior Rectangular Plate with the Receptance Method. *Advances in Acoustics and Vibration*, 2012:1–9, 2012.

[38] J.W.S. Rayleigh. On waves propagated along the plane surface of an elastic solid. *Proc. London Math. Soc.*, A 17:4–11, 1885.

[39] A.E.H. Love. *Some problems of geodynamics.* Cambridge University Press, 1911.

[40] R. Stoneley. Elastic waves at the surface of separation of two solids. *Proc. R. Soc. Lond. A*, 106:416–428, 1924.

[41] G.G. Stokes. On the dynamical theory of diffraction. *Transactions of the Cambridge Philosophical Society*, 9:1–62, 1851.

[42] H. Lamb. On the propagation of tremors over the surface of an elastic solid. *Philosophical Transactions of the Royal Society of London A*, 203:1–42, 1904.

[43] L. Cagniard. Réflexion et réfraction des ondes séismiques progressives. 1939.

[44] A.T. De Hoop. A modification of cagniards method for solving seismic pulse problems. *Applied Scientific Research, Section B*, 8(1):349–356, 1960.

[45] J.W.C. Sherwood. Elastic wave propagation in a semi-infinite solid medium. *Proceedings of the Physical Society*, 71(2):207–219, 1958.

[46] C.L. Pekeris. The seismic surface pulse. *Proceedings of the National Academy of Sciences*, 41:469–480, 1955.

[47] C.L. Pekeris. The seismic buried pulse. *Proceedings of the National Academy of Sciences*, 41:629–639, 1955.

[48] R. Arcos, J. Romeu, A. Balastegui, and T. Pàmies. Determination of the near field distance for point and line sources acting on the surface of an homogeneous and viscoelastic half-space. *Soil Dynamics and Earthquake Engineering*, 31(7): 1072–1074, 2011.

[49] G.F. Miller and H. Pursey. The field and radiation impedance of mechanical radiators on the free surface of semi-inifinite isotropic solid. *Proceedings of the royal society of London Series A-Mathematical and physical sciences*, 233(1155): 521–541, 1954.

[50] G. F. Miller and H. Pursey. On the partition of energy between elastic waves in a semi-infinite solid. *Proceedings of the Royal Society of London. Series A. Mathematical and Physical Sciences*, 233(1192):55–69, 1955.

[51] A. V. Razin. The radiation power of elastic waves excited in a solid half-space by a subsurface time-harmonic source. *Acoustical Physics*, 55:227–231, 2009.

[52] H.G. Georgiadis, D. Vamvatsikos, and I. Vardoulakis. Numerical implementation of the integral-transform solution to lamb's point-load problem. *Computational mechanics*, 24(2):90–99, 1999.

[53] R. Arcos, J. Romeu, A. Clot, and M. Genescà. Some analytical aspects of viscoelastic Lamb's problem for improving its numerical evaluation . *Wave Motion*, 50(2):226 – 232, 2013.

[54] R.J. Apsel and J.E. Luco. On the Green's functions for a layered half-space. Part II. *Bulletin of the Seismological Society of America*, 73(4):931–951, 1983.

[55] E. Kausel. *Fundamental solutions in elastodynamics. A compendium.* Cambridge University Press, 2006.

[56] W. T. Thomson. Transmission of elastic waves through a stratified solid medium. *Journal of Applied Physics*, 21:89, 1950.

[57] N.A. Haskell. The dispersion of surface waves in multilayered medium. *Bulletin of the Seismological Society of America*, 43:17–34, 1953.

[58] E. Kausel and J.M. Rosset. Stiffness matrices for layered soils. *Bulletin of the Seismological Society of America*, 71(6):1743–1761, 1981.

[59] W.T. Read. Stress analysis for compressible viscoelastic materials. *Journal of Applied Physics*, 21:671–674, 1950.

[60] C. Madshus and A.M. Kaynia. High-speed railway lines on soft ground: Dynamic behaviour at critical train speed. *Journal of Sound and Vibration*, 231(3):689–701, 2000.

[61] V.V. Krylov. Generation of ground vibrations by superfast trains. *Applied Acoustics*, 44(2):149–164, 1995.

[62] M.J.M.M. Steenbergen. Quantification of dynamic wheel-rail contact forces at short rail irregularities and application to measured rail welds. *Journal of Sound and Vibration*, 312(4-5):606–629, 2008.

[63] A.M. Remennikov and Kaewunruen. A review of loading conditions for railway track structures due to train and track vertical interaction. *Structural control and Health monitoring*, 15(2):207–234, 2008.

[64] K.L. Knothe and S.L. Grassie. Modelling of railway track and vehicles/track interaction at high frequencies. *Vehicle System Dynamics*, 22(3-4):209–262, 1993.

[65] D.J. Thompson. Wheel-rail noise generation, part 1: Introduction and interaction model. *Journal of Sound and Vibration*, 161(3):387–400, 1993.

[66] D.J. Thompson. Wheel-rail noise generation, part 2: Wheel vibration. *Journal of Sound and Vibration*, 161(3):401–419, 1993.

[67] D.J. Thompson. Wheel-rail noise generation, part 3: Rail vibration. *Journal of Sound and Vibration*, 161(3):421–446, 1993.

[68] K. Knothe and Y. Wu. Receptance behaviour of railway track and subgrade. *Archive of Applied mechanics*, 68(7-8):457–470, 1998.

[69] P. Van den Broek and G. De Roeck. The vertical receptance of track including soil-structure interaction. structural dynamics. In *Structural dynamics*, volume 1-2, pages 837–842, 1999. 4th European Conference on Structural Dynamics (EURODYN 99), Prague, Czech Republic.

[70] M. Heckl, G. Hauck, and R. Wettschureck. Structure-borne sound and vibration from rail traffic. *Journal of Sound and Vibration*, 193(1):175–184, 1996.

[71] G. Degrande and L. Schillemans. Free Field Vibrations During the Passage of a Thalys High-Speed Train At Variable Speed. *Journal of Sound and Vibration*, 247 (1):131–144, October 2001.

[72] S. Gupta, W.F. Liu, G. Degrande, G. Lombaert, and W.N. Liu. Prediction of vibrations induced by underground railway traffic in beijing. *Journal of Sound and Vibration*, 310(3):608–630, 2008.

[73] H. Kuppelwieser and A. Ziegler. A tool for predicting vibration and structure-borne noise immissions caused by railways. *Journal of Sound and Vibration*, 193 (1):261 – 267, 1996.

[74] *ISO 14837-1:2005 Mechanical vibration. Ground-borne noise and vibration arising from rail systems. Part 1: General Guidance.* International Organization for Standardization, 2005.

[75] *ISO 2631-1:1997 Mechanical vibration and shock. Evaluation of human exposure to whole-body vibration. Part 1: General requeriments.* International Organization for Standardization, 1997.

[76] *ISO 2631-2:2003 Mechanical vibration and shock. Evaluation of human exposure to whole-body vibration. Part 2: Vibration in buildings (1 Hz to 80 Hz).* International Organization for Standardization, 2003.

[77] R.A. Hood, R.J. Greer, M. Breslin, and P.R. Williams. The calculation and assessment of ground-borne noise and perceptible vibration from trains in tunnels. *Journal of Sound and Vibration*, 193(1):215 – 225, 1996.

[78] M.G. Floquet. Sur les équations différentielles linéaires à coefficients périodiques. *Annales Scientifiques de l'É.N.S*, 12:47–88, 1883.

[79] D. Cloteau, M.L. Elhabre, and D Aubry. Periodic BEM and FEM-BEM coupling - Application to seismic behaviour of very long structures. *Computational Mechanics*, 25(6):567–577, 2000.

[80] S. Gupta, M.F.M. Hussein, G. Degrande, H.E.M. Hunt, and D. Clouteau. A comparison of two numerical models for the prediction of vibrations from underground railway traffic. *Soil Dynamics and Earthquake Engineering*, 27(7):608–624, 2007.

[81] S. Gupta and G. Degrande. Modelling of continuous and discontinuous floating slab tracks in a tunnel using a periodic approach. *Journal of Sound and Vibration*, 329(1):1101–1125, 2010.

[82] D. Aubry, D. Cloteau, and G. Bonnet. Modelling of wave propagation due to fixed or mobile dynamic sources. In Chouw N. and G. Schimd, editors, *Workshop Wave '94, Wave propagation and Reduction of Vibrations*, 1994.

[83] X. Sheng, C.J.C. Jones, and D.J. Thompson. Responses of infinite periodic structures to moving or stationary harmonic loads. *Journal of Sound and Vibration*, 282(1-2):125–149, 2005.

[84] Y. B. Yang and H. H. Hung. A 2.5D finite/infinite element approach for modelling visco-elastic bodies subjected to moving loads. *International Journal for Numerical Methods in Engineering*, 51(11):1317–1336, 2001.

[85] Y.B. Yang and H.H. Hung. Soil vibrations caused by underground moving trains. *Journal of Geoenvironmental engineering*, 134(11):1633–1644, 2008.

[86] K. Müller, H. Grundmann, and S. Lenz. Nonlinear interaction between a moving vehicle and a plate elastically mounted on a tunnel. *Journal of Sound and Vibration*, 310(3):558–586, 2008.

[87] R.A. Clark, P.A. Dean, J.A. Elkins, and S.G. Newton. An investigation into the dynamic effects of railway vehicles running on corrugated rails. *Journal of Mechanical Engineering Science*, 24(1):65–76, 1982.

[88] M.F.M. Hussein and H.E.M. Hunt. A numerical model for calculating vibration from a railway tunnel embedded. *Journal of Sound and Vibration*, 305(3-5):401–431, 2007.

[89] M.F.M. Hussein and H.E.M. Hunt. A power flow method for evaluating vibration from underground railways. *Journal of Sound and Vibration*, 293:667 – 679, 2006.

[90] A.J.B. Tadeu and E. Kausel. Green's functions for two-and-a-half-dimensional elastodynamic problems. *Journal of Engineering Mechanics - ASCE*, 126(10): 1093–1097, 2000.

[91] A. Tadeu, J. António, and L. Godinho. Green's function for two-and-a-half dimensional elastodynamic problems in a half-space. *Computational Mechanics*, 27: 484–491, 2001.

[92] M.F.M. Hussein. An efficient model for calculating vibration from a railway tunnel buried in a half-space. Technical report, International Congress on Sound and Vibration, Vienna, 2006.

[93] S. Jones, M. Hussein, and H. Hunt. Use of PiP to investigate the effect of a free surface on ground vibration due to underground railways. *Acoustics Australia*, (1):2–6, 2010.

[94] M.F.M. Hussein, H.E.M. Hunt, L. Rikse, S. Gupta, D. Degrande, J.P. Talbot, S. Franois, and M. Schevenels. Using the PiP model for fast calculation of vibration from a railway tunnel in a multi-layered half-space. *Noise and vibration mitigation for rail transportation systems, Notes on numerical fluid mechanics and multidisciplinary design*, 99:136–142, 2008.

[95] G. Degrande, D. Clouteau, R. Othman, M. Arnst, H. Chebli, R. Klein, P. Chatterjee, and B. Janssens. A numerical model for ground-borne vibrations from underground railway traffic based on a periodic finite element-boundary element formulation. *Journal of Sound and Vibration*, 293(3-5, Sp. Iss. SI):645–666, 2006.

[96] S. Jones, K. Kuo, M. Hussein, and H. Hunt. Prediction uncertainties and inaccuracies resulting from common assumptions in modelling vibration from underground railways. *Proceedings of the Institution of Mechanical Engineers, Part F: Journal of Rail and Rapid Transit*, 226(5):501–512, March 2012.

[97] K.A. Kuo, H.E.M. Hunt, and M.F.M. Hussein. The effect of a twin tunnel on the propagation of ground-borne vibration from an underground railway. *Journal of Sound and Vibration*, 330(25):6203 – 6222, 2011.

[98] M.F.M. Hussein and H.E.M. Hunt. Modelling of floating-slab track with discontinuous slab - Part 1: Response to oscillating moving loads. *Journal of Low Frequency Noise Vibration and Active Control*, 25(1):23–39, 2006.

[99] M.F.M. Hussein and H.E.M. Hunt. Modelling of floating-slab tracks with continuous slabs under oscillating moving loads. *Journal of Sound and Vibration*, 297 (1-2):37–54, 2006.

[100] S. Jones and H. Hunt. Predicting surface vibration from underground railways through inhomogeneous soil. *Journal of Sound and Vibration*, 331(9):2055–2069, April 2012.

[101] S. Jones and H. Hunt. The effect of inclined soil layers on surface vibration from underground railways using a semi-analytical approach. *Journal of Physics: Conference Series*, 181:012050, August 2009.

[102] S. Jones and H. Hunt. Voids at the tunnel-soil interface for calculation of ground vibration from underground railways. *Journal of Sound and Vibration*, 330(2): 245–270, 2011.

[103] K.G. Graff. *Wave Motion in Elastic Solids.* Oxford University Press, 1975.

[104] P.J.P. Gonçalves, M.J. Brennan, and S.J. Elliott. Numerical evaluation of high-order modes of vibration in uniform Euler-Bernoulli beams. *Journal of Sound and Vibration*, 301(3-5):1035–1039, 2007.

[105] Y. Tang. Numerical evaluation of uniform beam modes. *Journal Of Engineering Mechanics-Asce*, 129(12):1475–1477, 2003.

[106] A power flow analysis of a double-deck circular tunnel embedded in a full-space. *Soil Dynamics and Earthquake Engineering*, 57(0):1–9,http://dx.doi.org/10.1016/j.soildyn.2013.10.008.

[107] J-T. Xing and W.G. Price. A power-flow analysis based on continuum dynamics. *Proceedings of the Royal Society of London. Series A: Mathematical, Physical and Engineering Sciences*, 455:401–436, 1999.

[108] H. Grundmann and E. Trommer. Transform methods what can they contribute to (computational) dynamics?". *Computers & Structures*, 79:2091–2102, 2001.

[109] L.N. Frazer and J.F. Gettrust. On a generalization of Filon's method and the computation of the oscillatory integrals of seismology. *Geophysical Journal of the Royal Astronomical Society*, 76(2):461–481, 1984.

[110] J.W. Cooley and J.W. Tukey. An algorithm for machine calculation of complex Fourier series. *Mathematics of Computation*, 19(90):297–301, 1965.

[111] J.D. Talman. Numerical fourier and bessel transforms in logarithmic variables. *Journal of Computational Physics*, 29:35–48, 1978.

[112] Q.H. Liu and Z.Q. Zhang. Nonuniform fast Hankel transform (NUFHT) algorithm. *Applied Optics*, 38(32):6705–6708, 1999.

[113] Q.H. Liu and Z.Q. Zhang. Nonuniform fast Hankel transform (NUFHT) algorithm: errata. *Applied Optics*, 39(11):1842, 2000.

[114] J. D. Achenbach. *Wave propagation in elastic solids*, volume 16 of *Applied Mathematics and Mechanics*. Elsevier, eight edition, 1999.

[115] D.C. Gazis. Three-dimensional investigation of the propagation of waves in hollow circular cylinders. i. analytical foundation. *The Journal of the Acoustical Society of America*, 31(5):568–573, 1959.

[116] M.F.M. Hussein. *Vibration from underground railways.* PhD thesis, University of Cambridge, 2004.